Capillarity and dynamic wetting

by

Andreas Carlson

March 2012 Technical Reports Royal Institute of Technology Department of Mechanics SE-100 44 Stockholm, Sweden Akademisk avhandling som med tillstånd av Kungliga Tekniska Högskolan i Stockholm framlägges till offentlig granskning för avläggande av teknologie doktorsexamen fredagen den 23 mars 2012 kl 10.00 i Salongen, Biblioteket, Kungliga Tekniska Högskolan, Osquars Backe 25, Stockholm. © Andreas Carlson 2012 E-PRINT, Stockholm 2012

Capillarity and dynamic wetting

Andreas Carlson 2012 Linné FLOW Centre, KTH Mechanics SE-100 44 Stockholm, Sweden

Abstract

In this thesis capillary dominated two-phase flow is studied by means of numerical simulations and experiments. The theoretical basis for the simulations consists of a phase field model, which is derived from the system's thermodynamics, and coupled with the Navier Stokes equations. Two types of interfacial flow are investigated, droplet dynamics in a bifurcating channel and spontaneous capillary driven spreading of drops.

Microfluidic and biomedical applications often rely on a precise control of droplets as they traverse through complicated networks of bifurcating channels. Three–dimensional simulations of droplet dynamics in a bifurcating channel are performed for a set of parameters, to describe their influence on the resulting droplet dynamics. Two distinct flow regimes are identified as the droplet interacts with the tip of the channel junction, namely, droplet splitting and non-splitting. A flow map based on droplet size and Capillary number is proposed to predict whether the droplet splits or not in such a geometry.

A commonly occurring flow is the dynamic wetting of a dry solid substrate. Both experiments and numerical simulations of the spreading of a drop are presented here. A direct comparison of the two identifies a new parameter in the phase field model that is required to accurately predict the experimental spreading behavior. This parameter $\mu_f \ [Pa \cdot s]$, is interpreted as a friction factor at the moving contact line. Comparison of simulations and experiments for different liquids and surface wetting properties enabled a measurement of the contact line friction factor for a wide parameter space. Values for the contact line friction factor from phase field theory are reported here for the first time.

To identify the physical mechanism that governs the droplet spreading, the different contributions to the flow are measured from the simulations. An important part of the dissipation may arise from a friction related to the motion of the contact line itself, and this is found to be dominating both inertia and viscous friction adjacent to the contact line. A scaling law based on the contact line friction factor collapses the experimental data, whereas a conventional inertial or viscous scaling fails to rationalize the experimental observation, supporting the numerical finding.

Descriptors: Phase field theory, finite element simulations, experiments, two-phase flow, dynamic wetting, contact line physics, capillarity.

Preface

- Research results presented in this thesis were obtained by the author during the period between December 2007 and March 2012. The work was performed at the Department of Mechanics at The Royal Institute of Technology.
- **Paper 1.** Carlson, A., Do-Quang, M., & Amberg, G. 2010 Droplet dynamics in a bifurcating channel. *International Journal of Multiphase Flow* **36** (5), 397–405.
- Paper 2. Carlson, A., Do-Quang, M., & Amberg, G. 2009 Modeling of dynamic wetting far from equilibrium. *Physics of Fluids* 21 (12), 121701-1-4.
- **Paper 3.** Carlson, A., Do-Quang, M., & Amberg, G. 2011 Dissipation in rapid dynamic wetting. *Journal of Fluid Mechanics* **682**, 213–240.
- **Paper 4.** Carlson, A., Bellani, G., & Amberg, G. 2012 Contact line dissipation in short-time dynamic wetting. *EPL* **97**, 44004-1–6.
- **Paper 5.** Carlson, A., Bellani, G., & Amberg, G. 2012 Universality in dynamic wetting dominated by contact line friction. Submitted to Rapid Communications in Physical Review E.

Below is a list of related work that has been performed by the author in the same period of time, but not included in this thesis.

International archival journals

LAURILA, T., CARLSON, A., DO-QUANG, M, ALA-NISSILÄ, T. & AMBERG, G. 2012 Thermo-hydrodynamics of boiling in a van der Waals fluid. *Accepted in Physical Review E*.

DO-QUANG, M., CARLSON, A., & AMBERG, G. 2011 The Impact of Ink-Jet Droplets on a Paper-Like Structure. Fluid Dynamics & Materials Processing 7 4, 389–402.

LIN, Y., SKJETNE, P. & CARLSON, A. 2011 A phase field model for multiphase electro–hydrodynamic flow. Submitted to International Journal of Multiphase Flow

Refereed conference proceedings

LIN, Y., SKJETNE, P. & CARLSON, A. 2010 A phase field method for multiphase electro-hydrodynamic flow. *International Conference on Multiphase Flow*, Tampa, USA.

Do-Quang, M., Carlson, A. & Amberg, G. 2010 The impact of ink-jet droplets on a paper-like structure. *International Conference on Multiphase Flow*, Tampa, USA.

Carlson, A., Do-Quang, M. & Amberg, G. 2010 Characterization of droplet dynamics in a bifurcating channel. *International Conference on Multiphase Flow*, Tampa, USA.

Carlson, A., Do-Quang, M. & Amberg, G. 2009 Spontaneously spreading liquid droplets in a dynamic wetting process. *EUROTHERM-84*, Namur, Belgium.

Carlson, A., Lakehal, D. & Kudinov, P. 2009 A multiscale approach for thin-film slug flow. 7th World Conference on Experimental Heat Transfer, Fluid Mechanics and Thermodynamics, Krakow, Polen.

Do-Quang, M., Carlson, A. & Amberg, G. 2008 Capillary force dominated impact of particle to free liquid surface *Proc.* of the 1st European Conference on Microfluidics - Microfluidics, Bologna, Italy.

Carlson, A., Do-Quang, M. & Amberg, G. 2008 Droplet dynamics in a microfluidic bifurcation. *Proc. of the 1st European Conference on Microfluidics* - *Microfluidics*, Bologna, Italy.

Carlson, A., Kudinov, P. & Narayanan, C. 2008 Prediction of two-phase flow in small tubes: A systematic comparison of state-of-the-art CMFD codes. 5th European Thermal-Sciences Conference, Eindhoven, Netherlands.

Division of work between authors

- **Paper 1.** The code was implemented by Andreas Carlson (AC) and Minh Do-Quang (MDQ). AC performed the simulations and analyzed the data. The paper was written by AC, with feedback from MDQ and Gustav Amberg (GA).
- **Paper 2.** The code was implemented by AC and MDQ. AC performed the simulations and analyzed the data. The paper was written by AC, with feedback from MDQ and GA.
- **Paper 3.** AC performed the simulations and analyzed the data. The paper was written by AC, with feedback from MDQ and GA.
- **Paper 4.** AC and Gabriele Bellani (GB) designed the initial experiments. The image processing tool was developed by GB. AC performed the experiments, the simulations and analyzed the data. AC wrote the article, with feedback from GB and GA.
- **Paper 5.** AC and GB designed the initial experiments. The image processing tool was developed by GB. AC performed the experiments, the simulations and analyzed the data. AC wrote the article, with feedback from GB and GA.





Abstract	iv
Preface	v
Part I - Summary	
Chapter 1. Introduction	1
Chapter 2. Capillarity	5
2.1. Surface tension	5
2.2. Young-Laplace Law	5
2.3. Dynamic capillary flows and non–dimensional numbers	6
2.4. Wetting – Young's Law	7
Chapter 3. Dynamic wetting	9
3.1. Hydrodynamic theory	9
3.2. Microscopic model	11
3.3. Experiments of dynamic wetting	12
3.4. Simulations of dynamic wetting	16
3.4.1. Macroscopic free energy models	16
3.4.2. Molecular dynamics simulations	18
Chapter 4. Phase field theory	21
4.1. Free energy	21
4.2. Evolution of fluxes	22
4.2.1. Decrease of free energy	22
4.2.2. Cahn–Hilliard and Navier Stokes equations	23
4.3. Phase field interface and surface tension	24
4.4. Wetting boundary condition	25
4.4.1. Local equilibrium	25
4.4.2. Non–equilibrium	26
Chapter 5. Numerical methodology	29
5.1. Finite Element toolbox – femLego	29
5.2. Numerical schemes	29
5.2.1. Cahn–Hilliard equation	29
5.2.2. Navier Stokes equations	31
Chapter 6. Summary of results	33
Chapter 7. Concluding remarks	41
Acknowledgements	44

Part II - Papers						
Paper 1.	Droplet dynamics in a bifurcating channel	63				
Paper 2.	Modeling of dynamic wetting far from equilibrium	87				
Paper 3.	Dissipation in rapid dynamic wetting	99				
Paper 4.	${\bf Contact\ line\ dissipation\ in\ short-time\ dynamic\ wetting}$	135				
Paper 5.	Universality in dynamic wetting dominated by contact line friction	151				

Bibliography

Part I Summary

CHAPTER 1

Introduction

In our daily life we often observe beautiful two-phase flow phenomena; formation of drops as the kitchen tap is turned on, how coffee spill stains the table linen, rain drops sliding on the windshield or cooking oil convecting towards the frying pans colder part. These common occurrences are all governed by the physics at the interface between the liquid and gas phase or at the contact line where the liquid-gas-solid phases meet. In other words they are dictated by the surface tension and the liquid-solid wettability.

Nature has used surface tension to develop several ingenious designs for insect propulsion, water collection and capillary adhesion. For instance water striders are able to walk on water despite the fact that they are heavier than water, see fig. 1.1b. Their hairy legs prevent water from wetting them and instead of penetrating the surface and sink, the feet deform the interface generating a surface tension force that supports the insect. Various beetles use surface tension in a different way. Instead of running on water, they have developed a method based on surface tension to adhere onto solid substrates. This allows them to easily walk up a vertical wall, or to withstand a pulling force much greater than their own weight, fig. 1.1a (Eisner & Aneshansley) (2000)). The beetle's secret is that it secretes an oil that wets their brush-like feet. When in need of protection from a predator they sit down, in order for thousands of their pre-wetted micron sized setae to contact the solid. This generates an adhesion force that sucks the beetle to the solid. Yet another example from Nature is the Namib desert beetle (Parker & Lawrence (2011)). Early in the morning the Namib beetles can be observed on the crest of the desert dunes, gazing against the wind, with their shells pushed up and heads lowered. This funny posture is important for the beetle to harvest water. In the hot and harsh climate, collection of water is a challenging task. The beetle has developed a design for water collection, which relies on the surface energy of its outer shell. The bumpy shell contains parts with a low energy that water wets well (hydrophilic) and parts with a wax layer (high energy) that water wets poorly (hydrophobic). The humid morning breeze condensates on their shell, where water drops nucleates on the hydrophilic tip of the bumps. As the drop grows it becomes affected by gravity and rolls down on the hydrophobic parts of its shell, guiding the drop towards its mouth.

Capillary flow is not only a toy problem observed in the kitchen and in many of Natures phenomena. It can even be a matter of life or death as we take our very first breath. In the late 1920's Dr. von Neergaard started to investigate the correlation between surface tension and the respiratory distress syndrome of newly born children (Comroe (1977)). He suggested that surface tension at the moist lung tissue could influence their breathing. To test his hypothesis he measured the force required to fill the lung with two liquids; air and an aqueous solution. A larger resistance to breath was found when breathing air, indicating a surface energy effect. von Neergaards hypothesis about capillarity was only much later recognized, making surface tension an assassin of newly born for about another 30 years after his discovery. Today it is established that respiratory distress syndrome is caused by the lack of production of a pulmonary surfactant, effectively reducing the lung surface tension easing the first breath of life (Wrobel (2004)).

Since the advent of microfluidic technologies in the early 1990's there has been an increasing demand for miniaturized components in different applications. Examples of such micro-scale components are lab-on-chip technologies for the analysis of medical samples or microsystem technologies which use the two-phase flow as switches, compartments for mixing and chemical reactions. Readers with special interest in microfluidics are referred to specific literature on the subject, for more details see for example Stone et al. (2004). One important aspect in these small scale applications, in terms of governing physics, is the fact that they are small. This makes surface forces, opposite to volume forces (inertia, gravity ect.), an important parameter for both design and performance. In many cases the two-phase flow consist of drops or bubbles, that are used as a deterministic tool for a desired process. Embolotheraphy (Eshpuniyani et al. (2005), Bull (2005)) utilizes drops as a medical treatment strategy for certain types of cancer, if all other treatments have failed. Drops are injected into the blood stream, with the purpose to block a junction where the capillary separates into two smaller vessels. This is done in an attempt to occlude the blood flow into the tumor, starving it from oxygen and inhibiting its growth. After ended treatment, these droplets are selectively vaporized using high-intensity ultrasound.

A common aspect in microfluidics and in our interaction with liquids are contact lines. The contact line is the point in which three different immiscible materials meet. The discussion here will only regard systems in which two of the materials are fluids, both gas and liquid, and the third material is a smooth solid. Contact lines are important in processes such as coating see fig. 1.1b (Snoeijer et al. (2006)), re-wetting dry eyes, deposition of micro-droplets in bio-medical applications or microfluidic systems. Even if contact lines are an important part in many applications, the physics that governs its motion still hold great challenges to physicists. In particular it is hard to derive a theoretical prediction for the contact line motion without using ad-hoc physical assumptions. Another difficulty in both experiments and numerical simulations is to capture all relevant length scales inherent in the phenomenon. Often a drop of millimeter size is observed as it spread due to the capillary force. The

relevant length scale for the physical processes at the contact line is in the order of the interface width, being roughly a nanometer. One question that arises naturally is, how does the small scale physics at the contact line influence the larger scale dynamics, and vise versa.

In this thesis capillary and dynamic wetting phenomena are studied by means of numerical simulations and experiments. The thesis consist of two parts; Part I and Part II. Part I is a broad description of relevant theoretical, experimental and modeling aspects. First the general principles of capillarity and wetting are discussed, giving a brief description of theoretical models in static and dynamic situations. A more in–depth discussion about dynamic wetting is presented, including theoretical, experimental and modeling approaches reported in the literature. In section 4 the theoretical formulation used to describe capillary dominated flows and dynamic wetting are described. Section 5 gives a description of the numerical modeling approach. Some final remarks are made in the last section of Part I. Part II is a collection of written articles.

4 1. INTRODUCTION

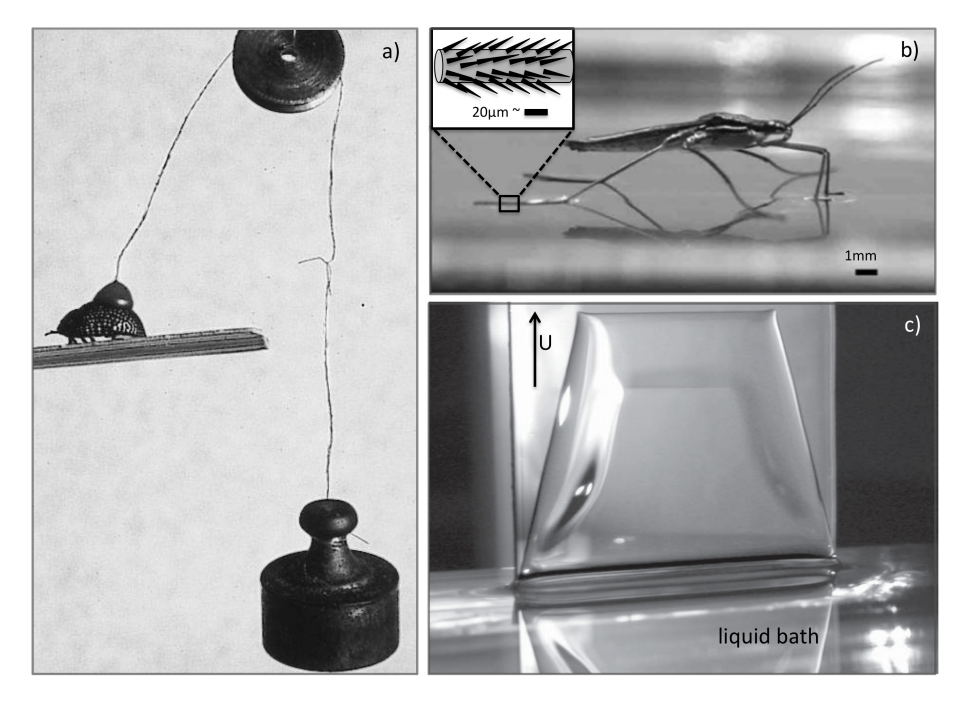


Figure 1.1: a)¹ A beetle (weight 13.5 ± 0.4 mg) adhered to the solid, withstanding a 2g pulling force (Eisner & Aneshansley (2000)). b)² The water strider Gerris walking on the free surface in experiment by Hu & Bush (2010), the inset to the upper left illustrates the water striders hairy leg. c)³ Forced wetting experiment by Snoeijer *et al.* (2006), withdrawing a Si–wafer from a bath of silicone oil. The capillary oil ridge is formed at the contact line, as the plate is withdrawn.

¹Eisner, T. & Aneshansley, D. J. (2000) Defense by foot adhesion in a beetle (Hemisphaerota cyanea). *Proceedings of the National Academy of Sciences U.S.A* **97**, 6568–6573, fig. 2. © 2000 National Academy of Sciences U.S.A.

 $^{^2{\}rm Hu},$ D. & Bush, J. W. (2010) The hydrodynamics of water-walking arthropods. Journal of Fluid Mechanics, $\bf 644,$ 5–33, fig.1. © 2010 Cambridge University Press.

³Snoeijer, J. H., Delon, G., Fermigier, M. & Andreotti, B. (2006) Avoided Critical Behavior in Dynamically Forced Wetting. *Physical Review Letters*, **96**, 17450-4–8, fig. 1. © 2006 American Physical Society.

CHAPTER 2

Capillarity

2.1. Surface tension

Surface tension may be interpreted on two different scales, the micro-scale and the macro-scale. On the macroscopic scale surface tension can be described within the thermodynamic framework as the interface energy per surface area (de Gennes et al. (2004), Berg (2010)). The origin of surface tension is however coming from the details of the intermolecular reorganization at the interface between the two phases. Let us consider a silicone oil drop in air, as seen in fig. 2.1. The oil molecules have an attraction toward each other, which is stronger than the attraction to the surrounding gas. As a consequence, the molecules on the liquid side of the interface feel a stronger attraction towards the oil rather than the air molecules. The "lost" pair-interaction generates an excessive free energy, which takes the form as surface tension on the macroscopic scale. More information about the molecular origin of surface tension can be found in the book by Israelachivili (2011).

2.2. Young-Laplace Law

Normal to the interface a force arises from the surface tension. This force is directly related to the local curvature of the interface. Young and Laplace were the first to relate the overpressure in drops and bubbles to the surface tension and interface curvature (de Gennes *et al.* (2004)). The Young-Laplace law for a spherical drop or bubble is,

$$P_i - P_o = \Delta P = \frac{2\sigma}{R}. (2.1)$$

Here P_i [Pa] is the pressure inside the drop, P_o is the pressure outside, σ [N/m] is the surface tension coefficient and R the drop radius. The factor two is due to the fact that the drop has two radii of curvature.

One way to derive the relationship for the Laplace pressure is to consider the work required to move the interface a small length δR in the radial direction. For mechanical equilibrium the work done by the pressure on the increased volume will be equal to the increase in surface energy (Berg (2010)). The same result is also obtained, by considering the pressure and surface energy as a grand potential. Minimizing the potential gives then the Young–Laplace Law, which illustrates that drops and bubbles find their surface energy minimizing shape (de Gennes et al. (2004)).

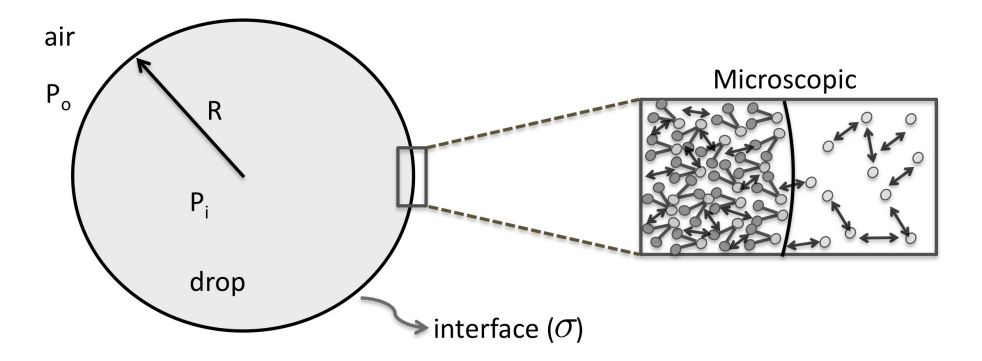


Figure 2.1: The sketch to the left shows a liquid drop in air. Overpressure in the drop (P_i) is generated by the surface tension σ . The sketch to the right illustrates the molecular organization at the interface, where the molecules at the interface feels an attraction to the liquid side generating the surface tension force. The arrows are intended to illustrate the intermolecular interaction.

2.3. Dynamic capillary flows and non-dimensional numbers

Hydrostatics of bubbles and drops is not particularly relevant in most applications. Two-phase flow is in general a time dependent phenomenon. Drops often traverse through channels of complicated geometrical shapes, where they deform and might split into several smaller drops. The deformation of the interface generates a local change in curvature, giving rise to a dynamic capillary force that tries to prevent the drops from deforming when an outer force acts on it. Determining the resulting drop dynamics is important in microfluidic systems, where it is often required to have precise control of whether drops would deform or split into two separate drops when approaching a channel junction (Carlson et al. (2010), Pozrikidis (2012), Manga (1996)) or an obstacle (Protiére et al. (2010), Link et al. (2004), Menetrier-Deremble and Tabeling (2006)).

One non-dimensional parameter that controls the splitting or non-splitting is the Capillary number (Ca). The Ca number expresses the ratio between the viscous and surface tension force in the flow,

$$Ca = \frac{\mu U}{\sigma} \tag{2.2}$$

 μ $[Pa \cdot s]$ is viscosity and U [m/s] is the characteristic velocity like the bubble or drop speed.

In small scale flow volume forces are usually less important. A measure of the influence of gravity is the capillary length $l_c = \sqrt{\frac{\sigma}{\rho g}}$. The capillary length

can be derived from the Bond number,

$$Bo = \frac{\rho g L^2}{\sigma}. (2.3)$$

In the Bo number ρ $[kg/m^3]$ is density, g $[m/s^2]$ gravity and L [m] the characteristic length, typically the drop radius. By assuming Bo = 1 having all the material properties, the capillary length is defined. If the drop size is $L < l_c$ or Bo < 1 gravity can be excluded from the analysis, as it gives a small contribution to the flow compared to surface tension. Another observation is that a drop with a radius less than the capillary length has a spherical shape, withstanding any deformation by gravity. The capillary length of water can be computed by introducing its material properties at room temperature $(\rho = 10^3 kg/m^3, \sigma = 73mN/m, g = 9.81m/s^2)$, giving $l_c \approx 2mm$. This tells us that water drops with a radius less than 2mm will be nearly unaffected by gravitational effects and have spherical shapes.

Another important non-dimensional number is the Reynolds number (Re), expressing the ratio between the inertial and the viscous force in the flow,

$$Re = \frac{\rho UL}{\mu}. (2.4)$$

A typical length scale L appears in the Re. In small scale flows, such as microfluidics, this has the implication that Re < 1 in contrast to most common observation of liquid flow such as smoke from a cigaret or a chimney, or when mixing milk in a cup of coffee. To illustrate relevant Re numbers in a microfluidic application we can introduce parameters that are commonly encountered in such systems. Let us assume a water drop with a radius similar to the size of the microfluidic channel $L = 10 \mu m$ that propagates with a speed U = 10 mm/s, having a density $\rho = 1000 kg/m^3$ and viscosity $\mu = 1 mPas$. Computing the Re number based on these parameters gives $Re = 10^{-4}$, illustrating the dominance of the viscous force.

2.4. Wetting – Young's Law

Compared to the description of a free surface, a slightly more complicated physical situation arises when it comes in contact with a third phase. Here the discussion will be limited to situations where the two fluid phases are gas-liquid or liquid-liquid, and when their interface is in contact with a dry smooth solid substrate. The point in which the interface intercepts the solid substrate is defined as the contact line or the three–phase point, see fig. 2.2.

Not only the drop interface has a surface energy (σ) , also the solid substrate has an energy that is different if it is dry (σ_{sg}) or wet (σ_{sl}) . In an equilibrium situation the drop will have a shape that minimizes the interfacial energy. By following a similar line of thought as when obtaining the Young–Laplace law in Sec. 2.2, the equilibrium angle between the tangent along the drop interface and the solid substrate can be found. This was first done by Young, giving his

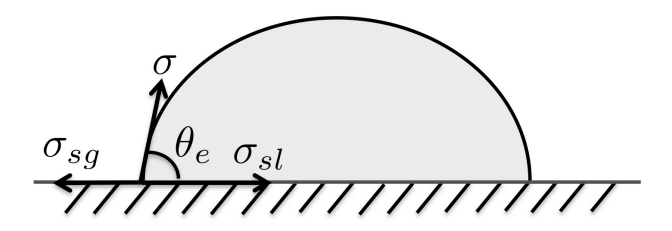


Figure 2.2: Sketch of a drop that partially wets the solid substrate and is in its equilibrium state. θ_e is the equilibrium angle, given by the surface tension and energy for the wet and dry solid substrate.

celebrated formula relating the solid surface energies to the surface tension and the equilibrium angle θ_e (de Gennes *et al.* (2004)),

$$\cos(\theta_e) = \frac{\sigma_{sg} - \sigma_{sl}}{\sigma}. (2.5)$$

 θ_e is defined as the angle in the liquid phase formed between a tangent along the interface, intersecting the contact line and the solid surface, see fig. 2.2.

The equilibrium angle is used as a measure of how well a liquid wets the solid substrate. One can roughly say that if the equilibrium angle $\theta_e^{\circ} < 90$ the solid is often referred to as being hydrophilic, or "water loving". If $\theta_e > 90^{\circ}$ the solid is considered to be hydrophobic or "water hating".

Two other states in the hydrophilic and hydrophobic regime should also be noted, which is complete wetting ($\theta_e \approx 0^\circ$) and non-wetting ($\theta_e > 120^\circ$) or superhydrophobic. In complete(perfect) wetting $\theta_e \approx 0^\circ$ and the liquid spreads completely onto the solid. The liquid will continue to spread until it forms a continuous film with a nano–scopic height. Superhydrophobic substrates have proven hard to produce in laboratories, using relatively smooth solid surfaces. Such a non wetting state can however be observed in Nature, where the Lotus leaf is one example of a plant with superhydrophobic leafs. If we look at the Lotus leaf through a microscope we can see that its surface is not smooth, but it has rather an hierarchical surface structure of humps. To obtain highly non–wetting substrates $\theta_e > 120^\circ$, either surface structures (Quéré (2008)) or a lubricating immiscible liquid film can be introduced (Wong et al. (2011), Lafuma & Quéré (2011)).

Another measure for the surface wettability is the spreading coefficient. The spreading coefficient S is given by the difference in surface energy between a dry and wet substrate $S = \sigma_{sg} - (\sigma_{sl} + \sigma) = \sigma(\cos(\theta_e) - 1)$. If $S \ge 0$ the liquid spreads completely onto the solid and if S < 0 the solid is only partially wetted by the liquid.

CHAPTER 3

Dynamic wetting

In contrast to the well established Young's law for an equilibrium wetting state, a theoretical description of dynamic wetting has proven to hold great scientific challenges, and the derivation of constituent laws usually rely on ad–hoc physical assumptions. What makes the description of contact line motion difficult, is the inherent multiscale nature of the phenomenon. To predict the macroscale spreading, physics at the length scale of the contact line must somehow be accounted for in the analysis. The preceding sections discuss general concepts regarding theoretical, experimental and modeling aspects of dynamic wetting. Several reviews are written on the topic, which gives a more detailed account of the theoretical approaches as well as the vast literature on the subject, see e.g. de Gennes (1985), Leger & Joanny (1992) and Bonn et al. (2009).

3.1. Hydrodynamic theory

Navier Stokes equations are the cornerstone for the description of flow physics, given here for an incompressible flow

$$\nabla \cdot \mathbf{u} = 0 \tag{3.1}$$

$$\rho \left(\frac{\partial \mathbf{u}}{\partial t} + \mathbf{u} \cdot \nabla \mathbf{u} \right) = -\nabla P + \mu \nabla^2 \mathbf{u} + \mathbf{F}$$
 (3.2)

where eq. 3.1 contains the mass conservation equation and eq. 3.2 contains the momentum equations. Here \mathbf{u} is the velocity, P the pressure and \mathbf{F} is a force per volume, like gravity. If the size of the system studied is much greater than the mean free path of the molecular motion, a no–slip condition holds as a boundary condition for the velocities at a solid wall. No–slip implies that there is no relative speed between the wall and the fluid elements adjacent to it.

Since the Navier Stokes equations present a well defined mathematical model for the flow physics, Huh & Scriven (1971) tried to develop a model for the contact line motion based on these equations. They assumed Stokes flow ($Re \ll 0$) and that the contact line has a wedge shaped form at the wall. Both the viscous stress and viscous dissipation was derived based on these assumptions, where they showed that both of these become infinite at the contact line, if a no–slip condition was applied at the wall. This finding made Huh &

Scriven (1971) coin the now famous expression that "... not even Heracles could sink a solid...". They also stressed that this could indeed be an indication that the physical model was not entirely valid. The no–slip condition is within the Navier Stokes framework incompatible with the contact line motion.

Even if the hydrodynamic framework had been shown to predict an unbounded stress at the contact line, Voinov (1976) used these equations to describe the contact line motion for a spreading drop. By making the assumption that the $Ca \ll 1$ and that the curvature of the outer solution is small, he derived a relationship for the apparent contact angle ($\theta^3 \approx Ca$) and the spreading radius ($r \approx t^{\frac{1}{10}}$) in time based on asymptotic theory. Tanner (1979) considered a similar situation, for a drop spreading on a solid with S=0, so that a precursor film has formed ahead of the drop. Later Cox (1986) presented a more generalized derivation, arriving at a similar result with some correction terms. The dependency of the apparent contact angle and spreading rate on the Ca number is often referred to as the Voinov–Tanner–Cox law. Similar expressions have also been derived by Hocking (1977) and Eggers (2005), where the latter uses the thin film lubrication approximation.

If we use the problem formulation presented by Tanner, the relationship for a complete spreading case can be easily derived based on a force balance between the capillary and the viscous force. By disregarding any influence of the precursor film and assuming the interface has the shape of a wedge ($\theta \ll 1$) at the contact line, the viscous dissipation can be equated and balanced by capillarity, giving $\theta^3 \approx \mu U/\sigma \log(L/L_m)$ (de Gennes et al. (2004)). θ is the apparent contact angle and U the spreading speed. L and L_m are length scales for the macroscopic and microscopic length, respectively. The microscopic length L_m is assumed to be the height of the precursor film ahead of the drop, and hence

$$\theta = \left(\log(\frac{L}{L_m})\frac{\mu U}{\sigma}\right)^{\frac{1}{3}} = \left(\log(\frac{L}{L_m}) \cdot Ca\right)^{\frac{1}{3}}.$$
 (3.3)

For a spherical cap shaped drop with $\theta \ll 1$, the apparent contact angle relates to the spreading radius, r, in the manner $\theta \approx 4V/r^3$. Introducing this relationship into eq. 3.3, where U = dr/dt and integrating gives the Tanner's law for viscous spreading, disregarding all numerical coefficients

$$r \approx L \left(\frac{\sigma L}{\mu} t\right)^{\frac{1}{10}}$$
 (3.4)

Using the problem formulation by Tanner gives a relationship that is independent of the spreading parameter S. If however, performing a detailed derivation as by Voinov and Cox, a correction for the apparent contact angle appears where also a microscopic angle θ_m must be defined. A common assumption is to choose this angle equal to be the equilibrium angle, thus giving a correction for partial wetting to the above expression.

 L_m represents a contribution from the microscopic scale, and to regularize the solution this microscopic length scale needs to be defined. It can be viewed

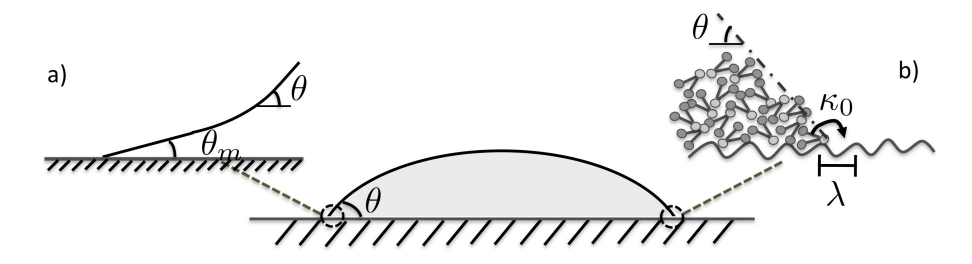


Figure 3.1: The main figure at the center shows a sketch of a drop that spreads on a solid substrate. a) Shows an interpretation of the microscopic (θ_m) and the apparent dynamic (θ) contact angle in the hydrodynamic theory. b) Sketch of the molecular motion at the contact line in the molecular kinetic theory. k_0 is the characteristic jump frequency, λ the length between adsorption sites and θ the dynamic contact angle.

as the slip length at the contact line, although this length is often found to be much larger than what can be physically argued (Winkels *et al.* (2011)). Another suggestion to avoid the singularity at the contact line for partial wetting has been to involve a disjoining pressure, arising from the molecular interactions at the contact line, to predict the cut-off for the hydrodynamic theory (de Gennes (1985), Eggers (2005)).

One of the shortcomings of the hydrodynamic theory today is that it cannot fully capture spreading when either Ca or Re number is of order one. In the former case it is found hard to formulate the appropriate boundary condition to couple the outer large scale to the small scale solution at the contact line.

3.2. Microscopic model

Since hydrodynamic theory does not give an adequate description of the dissipative processes at the contact line, different microscopic models have been suggested as complementary explanations. Blake & Haynes (1969) proposed a theory based on the motion of molecules in the contact line region. This model is often referred to as the chemical model, since it is based on a similar idea as the chemical reaction rate (Glasstone et al. (1941)), or as the Molecular Kinetic theory (MKT). Contrary to hydrodynamic theory, the large scale dynamics are completely dictated by the molecular processes at the contact line.

In the MKT the molecules hop forward (K^+) and backward (K^-) (Blake (2006)), which are predicted in a statistical sense as

$$K^{+} = k_0 \exp(\frac{w}{2nk_bT}), \ K^{-} = k_0 \exp(\frac{-w}{2nk_bT}).$$
 (3.5)

n [1/ m^2] is the number of molecular adsorption sites per unit area, k_0 [s^{-1}] is the characteristic hopping frequency, k_b [J/K] the Boltzmann constant and T [K] the temperature. w [N/m] is the activation energy for hopping between

sites, modeled as the difference between the equilibrium and dynamic contact angle $w = \sigma(\cos(\theta_e) - \cos(\theta))$. The contact line velocity is readily derived by taking the difference between the forward and backward hopping times the jump length, λ [m], between activation sites

$$V_{MK} = \lambda (K^+ - K^-) = 2k_0 \lambda \sinh\left(\frac{\sigma(\cos(\theta_e) - \cos(\theta))}{2nk_b T}\right). \tag{3.6}$$

At equilibrium the backward and forward hopping are equal, as are the dynamic and equilibrium contact angle, predicting no contact line motion.

When the difference between the equilibrium angle and the dynamic angle is small, the contact line velocity given in eq. 3.6 reduces to $V_{MK} \approx \frac{\lambda k_0 \sigma}{n k_b T} (\cos(\theta_e) - \cos(\theta))$ (de Ruijter et al. (1999)). The linear form of the contact line velocity is most often used to match experimental results, where k_0 , n and λ are fitting parameters that needs to be adjusted based on experimental observations. To obtain a match with experiments λ is often found to be much larger than the molecular size (de Gennes et al. (2004)).

The inverse of the pre–factor $(\frac{\lambda k_0}{nk_bT})^{-1}$ multiplying the linear form of the contact line velocity has also been interpreted in terms of a macroscopic friction factor, which would generate a local dissipation. Since both the hydrodynamic and the MKT has been found to explain different experimental data, Petrov & Petrov (1992) suggested a model in an attempt to merge the two different approaches to better explain wetting experiments.

One way to include both a local effect at the contact line and the contribution from the bulk viscosity to describe wetting phenomena, is to use a thermodynamic formulation as suggested by Brochard-Wyart & de Gennes (1992) and de Ruijter et al. (1999). What drives the contact line motion is the off equilibrium contact angle that generates a work $W = r\sigma(\cos(\theta_e) - \cos(\theta))$. In equilibrium, the free energy (Φ) is constant and the rate of change of work $(\dot{W} = U\sigma(\cos(\theta_e) - \cos(\theta)))$ should equal the dissipation $(T\dot{S})$, $\dot{\Phi} = \dot{W} - T\dot{S}$ (Brochard-Wyart & de Gennes (1992)),

$$U\sigma(\cos(\theta_e) - \cos(\theta)) = \frac{3\mu \log(L/L_m)}{\theta} U^2 + \Lambda \cdot U^2.$$
 (3.7)

 $\Lambda [Pa \cdot s]$ is a friction parameter at the contact line generating a local dissipation. Two regimes can be interpreted from this model, depending on the relative magnitude of the two terms on the right hand side.

3.3. Experiments of dynamic wetting

Experimental approaches to study dynamic wetting can be separated into two groups, forced wetting or capillary driven spreading (see fig. 3.2). In forced wetting experiments the contact line dynamics is studied by exerting an external force onto the fluid, which moves the contact line. An example of a forced wetting setup is the extraction, or pushing, of a plate out of or into a liquid bath. Another example is contact line motion in a capillary, which is driven by an external piston acting onto the fluid phase. A coating process is a particular

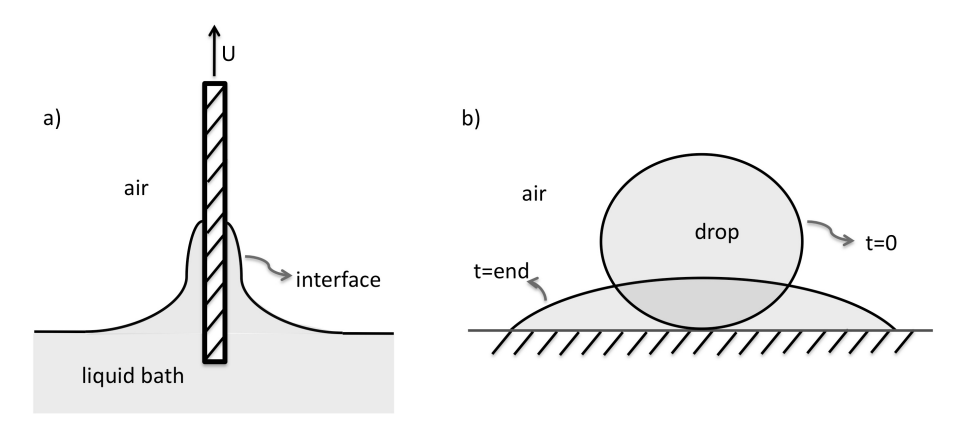


Figure 3.2: a) Sketch of a forced wetting experiment, as a plate is withdrawn with a speed U from a liquid bath. b) Example of capillary driven spreading, as a liquid drop comes in contact with a dry solid substrate. The drop has initially an spherical shape, and at equilibrium the drop has the shape of a spherical cap.

relevant application for forced wetting. Capillary driven spreading is different from forced wetting by that there is no external force exerted onto the fluid and the flow is driven by the capillary force local to the contact line. Two examples of typical experimental setups to study forced and capillary driven spreading are shown in fig. 3.2. Both hydrodynamic and microscopic theories have been used to rationalize experimental observations from both forced and capillary driven wetting.

Hoffman (1975) investigated the contact line motion in a capillary, where the flow was driven by an external piston. He observed a seemingly universal behavior of the relationship between the dynamic contact angle θ and the Ca number. His observation $\theta \approx Ca^{\frac{1}{3}}$ was later verified analytically by Voinov (1976), Tanner (1979) and Cox (1986). Tanner (1979) investigated the spreading of silicone drops, and saw the same dependency of the θ and the Ca number. Ström $et\ al.$ (1989) studied the liquid meniscus when a chemically treated metal blade was lowered or raised in a bath of silicone oil. Different oil viscosity and plate speed were examined and the results were in good agreement with the hydrodynamic theory, see fig. 3.3.

Marsh et al. (1993) studied forced wetting in a similar setup as Ström et al. (1989), using a cylinder instead of a plate. By fitting the microscopic length in the logarithm in the hydrodynamic theory, they achieved good agreement with the experiments. Since the Ca number was varied nearly three orders of magnitude, this also allowed a parametric study of the microscopic length used in the fitting procedure. This length was found to depend on the speed of the cylinder and it was hard to find any significant trend in the value of L_m in

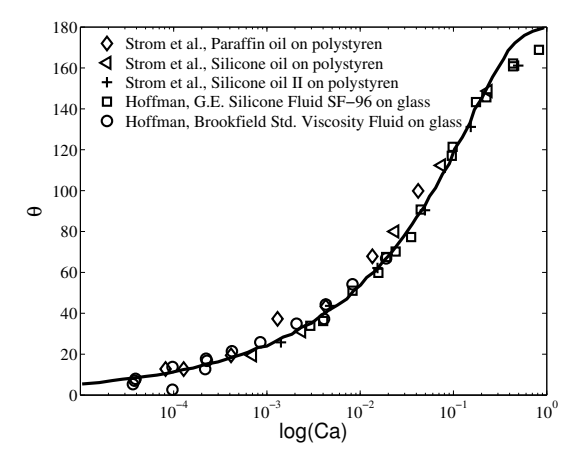
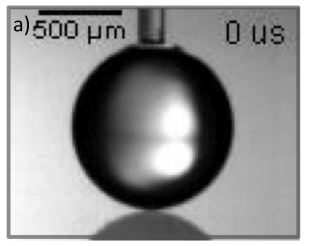


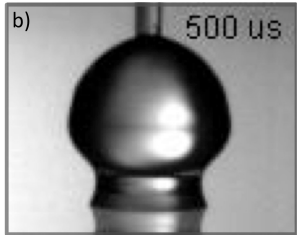
Figure 3.3: Comparison of the hydrodynamic theory and the perfectly wetting experiments by Ström *et al.* (1989) and Hoffman (1975). The fully drawn line represents the analytical function by Cox (1986) for $(L/L_m = 10^4)$ and $\theta_e = 0^\circ$. The figure is adopted from Bonn *et al.* (2009).

eq. 3.3 for the different experiments. However, the logarithmic nature of the correction caused the dynamic angle to change only slightly even if L_m varied over different orders of magnitude.

In the above described experiments the $Ca \ll 1$. For Ca > 0.1 Chen et al. (1995) demonstrated that the theory fails to predict the experimental results. Extension of the asymptotic solution (Cox (1986)) to also account for larger Ca numbers, is still an open theoretical question (Eggers (2004)).

Hayes & Ralston (1993) studied forced wetting, and found the hydrodynamic theory to only give a good prediction over a limited velocity range. The MKT was however found to give a better description of the experimental observation, where the hopping length λ , frequency k_0 and n sites per area needs to be adjusted. Based on the MKT de Ruijter et al. (1999), de Ruijter et al. (2000) derived a relationship for the spreading radius in time $r \approx t^{\frac{1}{7}}$ and the dynamic contact angle $\theta \approx t^{-\frac{3}{7}}$, which was also found experimentally (de Ruijter et al. (1999) and De Coninck et al. (2001)). Seveno et al. (2009) looked at capillary driven spreading of different liquids and evaluated the data with the hydrodynamic, combined model (Petrov & Petrov (1992)) and the MKT. Of the four liquids used in the experiments the most viscous liquid was found to follow the hydrodynamic theory, and the least viscous liquid the MKT. For intermediate viscosities the results were best described by a combined model. Recently, spreading experiments by Duvivier et al. (2011) were performed for liquids with a large span in viscosities, in an attempt to connect the local friction factor at the contact line in the MKT to the liquid bulk viscosity. The





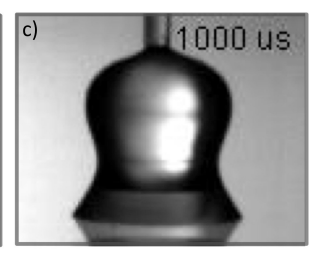


Figure 3.4: ⁴Three snapshots in time as a water drop spreads onto a dry glass plate, which has an equilibrium angle of $\theta_e \approx 3^{\circ}$.

frictional coefficient was determined by adjusting the friction factor appearing in the linearized form of the MKT, so that the theory matched the experiments.

Prevost et al. (1999) studied the contact line motion of superfluid helium at cryogenic temperatures (< 2K) in an attempt to remove any effect from viscosity. They measured the force acting at the contact line, where they found the contact line to move through thermally activated jumps related to the roughness of the Cesium substrate.

Rapid spontaneous spreading has been investigated by several authors (Biance et al. (2004), Drelich & Chibowska (2005), Bird et al. (2008), Courbin et al. (2009), Carlson et al. (2012a) and Carlson et al. (2012b)). Fig. 3.4 shows three snapshots in time from a high-speed imaging of a water drop spreading on a dry glass plate ($\theta_e \approx 3^{\circ}$). The drop spreads rapidly across the solid and has within a millisecond traveled a distance similar to its initial radius. Such rapid short-time spreading was proposed by Biance et al. (2004) and Drelich & Chibowska (2005) to be governed by inertial forces. By making a simplified force balance Biance et al. (2004) predicted the droplet radius to evolve as the square root of time. Water drops that spread on almost perfectly wetted solids, verified their power-law prediction. Bird et al. (2008) performed similar experiments but investigated the influence of the wettability of the solid substrate. For water spreading on a surface with low contact angle $\theta_e = 3^{\circ}$ they found the same exponent in the power-law as Biance et al. (2004). However, the exponent was found to be a function of the equilibrium contact angle. Carlson et al. (2011) presented another interpretation of the spreading physics. By integrating experiments and phase field simulations, another dissipative contribution was identified at the contact line, interpreted through a contact line friction factor (Carlson et al. (2012a)). By evaluating the dissipative contributions and the rate of change of kinetic energy, contact line dissipation was identified to dominate short time spreading even for rather large viscosities $(85mPa \cdot s)$. The contact line friction factor was measured from the numerics by adjusting the parameter so that the numerics and experiments matched for different

⁴Experiments performed at Princeton University from an ongoing work in collaboration with Pilnam Kim, Gustav Amberg and Howard A. Stone.

viscosities. A scaling law (Carlson *et al.* (2012b)) based on the contact line friction factor collapsed the experimental data for a wide range of viscosities $(1 - 85mPa \cdot s)$, different drop size and solid surface wettabilities. The same exponent was observed in the power–law when using a scaling based on the contact line friction parameter, even for different wettabilities. Bliznyuk *et al.* (2010) also observed the spreading radius to evolve as square root in time, for spontaneous spreading of viscous glycerin drops.

3.4. Simulations of dynamic wetting

Several modeling approaches exist for two–phase flow, which represents the interface in different ways. Most popular are the Volume–of–Fluid (Hirt & Nichols (1989)) and Level Set (Osher & Sethian (1988)) method, which define the interface through a numerically prescribed volume fraction or as a level set function, respectively. These methods do not require re–meshing of the interface, as the numerical color/level set function is solved by an advection equation on a fixed mesh. The interface can also be modeled by a moving mesh as in the boundary element method (Pozrikidis (2001)), whereas the front tracking method (Unverdi & Tryggvason (1992)) is a hybrid of the boundary fitted and volumetric interface methods. All of these methods have in common that the boundary condition for the moving contact line is not well defined, and relies on ad–hoc slip models.

A different way to obtain macroscopic models for two-phase flow is by postulating the free energy of the system. Through the free energy a phase field method can be derived for the interfacial dynamics in the bulk and on solid boundaries through a wetting boundary condition. On the nano-scale, molecular dynamic simulations represents a modeling framework that also naturally incorporates moving contact lines between different molecular species. The discussion below will be limited to literature about phase field simulations on the macro-scale and molecular dynamics simulation on the nano-scale.

3.4.1. Macroscopic free energy models

The phase field method, also labeled as the diffuse interface method, predicts from the system thermodynamics a solution for an interface that has a finite thickness (ϵ) , an idea that dates back to van der Waals (1893). Different phase field models can be derived based on the postulated free energy of the system or through its equation of state. Anderson *et al.* (1998) gives a review of the most popular phase field methods.

The phase field theory presents an alternative way, than described above, to obtain models of wetting phenomena. By defining the surface energies, a boundary condition can be derived for the contact line motion that allows it to move, even when a no–slip condition is applied for the velocity. The contact line moves by interfacial diffusion, avoiding the Huh–Scriven paradox and overcomes the difficulty that arises at the contact line in classical hydrodynamic theory. Another important point is that this makes the flow at the contact

line somewhat different than the prediction from classical hydrodynamic theory. Flow lines passes through the interface as the interfacial diffusion moves the contact line (Seppecher (1996)). Pomeau (2011) interpreted this as if there would be a local phase change at the contact line.

Phase field models exhibit many attractive features such as; mass conservation, obeys the laws of thermodynamics, contact line motion, ect., but there are still questions about its validity when modeling macroscopic contact line motion. With todays state-of-the-art computational resources a millimeter drop can be simulated with an interface that is about thousand times smaller than its radius. This interface thickness will then be in the order of micrometers. For liquids that are far from their critical point, like for instance water at room temperature, the interface has a thickness of about a nanometer. A direct consequence is that the thickness of the interface needed in macroscopic simulations has to be taken much larger than what can be physically motivated. Another question that still lingers is its sharp-interface limit ($\epsilon \to 0$), and whether such a solution exists at the contact line (Wang & Wang (2007)). Although these aspects presents a rather grim outlook for using a phase field method to simulate contact line motion, meaningful results have been predicted on the macro scale in accordance with hydrodynamic theory by Villanueva & Amberg (2006a), Yue et al. (2010) and Yue & Feng (2011) as well as in experimental observations by Carlson et al. (2012a), Do-Quang & Amberg (2009b) and Villanueva et al. (2006b).

By prescribing the equation—of—state for a van der Waals fluid, Teshigawara & Onuki (2010) derived a theoretical framework to study wetting close to the critical point. Spreading dynamics of a drop in a thermal gradient was studied on a perfectly wetting substrate. Liquid condensed at the precursor film, without the need to define the evaporation rate. The volatility of these liquids would not allow comparison with Voinov—Tanner—Cox law or experimental observation of non-volatile liquids.

Phase field simulations of macroscopic wetting for an incompressible flow are usually based on the Cahn–Hilliard equations. For relatively slow wetting phenomena, in a similar regime as the Voinov–Tanner–Cox theory, phase field theory has proven both analytically (Jacqmin (2000)) as well as numerically (Villanueva & Amberg (2006a), Yue et al. (2010), Yue & Feng (2011), Briant & Yeomans (2004)) to capture such wetting physics. Jacqmin (2000) proposed an effective slip length based on the mobility constant multiplying the chemical potential and the dynamic viscosity. Briant & Yeomans (2004) found the contact line diffusion to vary over a length scale different than the interface width, and by scaling arguments showed that this length is related to the mobility constant multiplying the chemical potential. Yue et al. (2010) modified the scaling argument for the diffusion length and instead interpreted this length in terms of the microscopic length appearing in hydrodynamic theory (L_m) . It should be noted that all of these results are obtained by making the physical

assumption that the interface is close to an equilibrium state as it wets the solid.

In order to capture spontaneous rapid spreading of water drops, Carlson et al. (2009) and Carlson et al. (2011) showed that the assumption of local equilibrium fails to capture the experimental observations. By retaining any perturbation in the concentration at the solid, a boundary condition for wetting far from equilibrium can be derived. A new parameter appears in the boundary condition, which controls the relaxation towards equilibrium. Carlson et al. (2012a) interpreted this coefficient as a local friction adjacent to the contact line and measured from the numerics its dissipative contribution in the flow. A different explanation was proposed, contrasting the previously suggested inertial wetting by Biance et al. (2004) and Bird et al. (2008), where the dissipation from the contact line is claimed to dominate the flow. By matching experiments and simulations for liquids of different viscosity, wetting substrates with different wetting properties, allowed a numerical measure of the contact line friction parameter. The experimental data collapsed using a scaling law based on the contact line friction parameter. In simulations Yue et al. (2010) and Yue & Feng (2011) interpreted the local friction parameter as a relaxation parameter at the contact line. Instead of suggesting this to be a physical mechanism it was assumed to be a numerical, compensating for having an artificially large diffusion length.

3.4.2. Molecular dynamics simulations

Contact line motion has also been studied on the microscopic scale through molecular dynamics simulations. Even with the increasing computational power, these systems are still limited to tens of nano meters. By prescribing the intermolecular interaction between the different types of molecules their motion are determined by Newtons first law. One convenient outcome of this is that the contact line can be modeled without the need for ad–hoc assumptions, as it is directly a solution based on the intermolecular potentials. Fig. 3.5 shows three snapshots in time from a molecular dynamics simulation of an Argon droplet spreading on a smooth Titanium substrate.

Some of the earliest studies on contact line dynamics were performed by Koplik et al. (1988) and Thomson & Robbins (1989). Koplik et al. (1988) studied the slip at the contact line in a Poiseuille flow and Thomson & Robbins (1989) in a Couette flow, both using a Lennard–Jones potential for the intermolecular interaction. Thomson & Robbins (1989) found the apparent angle in the simulations to follow the Tanner–Voinov–Cox theory. He & Hadjiconstantinou (2003) used molecular dynamics to study the spreading of a drop on a solid substrate that it wets perfectly. To avoid evaporation of the liquid a spring model was used between the molecules, which mimics the chain interaction between monomers. In the two dimensional (or quasi-three dimensional) simulation the radius was found to evolve as $r \approx t^{1/7}$, in accordance with classical theory. Many others have also used moleuclar dynamics to probe

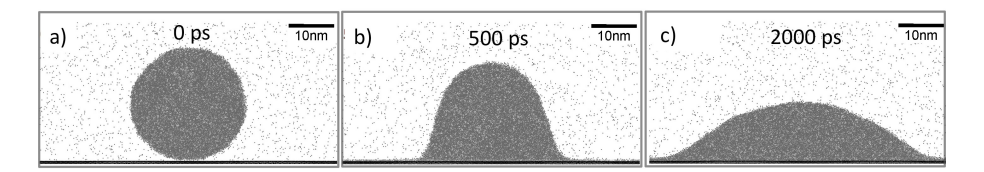


Figure 3.5: ⁵ Snapshots from a molecular dynamics simulations of an Argon drop with a radius of 12nm as it spreads in time on a Titanium substrate with $\theta_e \approx 0^\circ$ at 80K. The intermolecular interactions are determined through a Lennard–Jones potential.

different wetting phenomena using models for different liquids and geometries (De Coninck *et al.* (1995), Matsumoto *et al.* (1995)). Findings from molecular dynamics simulations can be summarized as; the contact line is regularized by a small slip region inside the interface and any deviation from the equilibrium angle causes a large response that drives the contact line motion (Ren & E (2007)).

Based on molecular dynamics observations Qian et al. (2003) developed a general wetting boundary condition for phase field simulations on the nanoscale,

$$\beta u_s = -\mu \frac{\partial \mathbf{u}}{\partial y} + \left(\alpha \frac{\partial C}{\partial y} + \frac{\delta w(C)}{\delta C}\right) \frac{\partial C}{\partial x}$$
 (3.8)

where β $[Pa \cdot s/m]$ is a friction factor, u_s slip velocity, \mathbf{n} the wall normal, α is a phase field parameter appearing in the free energy functional and w(C) is a function defining the surface energy on the dry or wet side of the contact line. x is the tangential direction along the solid substrate. Direct comparison between molecular dynamics simulations and phase field simulations show that this boundary condition indeed capture the slip velocity in the contact line region (Qian et al. (2004)). These simulations were made in a steady-state Couette flow, and the non-equilibrium boundary condition was used in the phase field model.

Ren & E (2007) and Ren et al. (2010) also suggested a boundary condition for macroscopic contact line simulations. Through measurements of steady—state molecular dynamics simulations they distinguished the different contributions at the contact line. They also identified a local friction factor at the contact line, and showed that the frictional force would be proportional to the force generated by having a contact angle different than the equilibrium angle. An extension of the boundary condition to be valid also within the thin film framework was presented in Ren & E (2010).

Numerical methods have been tailored with the aim to capture the multiscale nature of problems like the moving contact line. Development of such

⁵Molecular dynamics simulation performed at The University of Tokyo from an ongoing work in collaboration with Yoshinori Nakamura, Junichiro Shiomi and Gustav Amberg.

20

multiscale methods have shown some promise (E et al. (2007)), but great challenges still remain in order to have a modeling framework that directly couples a microscale and a macroscale solver for problems that vary in time and space.

CHAPTER 4

Phase field theory

4.1. Free energy

Phase field models are based on a postulate of the systems free energy. Seminal work devoted to the development of phase field theory is presented by van der Waals (1893), Chella & Vilñals (1996), Seppecher (1996) and Yue et al. (2010). In the following a phase field model will be derived based on the work by Cahn & Hilliard (1958) and Jacqmin (1999), which also forms the theoretical foundation for the numerical results presented in Part II.

Cahn & Hilliard (1958) showed, by making a multivariable Taylor expansion of the free energy per molecule, that an expression for the free energy could be derived. The first order approximation of the Taylor expansion gives what is presented here as the volumetric energy or the integral of the free energy functional, where the higher order terms are adsorbed into the coefficient (β) multiplying the gradient term. Here the free energy is defined for a system containing two binary incompressible phases, which are immiscible and represented by a concentration C. We design the total free energy, F, in such a way that two stable phases are favored,

$$F = \int \left(\beta \Psi(C) + \frac{\alpha}{2} |\nabla C|^2 \right) d\Omega + \int \left(\sigma_{sg} + (\sigma_{sl} - \sigma_{sg}) g(C) \right) d\Gamma$$
 (4.1)

a model originating from van der Waals (1893). The total free energy consists of two contributions, defined through the volume (Ω) and surface (Γ) integral. The volume integral has two parts, where the first term from the left defines the bulk and the second term the interfacial energy. $\beta \approx \sigma/\epsilon$ and $\alpha \approx \sigma\epsilon$ are positive phase field parameters depending on surface tension σ and interface thickness ϵ . $\Psi(C) = \frac{1}{4}(C+1)^2(C-1)^2$ is chosen as a double-well function where its two minima represents the two stable phases, see fig. 4.1a.

The surface integral gives the contribution to the free energy by having a solid substrate that is wet (σ_{sl}) or dry (σ_{sg}) . $g(C) = \frac{1}{4}(-C^3 + 3C + 2)$ is a higher order polynomial in C, acting as a switch between the two stable phases. For this model the two stable phases are defined at C = 1 (liquid) and C = -1 (gas), g(C) is then g(1) = 1 and g(-1) = 0. Note that the relationship for the equilibrium contact angle from Young's relation eq. 2.5 can be substituted into the integral $(\sigma_{sg} - \sigma_{sl}) = \sigma \cos(\theta_e)$.

By making a variation in the free energy with respect to the concentration, the chemical potential $\phi = \beta \Psi'(C) - \alpha \nabla^2 C$ is obtained,

$$\delta F = \int \left(\beta \Psi'(C) - \alpha \nabla^2 C \right) \delta C d\Omega + \int \left(\alpha \nabla C \cdot \mathbf{n} - \sigma \cos(\theta_e) g'(C) \right) \delta C d\Gamma$$

$$= \int \phi \, \delta C d\Omega + \int \left(\alpha \nabla C \cdot \mathbf{n} - \sigma \cos(\theta_e) g'(C) \right) \delta C d\Gamma$$
(4.2)

A new term appears in the surface integral by integrating the variation of the gradient term by parts as; $\int_{\Omega} \alpha \nabla C \nabla (\delta C) = \int_{\Omega} -\alpha \nabla^2 C \delta C + \int_{\Gamma} \alpha \nabla C \delta C$.

4.2. Evolution of fluxes

4.2.1. Decrease of free energy

From the free energy postulate given in eq. 4.1, it is clear that any perturbation in the concentration will lead to a change in free energy. The model is designed so that the free energy decreases with any change in C (Chella & Vilñals (1996)). Assuming that any variation in C with respect to time t should equal the divergence of a flux, the Cahn–Hilliard equation is recovered. By using the above defined free energy, this tells us whether the systems energy decreases in time, as expected. The flux $\mathbf{J} = -M\nabla \phi$ is modeled as the gradient in chemical potential and M [$m^4/(N \cdot s)$] is a positive mobility constant,

$$\frac{\delta C}{\delta t} = -\nabla \cdot \mathbf{J}.\tag{4.3}$$

From eq. 4.3 it is clear that $\delta C = -\nabla \cdot \mathbf{J} \delta t$, which can be introduced into eq. 4.2 giving $\delta F = \delta t \int -\nabla \cdot \mathbf{J} \phi d\Omega$. The variation in F is then,

$$\delta F = \delta t \int -\nabla \cdot \mathbf{J} \phi d\Omega + \int \delta C \left(\alpha \nabla C \cdot \mathbf{n} - \sigma \cos(\theta_e) g'(C) \right) d\Gamma. \tag{4.4}$$

Integration by parts of the first term in the right hand side of eq. 4.4, gives a boundary condition for the flux **J**. Assuming that there is no flux across the boundary $\mathbf{J} \cdot \mathbf{n} = 0$.

Similarly, we se that the perturbation on C on the boundary, δC in the boundary integral must also guarantee a decrease in F. The contribution inside the surface integral is often referred to as the wetting condition. The boundary condition for non–equilibrium wetting on Γ is defined as,

$$-\mu_f \epsilon \frac{\partial C}{\partial t} = \alpha \nabla C \cdot \mathbf{n} - \sigma \cos(\theta_e) g'(C)$$
 (4.5)

when a no–slip condition is prescribed for the velocity. $\mu_f [Pa \cdot s]$ is a positive constant and interpreted as a friction factor at the contact line. If $\mu_f > 0$ the solution allows a contact angle (θ) at the solid substrate that is different than the equilibrium angle θ_e . If $\mu_f = 0$ local equilibrium is assumed at the boundary, imposing the equilibrium contact angle. For a boundary with a no–slip condition for the velocity the second term on the left hand side drops out.

Details about the wetting boundary condition will be discussed in sec. 4.4. Introducing the relation for the wetting condition in eq. 4.5 into eq. 4.4,

$$\frac{\delta F}{\delta t} = \int -M(\nabla \phi)^2 d\Omega - \int \epsilon \mu_f \left(\frac{\partial C}{\partial t}\right)^2 d\Gamma < 0 \tag{4.6}$$

ensures a decrease of free energy with time.

4.2.2. Cahn-Hilliard and Navier Stokes equations

The complete mathematical model is given by the Cahn-Hilliard equation,

$$\frac{\partial C}{\partial t} + \mathbf{u} \cdot \nabla C = \nabla \cdot (M \nabla \phi) \tag{4.7}$$

the chemical potential (ϕ)

$$\phi = \beta \Psi'(C) - \alpha \nabla^2 C \tag{4.8}$$

and the wetting boundary condition with no-slip for the velocity,

$$-\mu_f \epsilon \frac{\partial C}{\partial t} = \alpha \nabla C \cdot \mathbf{n} - \sigma \cos(\theta_e) g'(C). \tag{4.9}$$

These equations couple with the mass conservation equation eq. 4.10 and the Navier Stokes equations eq. 4.11 for the flow of an incompressible fluid,

$$\nabla \cdot \mathbf{u} = 0, \tag{4.10}$$

$$\rho \left(\frac{\partial \mathbf{u}}{\partial t} + \mathbf{u} \cdot \nabla \mathbf{u} \right) = -\nabla S + \nabla \cdot \left(\mu (\nabla (\mathbf{u} + \nabla \mathbf{u}^T)) \right) - C \nabla \phi. \tag{4.11}$$

 $S = P - C\phi - \left(\beta\Psi(C) + \frac{1}{2}\alpha|\nabla C|^2\right)$ is the modified pressure (Jacqmin (1999)), from the potential form of the surface tension forcing that is the last term in eq. 4.11. For these equations to prescribe a well posed problem, we may prescribe the value for the velocity at the boundary of the domain though a dirchlet boundary condition then the pressure must be allowed to adjust freely through a Neumann boundary condition $\nabla S \cdot \mathbf{n} = 0$. Vice—versa if instead a Neumann boundary condition is prescribed for the velocity, the pressure should then be defined at the boundary.

In addition to the Re number and the Ca number defined in sec. 2.3, dimensional analysis identify a Peclet (Pe) number and a Cahn (Cn) number in eq. 4.7 and eq. 4.8, respectively. The Pe number is the ratio between the convective and diffusive mass transport,

$$Pe = \frac{UL}{D} = \frac{UL\epsilon}{\sigma M\psi''(C = \pm 1)} \tag{4.12}$$

where $D = \frac{\sigma M \psi''(C=\pm 1)}{\epsilon}$ is the Cahn–Hilliard bulk–phase diffusivity. The Cn number describes the ratio between the interface thickness ϵ and the characteristic length,

$$Cn = \frac{\epsilon}{L}. (4.13)$$

4.3. Phase field interface and surface tension

From the governing equations eq. 4.7 and eq. 4.8 we seek an analytical solution for the interface profile in one dimension and the dependency of the surface tension coefficient with respect to the phase field parameters α and β . In the defined system two stable phases are energetically favored, which are separated by a diffuse interface that changes smoothly but abruptly. The equilibrium interface profile is such that it minimize the free energy in eq. 4.1. Let us derive a solution of C along the coordinate ζ in equilibrium. The chemical potential in eq. 4.8 is by definition constant in equilibrium, and with our choice of the double—well function it is clear that

$$\phi = \beta \Psi'(C) - \alpha C_{\mathcal{C},\mathcal{C}} = 0. \tag{4.14}$$

 C_{ζ} and $C_{\zeta,\zeta}$ are defined as $C_{\zeta}=dC/d\zeta$ and $C_{\zeta,\zeta}=d^2C/d\zeta^2$, respectively. Eq. 4.14 is multiplied by C_{ζ}

$$\beta \Psi'(C) \cdot C_{\zeta} - \alpha C_{\zeta,\zeta} \cdot C_{\zeta} = 0 \tag{4.15}$$

and integration along the ζ direction gives

$$\int_{-\infty}^{\zeta} \left(\beta \Psi'(C) \cdot C_{\zeta} - \alpha C_{\zeta,\zeta} \cdot C_{\zeta} \right) d\zeta = \left[\beta \Psi(C) \right]_{-1}^{C(\zeta)} - \left[\frac{\alpha C_{\zeta}^{2}}{2} \right]_{-\infty}^{\zeta} . \tag{4.16}$$

At $\zeta=\pm\infty$ we have a pure phase $C=\pm1$ so that $C_{\zeta}|_{\pm\infty}=0$ and $\Psi(C=\pm1)=0$. This gives an expression relating C_{ζ} to the double–well function as,

$$C_{\zeta} = \sqrt{\frac{2\beta}{\alpha}\Psi(C)}.\tag{4.17}$$

In eq. 4.17 we require $\sqrt{\Psi(C)}$ to be positive and definite, we write $\sqrt{\Psi(C)} = \frac{1}{2}(1+C)(1-C)$ shifting the bounds for the integration of C to [0,C]. Separating the variables in eq. 4.17 and integrating with respect to C and ζ yields,

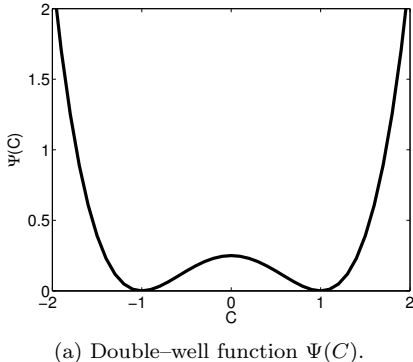
$$\int_0^C \frac{2}{(1+C)(1-C)} dC = \int_0^\zeta \sqrt{\frac{2\beta}{\alpha}} d\zeta. \tag{4.18}$$

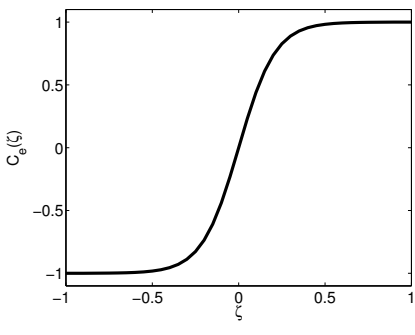
Concentration C=0 is at the midpoint of the interface at coordinate $\zeta=0$ that is the lower integration limit on the right hand side. Completing the integration of eq. 4.18 gives the equilibrium profile $C_e(\zeta)$ for a flat interface in one dimension along ζ

$$C_e(\zeta) = \tanh\left(\sqrt{\frac{\beta}{2\alpha}}\zeta\right) = \tanh\left(\frac{\zeta}{\sqrt{2\epsilon}}\right),$$
 (4.19)

where $\epsilon = \sqrt{\frac{\alpha}{\beta}}$ is defined as the thickness of the diffuse interface. The equilibrium interface profile is plotted in fig. 4.1b.

The ability to analytically derive the structure of the equilibrium interface profile has an important implication, as it enables a solution of the surface tension coefficient in the phase field model. The surface tension is defined as the excess free energy, and it is clear from the postulated free energy in eq.





(b) Equilibrium interface profile $C_e(\zeta)$.

Figure 4.1: a) Shows the form of the bulk free energy, where the two minima represents the equilibrium phases. b) Shows the interface profile of $C_e(\zeta)$ for an interface with a thickness $\epsilon = 0.15$, where $C = \pm 1$ are the equilibrium phases.

4.1 that $\Psi(C)$ gives a contribution to the free energy only in the interfacial region. By considering a one-dimensional equilibrium composition $C_e(\zeta)$ and integration of the free energy per volume along ζ direction gives the surface tension coefficient in the phase field model,

$$\sigma = \int_{-\infty}^{\infty} \left(\beta \Psi(C) + \frac{\alpha}{2} C_{\zeta}^{2} \right) d\zeta = \int_{-\infty}^{\infty} \alpha C_{\zeta}^{2} d\zeta = \frac{2\sqrt{2}}{3} \sqrt{\alpha \beta}$$
 (4.20)

relating the phase field parameters α and β to σ .

4.4. Wetting boundary condition

4.4.1. Local equilibrium

A contribution to the free energy arise from the solid boundary, see eq. 4.1. By making a variation in the free energy with respect to C eq. 4.2, the wetting condition appears. This gives a well defined boundary condition for the contact line at a solid substrate. By assuming local equilibrium at the boundary (Γ) the wetting boundary condition becomes,

$$0 = \alpha \nabla C \cdot \mathbf{n} - \sigma \cos(\theta_e) g'(C). \tag{4.21}$$

A consequence of the local equilibrium assumption is that the equilibrium angle is imposed between the interface and the solid boundary, defined on the liquid side.

So far, the derivation of the polynomial g(C) has not been described. Two restrictions of its solution have however been prescribed from the free energy, namely that is should take the value g(1) = 1 and g(-1) = 0. The polynomial g(C) is not arbitrary but also defined by the postulated form of the free energy. For simplicity we assume only a one dimensional equilibrium profile of the concentration along ζ direction, which is introduced in eq. 4.21. A sketch of the shape of the contact line foot–region is shown in fig. 4.2, where from geometrical arguments $\nabla C \cdot \mathbf{n} = \partial C/\partial y = \cos(\theta_e)C_{\zeta}$ where $\mathbf{n} = \mathbf{e_y}$. Substituting these quantities in eq. 4.21 we get,

$$\alpha \cos(\theta_e) C_{\zeta} = \sigma \cos(\theta_e) g'(C). \tag{4.22}$$

Now using the relationship for C_{ζ} given in eq. 4.17 and the definition of the surface tension coefficient in eq. 4.20 we get,

$$\sigma \frac{3}{4}(1+C)(1-C) = \sigma \frac{dg(C)}{dC}.$$
 (4.23)

Through integration of eq. 4.23 g(C) is obtained as

$$\int_{g_0}^{g(C)} dg(C) = \int_0^C \frac{3}{4} (1 + C)(1 - C) dC$$

$$g(C) = \frac{1}{4} (-C^3 + 3C + 2), \tag{4.24}$$

where the integration constants are defined from the value prescribed for g(C) when $C=\pm 1$.

Previous numerical work has shown that the equilibrium wetting boundary condition describes many flows with contact lines well, see for example Do-Quang & Amberg (2009b) and Villanueva & Amberg (2006a). A boundary condition that also captures non–equilibrium wetting can be derived, by postulating that any variation in C at the boundary should be counteracted by a diffusive flux proportional to $D_W \delta C/\delta t$. D_W $[Pa \cdot ms]$ is a rate coefficient, which was later re–defined by Carlson et al. (2012a) as $D_W = \mu_f \epsilon$ where μ_f $[Pa \cdot s]$ is interpreted as a contact line friction factor. The non-equilibrium boundary condition, first proposed by Jacqmin (1999), takes the form,

$$-\mu_f \epsilon \left(\frac{\partial C}{\partial t} + \mathbf{u} \cdot \nabla C \right) = \alpha \nabla C \cdot \mathbf{n} - \sigma \cos(\theta_e) g'(C). \tag{4.25}$$

If a no–slip boundary condition is applied on the velocity **u**, the second term on the left hand side drops out. In nanoscopic simulations the slip at the contact line might however not be neglected and the slip velocity needs to be computed through eq. 3.8.

There is one significant difference between the equilibrium and non-equilibrium wetting boundary condition from an energetic point of view. The former is not dissipative, while the latter generates a dissipation at the contact line. This has the consequence that with a $\mu_f > 0$ the contact line will move slower than with $\mu_f = 0$. Eq. 4.25 makes it possible to analytically derive a relationship for the contact line velocity. To obtain such a solution let us assume that there is no–slip at the boundary and that the contact line dynamics are completely dictated by eq. 4.25, neglecting all other contributions that might

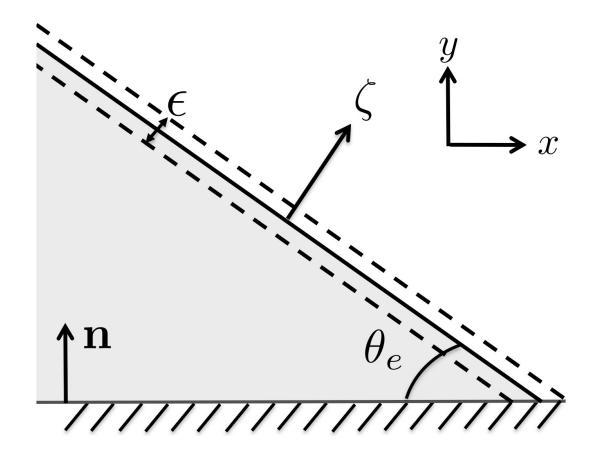


Figure 4.2: Sketch of the geometry of the interface at the wall. **n** is the normal vector on the solid, ζ is the normal direction to the interface.

affect the contact line movement. A sketch of the interface shape at the contact line is given in fig. 4.2.

Let us consider a solution where we move in the same frame of reference as the interface. Its geometry defines a shift in coordinates such that $\zeta = x \sin(\theta) + y \cos(\theta) - Ut$, where $\mathbf{n} = \mathbf{e_y}$ and ζ is normal to the interface. The normal velocity of the interface is U, where the interface geometry gives the velocity V along the tangential x direction as $U = V \sin(\theta)$. Substituting these relationships into eq. 4.25 and multiplying it with C_{ζ} on both sides and integrating gives the expression for the contact line velocity when contact line friction dominates (Yue & Feng (2011)),

$$V = \frac{\sigma}{\mu_f} \left(\frac{\cos(\theta_e) - \cos(\theta)}{\sin(\theta)} \right). \tag{4.26}$$

One peculiarity of the analytically predicted velocity from the phase field theory is that the velocity has a divergent solution for $\theta=0^\circ$ and $\theta=180^\circ$. Any influence from other contributions to the flow such as inertia or viscous dissipation are disregarded in this prediction. At the extremes of the function these other contributions are believed to regularize the contact line velocity.

In fig. 4.3 the contact line velocity predicted in the phase field theory eq. 4.26 and the linearized MKT eq. 3.6 $(V_{MK} = \frac{\lambda k_0 \sigma}{n k_b T}(\cos(\theta_e) - \cos(\theta)))$ are compared for different dynamic contact angles (θ) , assuming an equilibrium angle of $\theta_e = 45^{\circ}$. The two solutions are very different when the dynamic angle is far from the equilibrium angle.

Comparison of the form of eq. 4.26 and eq. 3.6 (MKT) shows the phase field theory to predict a friction factor that would be proportional to $1/\sin(\theta)$ within the MKT framework. The $1/\sin(\theta)$ factor introduces an additional

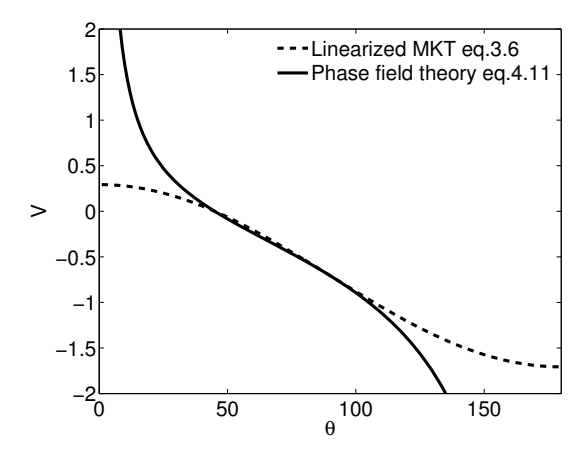


Figure 4.3: Analytical contact line velocity using $\theta_e = 45^{\circ}$, $\sigma = 20mN/m$ and $\mu_f = 20mPas$ assuming here that $\mu_f = (\frac{\lambda k_0}{nk_bT})^{-1}$. The dashed line shows the contact line velocity predicted with the linearized form of eq. 3.6 $(V_{MK} = \frac{\sigma}{\mu_f}(\cos(\theta_e) - \cos(\theta)))$ from the MKT and the fully drawn line the prediction from phase field theory eq. 4.26.

non–linearity to the function. By using values for the numerically measured μ_f and measured dynamic contact angle θ from experiments, the prediction from eq. 4.26 and eq. 3.6 was evaluated by Carlson et~al.~(2012b). Direct comparison with spreading slopes measured from the experiments show that the analytical phase field velocity eq. 4.26 predicted a spreading behavior in accordance with the experimental observation. The expression from the MKT given in eq. 3.6 did on the other hand not predict the correct spreading slope for these experiments.

CHAPTER 5

Numerical methodology

5.1. Finite Element toolbox – femLego

A finite element toolbox named femLego (Amberg et al. (1999)) has been used for the numerical simulations. femLego is an open–source symbolic tool to solve partial differential equations, where all the equations, numerical solvers, boundary and initial conditions are defined in a single Maple sheet, acting as a user-interface. One of its strong advantages is that it is easy to modify or even replace the governing equations, without the need to rewrite the source code. The variables can be discretized in space with quadratic or piecewise linear approximation functions, on tetrahedral elements. Only piecewise linear approximation functions have been used for the numerical results in this work. femLego includes adaptive mesh refinement routines, which are particularly important when solving problems that need a high resolution in certain parts of the domain, which might also move in time (Do-Quang et al. (2007)). The code runs on parallel computers, showing a good scaling behavior up to several thousands of computer process units. After compiling the Maple sheet, a C++/C and fortran77 code is automatically generated.

5.2. Numerical schemes

One of the challenges when solving the Cahn–Hilliard equation is the fourth order derivative of the concentration. Another complication is the non-linearity in C that comes from the definition of the double–well function $\Psi(C)$. Two different numerical strategies have been used to solve the Cahn–Hilliard equation, where both are based on separating the concentration and the chemical potential into two second order equations.

The chemical potential and the Cahn–Hilliard equation are discretized with piecewise linear finite elements, where the variables ϕ and C are solved in the same finite element space. The weak variational form of the equation eq. 4.8 and eq. 4.7 reads as follows;

Find $C, \phi \in H^1(\Omega)$ for all $\chi \in H^1(\Omega)$

$$(\phi, \chi) - (\beta \Psi'(C), \chi) - (\alpha \nabla C, \nabla \chi) - (\alpha \nabla C, \chi)_{\Gamma} = 0$$
(5.1)

$$\left(\frac{\partial C}{\partial t}, \chi\right) + (\mathbf{u} \cdot \nabla C, \chi) + (M \nabla \phi, \nabla \chi) - (M \nabla \phi, \chi)_{\Gamma} = 0.$$
 (5.2)

One way to solve the above coupled system of equations is to use a type of preconditioned conjugate gradient solver, described in detail in Villanueva (2007), Villanueva & Amberg (2006a). The numerical scheme consist of three steps, where the first step only solves the advection of C. The chemical potential is linearized and lumped into a symmetric matrix form. The non–convective part of C is solved inside a Conjugate Gradient (CG) loop that updates ϕ . The final step solves ϕ with a CG solver, to improve the accuracy of the numerical solution.

Another solution method is to use a non–linear method each time step. A Newton iteration method has been used (Boyanova et al. (2011) and Do-Quang & Amberg (2009b)), that solves the chemical potential and the Cahn–Hilliard equation simultaneously. This allows the system to be solved implicitly, with a backward Euler method. The solution method is as follows; the initial condition for the for the variables C and ϕ are prescribed. The non–linear problem is approximated each time step by solving a sequence of Newton iterations, consisting of a solution of the linear problem and the Jacobian matrix. The Jacobian matrix is automatically assembled in femLego. Each Newton iteration updates the solution until it reaches a preset maximum residual, see Boyanova et al. (2011).

One implication of reducing the second order derivatives in the equations by integration by parts, is that the Neumann boundary condition appears for the variables in the finite element system. No flux of chemical potential is assumed at the boundary $\nabla \phi \cdot \mathbf{n} = 0$. The wetting boundary condition appears in the chemical potential, as a Neumann condition for the concentration. Since the wetting boundary condition is already derived from the thermodynamic formulation eq. 4.9, the boundary condition for $\nabla C \cdot \mathbf{n}$ in the equation set above in weak form on the boundary Γ becomes,

$$(\nabla C, \chi)_{\Gamma} = \left(\frac{\mu_f}{\alpha} \epsilon \frac{\partial C}{\partial t}, \chi\right)_{\Gamma} - \left(\frac{\sigma}{\alpha} \cos(\theta_e) g'(C), \chi\right)_{\Gamma}$$
 (5.3)

with $\mathbf{u} = 0$ on Γ .

Since the wetting boundary condition appears naturally within the finite element formulation, it is rather straight forward to implement. It is however, slightly more complicated to treat this boundary condition with other numerical methods. One of the difficulties is to implement this boundary condition accurately, since it requires a discretization of C on the boundary whereas its value is not known. Ding & Spelt (2007), Takada et al. (2008) and Lee & Kim (2011) all used a finite difference method to discretize the equilibrium boundary condition. To obtain a discretization of the concentration gradient at the boundary they used a ghost–fluid method, with an additional set of ghost–nodes underneath the solid boundary. By approximating the values for the

concentration in the ghost–nodes, the gradient in concentration can be approximated at the solid boundary. Ding & Spelt (2007) used a criterion to identify the interfacial region, and used a fixed stencil to approximate the concentration in the ghost–node. Lee & Kim (2011), used a method of characteristics where the node points in the stencil were determined as a function of the equilibrium contact angle.

5.2.2. Navier Stokes equations

Two types of explicit projection methods have been used to solve the incompressible two-phase flow, depending on whether the phases have similar or different density. For the former case, a solution methodology similar to single-phase incompressible flow can be used. Such projection methods in general consist of two steps, which allow pressure and velocity to be solved in segregated manner. The projection method proposed by Guermond and Quartapelle (1997) has been used for such simulations (Carlson et al. (2010); Villanueva & Amberg (2006a)). Since all variables are approximated with a piecewise linear function, the velocity and pressure are solved in the same space. Restrictions by the Ladyzhenskaya-Babuska-Brezzi condition were avoided by adding a pressure stabilization term $(\epsilon_n \nabla \chi, \nabla P)$ (Hughes et al. (1986)), where ϵ_n is a small numerical parameter proportional to the mesh size.

When the two phases have different density, the standard projection scheme needs to be modified, to ensure that the mass density of each fluid particle remains unchanged as it is advected, requiring the velocity field to satisfy the incompressibility constraint. Below is a description of the projection method by Guermond & Quartapelle (2000), used to simulate incompressible two–phase flow with a density contrast. The scheme ensures mass conservation, without affecting the kinetic energy balance. This is achieved by writing the density in the evolutionary term $(\partial/\partial t)$ in the momentum equation eq. 5.7 as a product of the square root of density, with one inside and one outside the time derivative operator. The weight of density in the projection step generates an new complication.

Below the discretization of the incremental projection scheme for variable density (Guermond & Quartapelle (2000)) is presented. One modification to the original scheme is made here, namely that the continuity equation is substituted by the solution for the Cahn–Hilliard equation that conserves the C variable.

$$\begin{bmatrix}
\phi^{n+1} = \beta (C^{n+1} - (C^{n+1})^3) - \alpha \nabla^2 C^{n+1} \\
\frac{C^{n+1} - C^n}{\Delta t} + \mathbf{u}^n \cdot \nabla C^{n+1} = -M \nabla^2 \phi^{n+1}
\end{bmatrix}$$
(5.4)

the equations are solved implicitly and the brackets are used to indicate that the two equations are solved simultaneously using a Newton iteration method (Boyanova *et al.* (2011)).

The material property for each individual phase is related through an interpolation of the concentration C, where C = 1 for phase 1 and C = -1 for

phase 2. Both density and viscosity are allowed to be different in each of these phases. An example of how the material properties are interpolated is shown here for the density, but the same method is also used for the viscosity,

$$\rho = \frac{1}{2} \left(\rho_1 (1 + C) + \rho_2 (1 - C) \right) \tag{5.5}$$

 ρ_1 and ρ_2 are the density of phase 1 and phase 2, respectively.

When solving for two-phase flow with a density contrast, an additional pressure solution is required due to the weight of density. This additional step can be interpreted as a preliminary projection step giving an estimate for P^{n+1} . Q^n is an approximate pressure,

$$-\nabla \cdot \left(\frac{\nabla P^{n+1}}{\rho^{n+1}}\right) = -\nabla \cdot \left(\frac{\nabla Q^n}{\sqrt{\rho^n \rho^{n+1}}}\right). \tag{5.6}$$

The next step predicts a solution for the preliminary velocity u^{n+1} , where the non–linear advective term is made semi–implicit,

$$\sqrt{\rho^{n+1}} \left(\frac{\sqrt{\rho^{n+1}} \mathbf{u}^{n+1} - \sqrt{\rho^{n}} \hat{\mathbf{u}}^{n}}{\Delta t} \right) + \rho^{n+1} \mathbf{u}^{n} \cdot \nabla \mathbf{u}^{n+1} + \frac{1}{2} [\nabla \cdot (\rho^{n+1} \mathbf{u}^{n})] \mathbf{u}^{n+1} = -\nabla P^{n+1} + \nabla \cdot \left(\mu^{n+1} (\nabla \mathbf{u}^{n+1} + (\nabla \mathbf{u}^{n+1})^{T}) + C^{n+1} \nabla \phi^{n+1} \right).$$

$$(5.7)$$

The projection step takes the form,

$$\rho^{n+1}\left(\frac{\hat{\mathbf{u}}^{n+1} - \mathbf{u}^{n+1}}{\Delta t}\right) = -\nabla\left(Q^{n+1} - P^{n+1}\right). \tag{5.8}$$

The end-of-step, divergence free, velocity $\hat{\mathbf{u}}$ can be avoided in the scheme by taking the divergence of eq. 5.8, making use of the relation $\nabla \cdot \hat{\mathbf{u}}^{n+1} = 0$. This gives the solved projection step,

$$\nabla \cdot \mathbf{u}^{n+1} = \Delta t \nabla \cdot \left(\frac{1}{\rho^{n+1}} \nabla (Q^{n+1} - P^{n+1}) \right). \tag{5.9}$$

eq. 5.8 reads $\hat{\mathbf{u}}^n = \mathbf{u} - \frac{\Delta t}{\rho^n} \nabla (Q^n - P^n)$ at time n. $\hat{\mathbf{u}}$ is removed from the scheme by introducing its definition into eq. 5.7,

$$\begin{split} &\sqrt{\rho^{n+1}}\left(\frac{\sqrt{\rho^{n+1}}\mathbf{u}^{n+1}-\sqrt{\rho^{n}}\mathbf{u}^{n}}{\Delta t}\right)+\rho^{n+1}\mathbf{u}^{n}\cdot\nabla\mathbf{u}^{n+1}+\frac{1}{2}[\nabla\cdot(\rho^{n+1}\mathbf{u}^{n})]\mathbf{u}^{n+1}=\\ &-\nabla P^{n+1}-\frac{\sqrt{\rho^{n+1}}}{\sqrt{\rho^{n}}}(Q^{n}-P^{n})+\nabla\cdot\left(\mu^{n+1}(\nabla\mathbf{u}^{n+1}+(\nabla\mathbf{u}^{n+1})^{T}\right)+C^{n+1}\nabla\phi^{n+1}. \end{split} \tag{5.10}$$

The numerical scheme consist of four consecutive steps, eq. 5.4, 5.6, 5.10, 5.9, that solves the variables $[\phi, C, P, \mathbf{u}, Q]$. More details about the stability analysis, and theory behind the scheme, can be found in Guermond & Quartapelle (2000).

CHAPTER 6

Summary of results

This section gives a brief summary of the results presented in Part II.

Droplet dynamics in a bifurcating channel.

These results are reported in Carlson *et al.* (2010), or Paper 1 in Part II, and concerns droplet dynamic in a bifurcating channel.

Three dimensional numerical simulations based on the Cahn-Hilliard and Navier Stokes equations have been performed. First the numerical implementation was validated against two benchmark cases for a static and a dynamic drop. In the static case, the over–pressure in a drop was computed and the simulation result was compared with the Young–Laplace law. To verify that also the numerics capture accurately a dynamic case, the deformation of a single drop in a Couette flow was computed and the predicted deformation, for a set of parameters, was compared with the analytical solution by Taylor (1960). Both benchmark cases showed good agreement between the numerical results and analytical solutions.

We then proceed to investigate droplet dynamics in a bifurcating channel, a flow particular relevant for bio-medical applications. The aim here was to describe the parameter space that governs the droplet dynamics at the channel junction. Two different droplet characteristics were predicted, either splitting or non-splitting droplets.

Fig.6.1 shows four snapshots in time as a droplet comes in contact with the channel junction. At non-dimensional time T<2 the droplet travels in the straight parent channel, and around T=2 the droplet meets the junction where the parent channel bifurcates into two smaller daughter branches, see fig. 6.1a. The deformation of the interface converts work done by inertial and viscous forces into surface energy, leading to a deceleration of the droplet at the tip of the junction. But the droplet is not sufficiently stretched to initiate a type of Rayleigh-Plateau instability (for details see Berg (2010)), which would generate breakup, instead the droplet rests in an unstable quasi-steady state at the tip of the junction. The incipience of a numerical disturbance, generates a slightly asymmetric flow in the film formed between the droplet interface and the channel surface, which initiates droplet slipping (see fig. 6.1b). As the perturbation grows the droplet migrates into the lower daughter branch (fig. 6.1c). This leaves an asymmetric distribution of the phases in the daughter

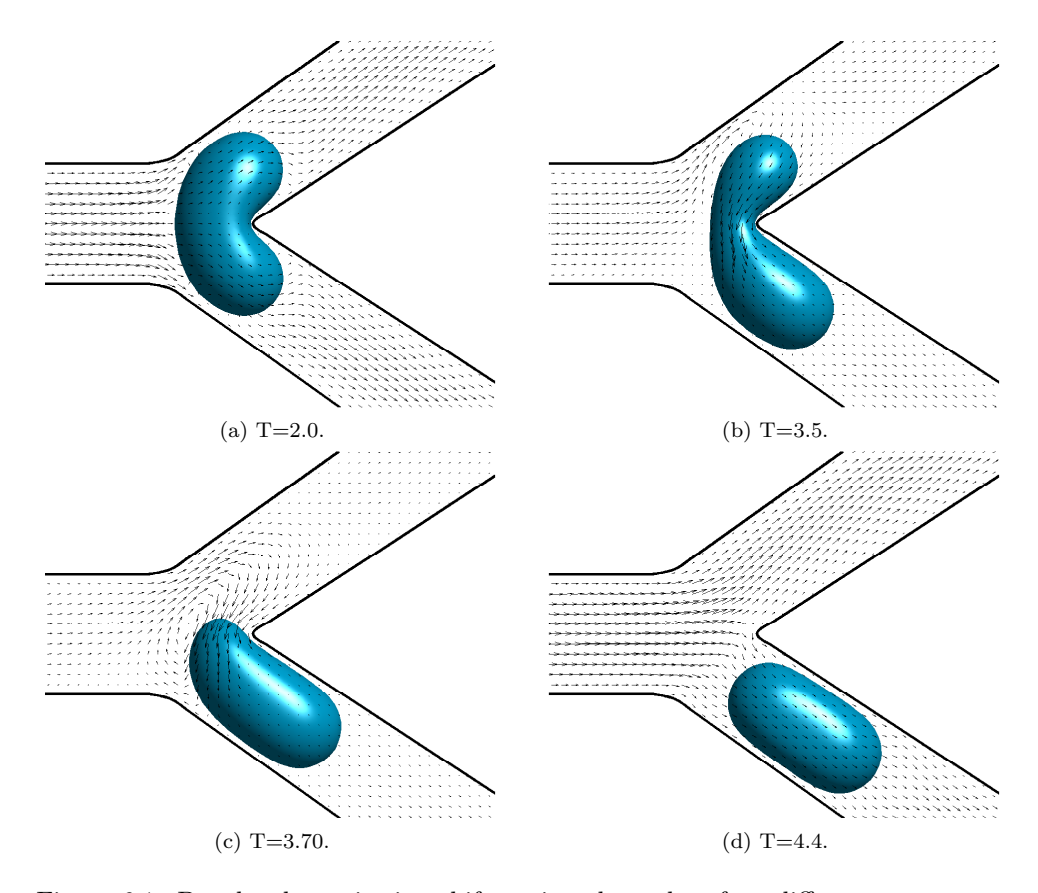


Figure 6.1: Droplet dynamics in a bifurcating channel at four different snapshots in non–dimensional time with $Ca = 1.8 \cdot 10^{-3}$ and V=0.67, in the splitting regime. The figure shows the iso–surface for the order parameter C=0 with Cn = 0.06 and the velocity vectors in the plane [0,0,1]. Fig.6 in Paper 1 in Part II.

branches and the droplet wrapping generates a flow recirculation in the upper branch. Finally the droplet travels into the lower branch, which acts effectively as a resistance to the continuous flow from the parent channel directing most of its flow into the upper branch (fig. 6.1d).

A set of simulations were performed where the Ca number and the droplet size were varied. This allowed us to predict a flow map for the two regimes, splitting and non–splitting droplet. For non–splitting droplets, a relationship was also proposed to describe the mass flow distribution of the continuous phase in the upper and lower branch, which was found to be linear with respect to the drop size.

Dynamic wetting

Four articles have been written about dynamic wetting Carlson *et al.* (2009), Carlson *et al.* (2011), Carlson *et al.* (2012a,b) or paper 2, 3, 4, 5 in Part II, where a phase field model has been developed to describe such phenomena.

Phase field models have previously been applied with success to describe flows with contact lines. However, the detailed comparison between numerical simulations and experiments of short–time dynamic wetting have been scarce in the literature. Experiments reported by Bird et al. (2008) allowed a detailed comparison with numerical phase field simulations. In Carlson et al. (2009) axis-symmetric phase field simulations of spontaneous spreading drops were compared directly with these experimental findings. The simulations revealed that a common assumption, that there is local equilibrium at the contact line, did not predict the correct contact line speed. Allowing the physics at the contact line to relax towards equilibrium, by applying a non–equilibrium boundary condition, showed that the numerics could reproduce the experimental spreading behavior.

In the non–equilibrium boundary condition a new rate coefficient appears, denoted in as D_W . This parameter is not known a-priori, and was adjusted for the simulations to match the experimental spreading radius. Not only the spreading radius was affected by the use of the non–equilibrium boundary condition, also the predicted drop shape became very different. Fig. 6.2 shows the numerical drop shape for the spreading of a water drop on three dry substrates with different wetting properties. The left panel in each subfigure shows the drop shape using the non–equilibrium boundary condition and the right panel the predicted drop shape with the equilibrium boundary condition. It is clear that the apparent dynamic contact angle is predicted to be very different for the two boundary conditions. Comparing the simulated and experimental drop shape, we notice that the shape predicted with the non–equilibrium boundary condition is in close agreement with the experimental observation.

One difference between the equilibrium and non–equilibrium wetting boundary condition is that the latter is a source of dissipation. On the macroscopic scale, as the simulations presented here, this slows the contact line motion. To better understand how this dissipation influences the spreading, we extract the three dissipative contributions (viscous \dot{R}_{μ} , diffusive \dot{R}_{D} and contact line dissipation \dot{R}_{D_W}) (Carlson et al. (2011)). Since also inertia has been proposed to govern such spreading, the rate of change of kinetic energy (\dot{R}_{ρ}) was also measured from the numerics. These four rates were compared in order to determine which contribution that dominated, as the drop spreads. Contradictory to previous interpretation that this spreading is governed by inertia, the numerics predicted the local dissipation at the contact line to give the largest contribution and dominate the spreading. How these rates evolves in time is shown in fig. 6.3, where the insets of the drop shapes correspond to the time given on the x-axis.

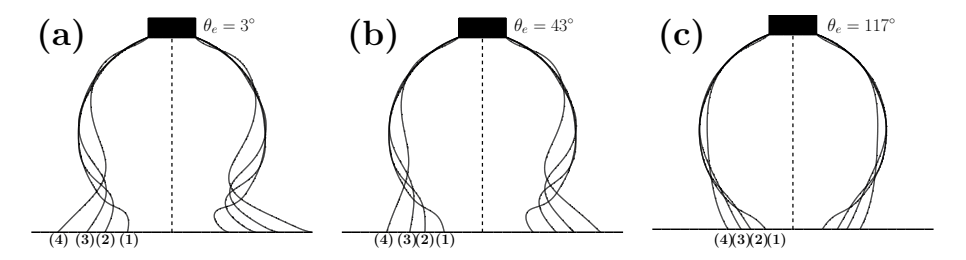


Figure 6.2: Droplet shapes at (1) t=0.4ms, (2) t=0.8ms, (3) t=1.2ms and (4) t=1.9ms, for three different surfaces: a) $D_w=1.0, \ \theta_e=3^\circ$, b) $D_w=1.4, \ \theta_e=43^\circ$, c) $D_w=0.2, \ \theta_e=117^\circ$. The right half of each panel shows the corresponding simulated result for equilibrium conditions, Dw = 0. Fig. 2 in paper 3 in Part II.

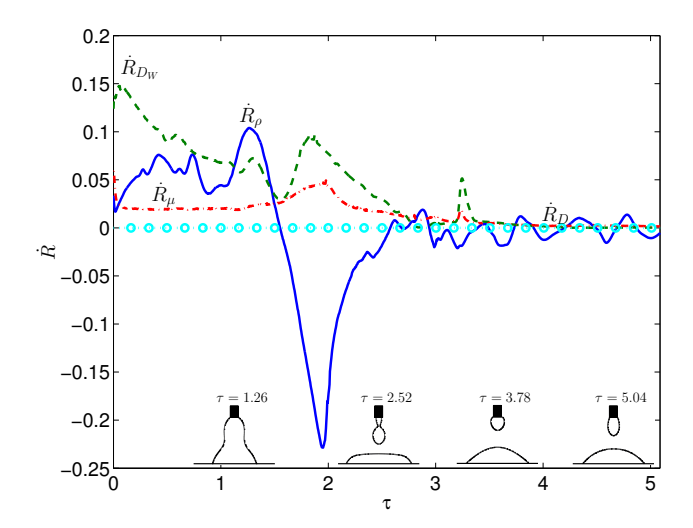


Figure 6.3: The non–dimensional rate of dissipation in time and the rate of change of kinetic energy for the spreading of a water drop $(R \approx 0.78mm)$ on a dry solid surface with $\theta_0 = 43^\circ$. The full line corresponds to \dot{R}_ρ , dashed line \dot{R}_{DW} , dashed dotted line \dot{R}_μ and the dashed line with round markers to \dot{R}_D . The insets in the lower part of the figure shows the droplet shape corresponding to the time given on the x-axis. Fig. 9 in paper 3 in Part II.

In macroscopic phase field simulations, the interface thickness (ϵ) and the Cahn–Hilliard mobility (M) needs to be taken much larger than what can be argued physically. Changes in ϵ and M are reflected in the Cn and Pe number. It is particularly important to know whether these two parameters influence

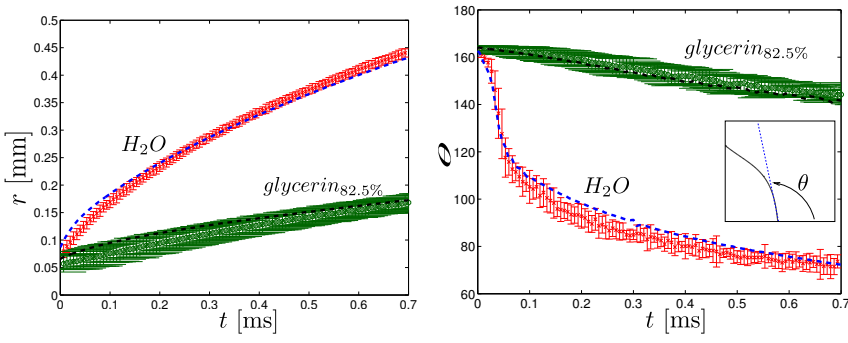
the spreading physics in simulations, and how the rate coefficient in the non-equilibrium boundary condition is affected when varying these. In Carlson et al. (2011) simulations with different interface widths indicate that the rate coefficient $D_W = \epsilon \mu_f$ is a product of the interface thickness and a coefficient μ_f , which we interpret as a contact line friction. By varying D_W with ϵ for $Cn = 10^-2$ to $Cn = 2.5 \cdot 10^{-3}$ showed that the numerical results were rather insensitive to the interface width. Also changing the mobility M (Pe number) one order of magnitude, did not have any observable effect on the simulation results.

Experiments were designed with the aim to capture even shorter timescales than reported by Bird et al. (2008) and to see the effect for a wider range of viscosities. Integration of experiments and simulations allowed thereby a measure of the contact line friction factor from the phase field theory μ_f for a wide parameter space. These results were reported in two articles Carlson et al. (2012a,b).

 μ_f was measured from the numerics by comparing directly the wetted radius and the apparent dynamic contact angle from the experiments. The same procedure was used in both the numerics and the experimental post–processing for the measurement of the apparent dynamic contact angle. The primary input in the axis-symmetric simulations are given directly from the experiment, meaning that the measured value for density, dynamic viscosity, equilibrium contact angle and surface tension are used. Fig. 6.4 shows the direct comparison of the wetted radius and dynamic contact angle predicted from the numerics and the experiments for a water drop $\mu_{H_2O} = 1mPa \cdot s$ and a glycerin–water drop $\mu_{82.5\%} = 85mPa \cdot s$. Fig. 6.4a and fig. 6.4b shows that the bulk viscosity influences both the speed of the contact line and the dynamic contact angle as it relaxes in time.

Fig. 6.5 shows a direct comparison between the drop shape predicted in simulations and in experiments, for the explored parameter space. By adjusting a single parameter the complete dynamics match between experiments and simulations. The measured contact line friction factor for the cases in fig. 6.5 are reported in tab.6.1. The value of μ_f is found for all cases to be larger than the dynamic viscosity and to depend on the solid wettability.

One interpretation of such rapid wetting is that inertia resists the spreading motion (Biance et al. (2004), Bird et al. (2008)). One aim with our experiments was to see if we could find a dependency of viscosity. One relevant non–dimensional number to predict the relative dominance between viscous and inertial forces would be the Ohnesorge number $Oh = \mu/\sqrt{\rho\sigma L}$. Oh is achieved through dimensional analysis by assuming the spreading speed follows a capillary scaling $U = \sigma/\mu$. For water, such a scaling gives a speed $U \approx 73m/s$ or $Oh \approx 0.005$, while for the most viscous liquid used in the experiments (85mPas) $U \approx 0.73m/s$ or $Oh \approx 0.4$. This should indicate that all experiments would follow an inertial scaling. Such a large difference in spreading speed for these two viscosities are however not observed in experiments, see fig. 6.4a.



- (a) Droplet radius as function of time.
- (b) The apparent dynamic contact angle θ as function of time.

Figure 6.4: a) Droplet spreading radius and b) dynamic contact angle as functions of time for a pure water and an 82.5% glycerin-water droplet. The inset in b) illustrates how the dynamic contact angle has been defined in the experiments and the simulations. The dashed curves are simulations and the points with error bars are experimental. Fig. 3 in paper 4 in Part II.

Mass fraction glycerin	0%	50%	65%	72.5%	82.5%
$SiO_2 [Pa \cdot s]$	0.15	0.33	0.51	0.66	1.02
Silane $[Pa \cdot s]$	0.17	0.26	0.33	0.41	0.80
Teflon $[Pa \cdot s]$	0.07	0.06	0.09	0.10	0.19

Table 6.1: Values for the contact line friction parameter μ_f $[Pa \cdot s]$ for different viscosities % glycerin [0, 50, 62.5, 72.5, 82.5%], $\mu \approx [1, 6.6, 14, 31, 85] mPa \cdot s$ and substrates $[SiO_2, Silane, Teflon]$, $\theta_e = [20^\circ, 60^\circ, 109^\circ]$ measured from the numerics.

Fig. 6.6a shows how the radial position of the contact line evolves in time for drops with different initial radii and for different viscosities on the oxidized Si–wafer. The markers represent the mean value after several realizations of the experiments (minimum of four) and the data set has been reduced for clarity. One observation to be made in fig. 6.6a is that the viscosity as well as the drop size influences the spreading.

Fig. 6.6b shows the same data, with the contact line radius scaled with the initial drop radius R and the time scale with a viscous capillary speed σ/μ . However, as is evident from fig. 6.6b, this scaling fails to collapse the data, so the viscous contribution does not seem to be the limiting factor in this situation. An alternative would be an inertial scaling of time based on an inertial capillary velocity scale $\sqrt{\sigma/(\rho R)}$, as shown in fig. 6.6c. As is evident here, this scaling

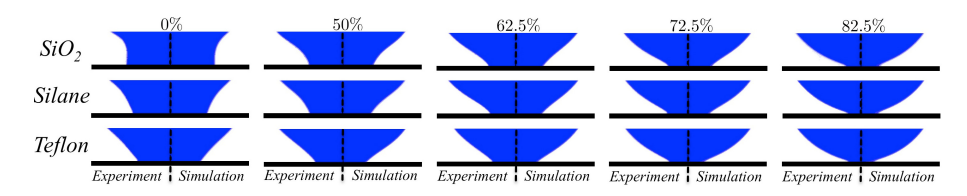


Figure 6.5: Direct comparison of experimental results and numerical simulations for five drops with an initial radius $R=(0.5\pm0.02)mm$ and 0,50,62.5,72.5,82.5% glycerin mass fraction (from left to right), spreading on SiO_2 , Silane and Teflon (from top to bottom) at time 0.33ms after start of spreading. Each panel shows a composite of experiment and simulation, where the left half is the experimental picture and the right half the numerical prediction. Fig. 2 in paper 4 in Part II.

does not capture the essential dynamics either, and we conclude that neither inertia or bulk viscosity is the limiting factor for spreading in our experiments.

The remaining possibility is a capillary velocity based on the contact line friction discussed above and quantified in tab.6.1. A representative velocity in this case can be found from dimensional analysis to be $u^* = \sigma/\mu_f$. Introducing the values for σ and μ_f from tab.6.1 gives a speed of $u^*_{0\%} \sim 4.8 m/s$ for water and $u^*_{85\%} \sim 0.6 m/s$ for 85% glycerin. By scaling time with R/u^* , we do obtain a collapse of data, for the entire range of viscosities and drop sizes, see fig. 6.6d. The scattered dimensional plot represented in fig. 6.6a is reduced nearly to a single spreading curve. Fig. 6.6 shows only results for the SiO_2 surface, but similar results are also obtained for the other solid surface coatings. The scaling law indicates a local dissipation at the contact line to dominate the short–time spreading, in accordance with the numerically measured dissipations in Carlson et al. (2011) and presented in fig. 6.3.

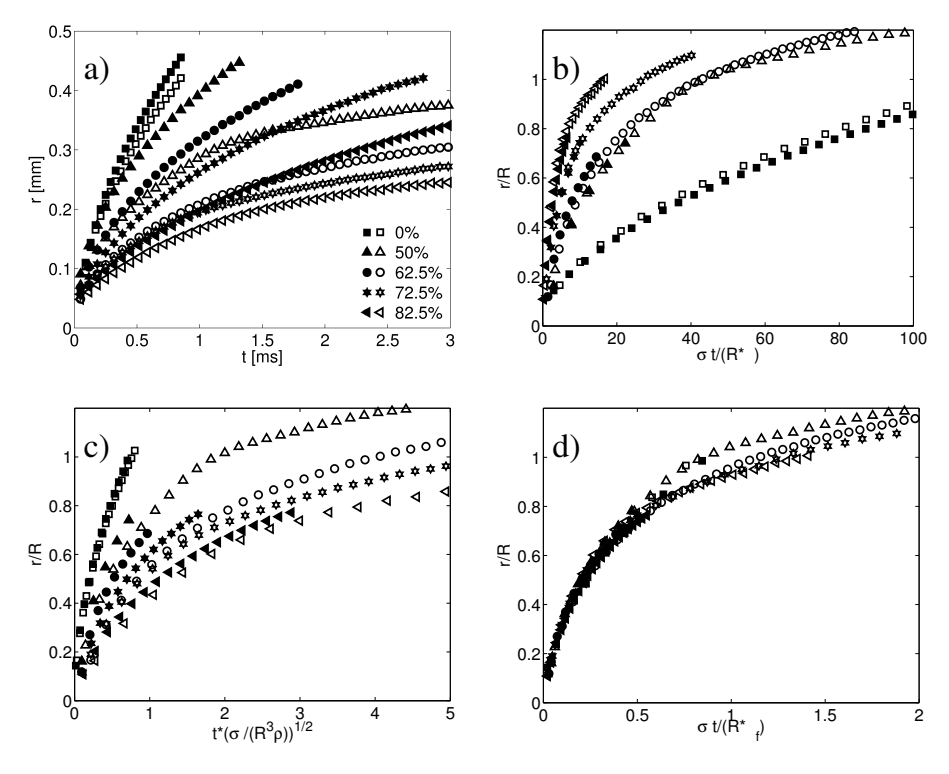


Figure 6.6: The spreading radius in time on an oxidized Si-wafer for two drop sizes $R=(0.3\pm0.02)\mathrm{mm}$ (hollow markers) and $R=(0.5\pm0.02)\mathrm{mm}$ (filled markers) for different mass fractions glycerin as indicated in the legend. (a) Dimensional units. (b) Viscous scaling. (c) Inertial scaling. (d) Contact line friction scaling. Fig. 2 in paper 5 in Part II.

CHAPTER 7

Concluding remarks

Two types of interfacial flow, droplet dynamics in a bifurcating channel and dynamic wetting, have been studied in this work, with the aim to improve the current understanding of their governing physics. Both of these flows have been studied by means of numerical simulations, based on a phase field model.

Droplets that meet a channel junction is a common occurrence in any microfluidic device, however numerical simulations of two—phase flow in such complicated geometries have so far been rather limited. We have demonstrated that by solving the Cahn-Hilliard and Navier Stokes equations with a finite element method, allowing meshing of complicated geometries, the droplet dynamics can be predicted at the tip of the channel junction. In the future this opens a window of opportunity to, probe two—phase flows in an even more challenging geometrical system, which are of great industrial relevance. Examples of such type of flows are imbibition in porous media, impact of drops on complicated substrate structures and drops that travels in microfluidic devices.

Spontaneous capillary driven spreading on dry solid substrates has been investigated in both numerical simulations and experiments. The ability to conduct both, allow a direct comparison of the two as the drop spreads. Critical evaluation of phase field simulations reveal that a common assumption of local equilibrium at the contact line predicted results, which could not rationalize the experimental behavior. This illustrates that a key ingredient was missing in the model. A non–equilibrium boundary condition, first postulated by Jacqmin (1999), was implemented and the numerical simulations reproduced the experiments. To the authors knowledge, the influence of this boundary condition in macroscopic simulations has previously been unknown.

Another important outcome of the understanding of the non–equilibrium boundary condition is that it allows a new interpretation of the physics at the contact line. Phase field theory predicts a new parameter in this boundary condition, which is interpreted here as a contact line friction factor. The friction at the contact line generates in this model a dissipation as it moves. The friction factor was measured for a wide parameter space, by direct comparison of spreading experiments and the numerical simulations. Our numerical results show that there is a significant dissipation generated locally at the contact line, which is believed to govern short–time dynamic spreading. A scaling law based on the contact line friction parameter also collapsed the experimental data set, which could not be explained by a conventional viscous or inertial scaling.

One important remark to make about phase field simulations of wetting phenomena, is that with todays state—of—the—art computational resources, we are still far from resolving all important length scales when modeling the spreading of a millimeter drop. One practical implication of the limited computational power is that in macroscopic phase field simulations, the interface width has to be taken much larger than what can be physically argued. A matter in question is whether the non—equilibrium boundary condition presented here merely compensates for the fact that all relevant length scales are not resolved. One suggestion for future work, which might bring answers to such hypotheses, would be to make a direct comparison with phase field simulations and a type of first—principle simulations, like molecular dynamics. This could even clarify the intricate nano scale physics at the contact line, which might influence or even dominate dynamic wetting.

A myriad of two-phase flow phenomena still hold scientific challenges. Many of these are also of great importance in industrial applications. Contact line hysteresis is one example of such a phenomenon. Both substrate defects and chemical heterogeneity are well known to generate contact line hysteresis, but how these influence a dynamic wetting process is yet to be quantified.

Another phenomenon of scientific interest is chemical reaction at interfaces. In many microfluidic systems droplets are used to transport different chemical components. When these droplets get close to each other or even coalesce, the different chemical species can rapidly react. This might locally modify the surface tension as well as generate an increase in temperature, which can create a non-trivial flow and even promote mixing at the micro scale.

Yet another avenue of research that holds scientific challenges is the understanding of how three phase mixtures interact with a solid. Today, a significant effort has been devoted to the modeling of two phase flow and how an interface wets a solid substrate. Development of models that accurately predict the interaction of a three phase liquid mixture and a solid substrate has so far been rather limited in the literature. Details of the physical processes that govern the dynamic interaction between oil–gas/water–gas/water–oil interfaces in conjunction with a solid is particularly relevant to the oil and gas industry. Such liquid mixtures are encountered both in the oil recovery in porous rock formations and in the cleanup of oil spills in the ocean. Plastic foams have been shown to efficiently absorb and remove oil sheen from the B. P. Deepwater Horizon 2010 oil spill accident in the Mexican Gulf. Models that describe how the oil–water–gas mixture behaves upon contact with the solid material can be invaluable for increasing the efficiency and can even promote novel design of materials to cleanup oil spills.

From a modeling perspective all of the above mentioned phenomena still lack a complete and physically sound description. Development of models through guidance of experimental observation, which could even allow a direct comparison, can open hidden doors that might disclose more of Natures physical secrets.

Acknowledgements

First of all I would like to thank my supervisor Prof. Gustav Amberg, for guiding me through my graduate studies, supporting me through every step and shearing his deep intuition in both physics and mathematics. It has been a pleasure working with Gustav, especially since he is always in a joyful mood. He has the extraordinary gift to be able to always find something positive to focus on, even in times when they are scarce. My deepest gratitude to Dr. Minh Do—Quang, for the countless discussions we have had about all aspects of research during these years and for learning me every piece of the femLego puzzle. A special thank to Prof. Truc—Nam Dinh for introducing me to scientific research and following me as mentor since the end of my Master studies. Thank to Prof. Anna—Karin Tornberg for career advice and support as my co—supervisor.

During the spring term 2011 I had the pleasure to visit Prof. Howard A. Stone and his Complex Fluids Group at Princeton University. I would like to thank Howard and the members of the Complex Fluids group for the stimulating discussions, brainstorming of new scientific ideas and fun we all had together at Princeton.

Many people have contributed to the work presented in this thesis and the scientific progress would not have been possible without all of these talented and highly skilled collaborators; Dr. Gabriele Bellani (UC Berkeley), Dr. Pilnam Kim (Korea Institute of Science and Technology (KIST)), Prof. Tapio Ala–Nissilä (Aalto University (AU)), Dr. Teemu Laurila (AU), Prof. Junichiro Shiomi (The University of Tokyo (UT)), Yoshinori Nakamura (UT), Dr. Yuan Lin (COMSOL) and Dr. Paal Skjetne (Sintef).

Next I would like to thank Dr. Daniel Ahlman, Dr. Walter Villanueva and Docent Anders Dahlkild for carefully reading the thesis and for giving valuable feedback on the writing. Thank to Dr. Johan Malm, for helping me with all practical details regarding the thesis writing and the dissertation. I also want to express my gratitude to all the past and present colleagues and friends at the Mechanics Department at The Royal Institute of Technology, which all contribute to a stimulating and friendly work place.

I would like to acknowledge funding from the Swedish Research Council through the Linnè FLOW Center, which has made this work possible. Travel grants from the Sweden–Japan Sasakawa Foundation, Stiftelsen Signeuls fond,

Linnè FLOW Center, Fonden för Erik Petersohns Minne and the GMSI program at UT, are all gratefully acknowledge.

Last, but the most I would like to thank Solvor for shearing all her love with me and making me feel very special.

Bibliography

- Amberg, G., Tonhardt, R. & Winkler, C. 1999 Finite element simulations using symbolic computing. *Mathematics and computers in simulation* **49** (4-5), 257–274.
- ANDERSON, D. M., McFadden, G. B. & Wheeler, A. A. 1998 Diffuse-interface methods in fluid mechanics Annual Review of Fluid Mech. 30, 139–165.
- Berg, J. C. 2010 An introduction to interfaces & colloids The bridge to nanoscience. World Scientific.
- BIANCE, A. L., CLANET, C. & QUÉRÉ, D. 2004 First steps in the spreading of a liquid droplet. *Physical Review E* **69** (1), 016301-1-4.
- BIRD, J. C., MANDRE, S. & STONE, H. A. 2008 Short-time dynamics of partial wetting. *Physical Review Letters* **100** (23), 234501.
- Blake, T. D. 2006 The physics of moving wetting lines. *Journal of Colloid and Interface Science* **299**, 1–13.
- Blake, T. D. & Haynes, J. M. 1969 Kinetics of liquid/liquid displacement. *Journal of Colloid and Interface Science* **30** (3), 421–423.
- BLAKE, T. D. & SHIKHMURZAEV, Y. D. 2002 Dynamic wetting by liquids of different viscosity. *Journal of Colloid and Interface Science* **253** (1), 196–202.
- BLIZNYUK, O., JANSEN, H. P., KOOIJ, E. S. & POELSEMA, B. 2010. Initial spreading kinetics of high-viscosity droplets on anisotropic surfaces. *Langmuir* **26** (9), 6328–6334.
- Bonn, D., Eggers, J., Indekeu, J., Meunier, J. & Rolley, E. 2009 Wetting and spreading. *Reviews of Modern Physics* 81 (2), 739–805.
- BOYANOVA, P., DO-QUANG M. & NEYTCHEVA, M. 2011 Efficient preconditioner for large scale binary Cahn-Hilliard models. *Technical Report Uppsala University* ISSN 1404-3203.
- Briant, A. J. & Yeomans, J. M. 2004 Lattice boltzmann simulations of contact line motion. ii. binary fluids. *Physical Review E* **69** (3).
- Brochard-Wyart, F. & de Gennes, P. G. 1992 Dynamics of partial wetting. Advances in Colloid and Interface Science, 39, 1–11.
- Bull, J. L. 2005. Cardiovascular bubble dynamics. Crititial Review Biomedical Engineering 33 (4), 299–346.
- Cahn, John W. & Hilliard, John E. 1958 Free energy of a nonuniform system. i. interfacial free energy. *The Journal of Chemical Physics* **28** (2), 258–267.

- Carlson, A., Do-Quang, M. & Amberg, G. 2009 Modeling of dynamic wetting far from equilibrium. *Physics of Fluids* **21** (12), 121701–4.
- CARLSON, A., Do-QUANG, M. & AMBERG, G. 2010a Droplet dynamics in a bifurcating channel. Int. Journal of Multiphase Flow 36 5, 397–405.
- Carlson, A., Do-Quang, M. & Amberg, G. 2011 Dissipation in rapid dynamic wetting. *Journal of Fluid Mechanics* **682**, 213–240.
- Carlson, A., Bellani, G. & Amberg, G. 2012a Dissipation in short—time dynamic wetting. EPL 97, 44004-1—6.
- Carlson, A., Bellani, G. & Amberg, G. 2012b Universality in dynamic wetting dominated by contact line dissipation. *submitted Physical Review E*.
- Chella, R. & Vilñals, J. 1996 Mixing of two-phase fluid cavity flow. *Physical Review E* 53 (4), 3832.
- Chen, Q., Rame E. & Garoff, S. 1995 The breakdown of asymptotic hydrodynamic models of liquid spreading at increasing capillary number. *Physics of Fluids* 7 (11), 2631–2639.
- Comroe, J.H. Jr. 1977 Premature science and immature lungs. Part I. Some premature discoveries. Am. Rev. Respir. Dis. 116 (1), 127–135.
- COURBIN, L., BIRD, J. C. & STONE, H. A. 2009 Dynamics of wetting: From inertial spreading to viscous imbibition. *Journal of Physics-Condensed Matter* **21** (46), 464127.
- Cox, R. G. 1986 The dynamics of the spreading of liquids on a solid surface. part 1. visocus flow. *Journal of Fluid Mechanics* **168**, 169–194.
- DE CONINCK, J., DORTONA, U., KOPLIK, L. & BANAVAR, J. R. 1995 Terraced spreading of chain molecules via molecular-dynamics. *Physical Review Letters* **74** 6, 928–931.
- DE CONINCK, J., DE RUIJTER, M. J. & VOUE, M. 2001 Dynamics of wetting. Current opinion in Colloid and Interface Science 6 (1), 49–53.
- DAVIS, T. 2004 Umfpack, an unsymmetric-pattern multifrontal method. ACM Transactions on Mathematical Software, 30, 196–199.
- DING, H. & SPELT, P. D. M. 2007 Wetting condition in diffuse interface simulations of contact line motion. *Physical Review E* **75** (4), 046708.
- Do-Quang, M., Villanueva, W., Singer-Loginova, I. & Amberg, G. 2007 Parallel adaptive computation of some time-dependent materials-related microstructural problems. *Bull. of the Polish Academy of Sciences-Technical Sciences* **55** (2), 229–237.
- Do-Quang, M. & Amberg, G. 2009a The splash of a solid sphere impacting on a liquid surface: Numerical simulation of the influence of wetting. *Physics of Fluids* **21** (2).
- Do-Quang, M. & Amberg, G. 2009b Numerical simulation of the coupling problems of a solid sphere impacting on a liquid free surface. *Mathematics & Computers in Simulation* **80** 1664–1673.
- DRELICH, J. & CHIBOWSKA, D. 2005 Spreading kinetics of water drops on self-assembled monolayers of thiols: Significance of inertial effects. *Langmuir* 21 (17), 7733–7738.
- Duez, C., Ybert, C., Clanet, C. & Bocquet, L. 2007 Making a splash with water repellency. *Nature Physics*, **3**, 180–183.
- DUVIVIER, D., SEVENO, D., BLAKE, T.D. RIOBOO, R. & DE CONINCK, J. 2011

- Experimental evidence of the role of viscosity in the molecular kinetic theory of dynamic wetting. *Langmuir*, **27**, 13015–13021.
- E, W., Engquist, B., Li, X., Ren, W. & Vanden-Eijnden, E. 2007 Heterogeneous multiscale methods: A review. *Comm. in Computational Physics*, 2 3,367–450.
- EISNER, T. & ANESHANSLEY J. 2000 Defense by foot adhesion in a beetle (Hemisphaerota cyanea). *Proceedings of the National Academy of Sciences U.S.A*, **97** (12), 6568–6573.
- EGGERS, J. 2005 Contact line motion for partially wetting fluids. *Physical Review E* **72** (6), 061605-(1-6).
- EGGERS, J. 2004 Toward a description of contact line motion at higher capillary numbers. *Physics of Fluids* **16** (9), 3491–3494.
- ESHPUNIYANI, B., FOWLKES, J. B., BULL, J. L. 2005. A bench top experimental model of bubble transport in multiple arteriole bifurcations. *Int. Journal of Heat and Fluid Flow* **26** (6), 865–872.
- DE GENNES, P. G. 1985 Wetting statics and dynamics. Review of Modern Physics 57 (3), 827–863.
- DE GENNES, P. G., BROCHARD-WYART & Quéré 2004 Capillarity and wetting phenomena Drops, Bubbles, Pearls, Waver. Springer.
- GLASSTONE, S., LAIDLER, K. J. & EYRING, H. J. 1941 The theory of rate processes. McGraw-Hill.
- Guermond, J. L., Quartapelle, L., 1997. Calculation of incompressible viscous flows by an unconditionally stable projection fem. Journal of Computational Physics 132 (1), 12–33.
- Guermond, J. L. & Quartapelle, L. 2000 A projection fem for variable density incompressible flows. *Journal of Computational Physics* **165** (1), 167–188.
- HAYES, R. A. & RALSTON, J. 1993 Forced liquid movement on low energy surfaces. Journal of Colloid and Interface Science 159, 429–438.
- HIRT, C. W. & NICHOLS, B. D. 1981 Volume of Fluid (VOF) method for the dynamics of free boundaries. *Journal of Computational Physics*, 39, 201–225.
- HE, G. & HADJICONSTANTINOU, N. G. 2003 A molecular view of Tanner's law: molecular dynamics simulations of drop spreading. *Journal of Fluid Mechanics* 497, 123–132.
- HOFFMAN, RICHARD L. 1975 A study of the advancing interface. i. interface shape in liquid—gas systems. *Journal of Colloid and Interface Science* **50** (2), 228 241.
- HOCKING, L. M. 1977 A moving fluid interface Part 2. The removal of the force singularity by a slip flow. *Journal Fluid Mechanics* **79** (2), 209–229.
- Hu, D. & Bush, J. W. 2010 The hydrodynamics of water-walking arthropods Journal Fluid Mechanics, 644, 5–33.
- HUGHES, T. J. R., FRANCA, L. P. & BALESTRA, M. 1986 A new finite element formulation for computational fluid dynamics: V. Circumventing the babuska-brezzi condition: a stable Petrov-Galerkin formulation of the stokes problem accommodating equal-order interpolations Computer Methods in Applied Mechanics and Engineering, 59 (1), 85–99.
- Huh, C. & Scriven, L. E. 1971 Hydrodynamic model of steady movement of a solid/liquid/fluid contact line. *Journal of Colloid and Interface Science* **35** (1), 85–101.

- ISRAELACHIVILI, J. N. 2011 Intermolecular and surface forces. World Scientific, 3rd edition
- JACQMIN, D. 1999 Calculation of two-phase Navier-Stokes flows using phase-field modeling. *Journal of Computational Physics* 155 (1), 96–127.
- JACQMIN, D. 2000 Contact-line dynamics of a diffuse fluid interface. Journal of Fluid Mechanics 402, 57–88.
- KOPLIK, J., BANAVAR, J. R. & WILLEMSEN, J. F. 1988 Molecular dynamics of Poiseuille flow and moving contact lines *Physical Review Letters* 60 (13), 1282– 86
- LAFUMA, A. & QUÉRÉ, D. 2011 Slippery pre-suffused surfaces. EPL 96 (1).
- Lee, H. G. & Kim, J. 2011 Accurate contact angle boundary conditions for the Cahn–Hilliard equations. *Computers & Fluids*, **44** 1, 178–186.
- Leger, L. & Joanny, J. F. 2011 Liquid spreading. Report Progress Physics 431–486.
- LINK, D. R., ANNA, S. L., WEITZ, D. A., & STONE, H. A. 2004. Geometrically mediated breakup of drops in microfluidic devices. *Physical Review Letters* **92** (5), 054503–(1–4).
- MANGA, M. 1996. Dynamics of drops in branched tubes. *Journal Fluid Mechanics* **315**, 105–117.
- MARSH, J. A., GAROFF, S. & DUSSAN, V. E. 1993 Dynamic contact angles and hydrodynamics near a moving contact line. *Physical Review Letters* **70**, 2278–2281.
- MENETRIER-DEREMBLE, L., TABELING, P. 2006. Droplet breakup in microfluidic junctions of arbitrary angles. *Physical Review E* **74** (3).
- MATSUMOTO, S., MARUYAMA, S. & SARUWATARI, H. 1995 A molecular dynamics simulation of a liquid droplet on a solid surface. *ASME/JSME Therm. Eng. Conf.* **2** (557).
- Osher, S. & Sethian, J. A. 1988 Fronts propagating with curvature-dependent speed Algorithms based on Hamiltonian-Jacobi formulations. *Journal of Computational Physics* **79**, 12–49.
- Pomeau., Y. 2011 Contact line moving on a solid. European Physics Journal Special Topics, 197, 15–31.
- Pozrikidis, C. 2001 Interfacial dynamics for Stokes flow. *Journal of Computational Physics* **169** (2), 250–301.
- Pozrikidis, C. 2012 Passage of a liquid drop through a bifurcation *Engineering* Analysis with Boundary Elements **36** (2), 93–103.
- ParkerA. R. & Lawrence C. R. 2001 Water capture by a desert beetle *Nature*, 414, 33–34.
- Petrov, P. G. & Petrov, J. G. 1992 A combined molecular-hydrodynamic approach to wetting kinetics. *Langmuir* 8 (7), 1762–1767.
- PREVOST, A., ROLLEY, E. & GUTHMANN, C. 1999 Thermally activated motion of the contact line of a liquid he-4 meniscus on a cesium substrate. *Physical Review Letters* 83 (2), 348–351.
- Protiére, S., Bazant, M. Z., Weitz, D. A. & Stone, H. A. 2010 Droplet breakup in flow past an obstacle: A capillary instability due to permeability variations. *EPL* **92** (5).
- QIAN, T. Z., WANG, X. P. & SHENG, P. 2003 Molecular scale contact line hydrodynamics of immiscible flows. *Physical Review E* **68** (1).

- QIAN, T. Z., WANG, X. P. & SHENG, P. 2004 Power-law slip profile of the moving contact line in two-phase immiscible flows. *Physical Review Letters* **93** (9).
- Quéré, D. 2008 Wetting and Roughness Annual Review in Materials Research 38, 71–99.
- Ren, W. & E, W. 2007 Boundary conditions for the moving contact line problem. *Physics of Fluids* **19** (2), 022101-1–15.
- Ren, W. & E, W. 2010 Derivation of continuum models for the moving contact line problem based on thermodynamic principles. *Comm. in Mathematical Sciences*, ISSN: 1539-6746, 9, 597.
- Ren, W., Hu, D. & E, W. 2010 Continuum models for the contact line problem. *Physics of Fluids*, 22(10):102103-1–19.
- DE RUIJTER, M. J., DE CONINCK, J. & OSHANIN, G. 1999 Droplet spreading: Partial wetting regime revisited. *Langmuir* **15** (6), 2209–2216.
- DE RUIJTER, M. J., BLAKE, T. D. & DE CONINCK, J. 1999 Dynamic Wetting Studied by Molecular Modeling Simulations of Droplet Spreading *Langmuir*, **15** (22), 7836–7847.
- DE RUIJTER, M. J., CHARLOT, M., VOUÉ, M. & DE CONINCK, J. 2000 Experimental evidence of several time scales in drop spreading *Langmuir* 16, 2363–2368.
- SEPPECHER, P. 1996 Moving contact line in the Cahn-Hilliard theory. *International Journal of Engineering Science*, **34**, 977.
- Seveno, D., Vaillant, A., Rioboo, R., Adao, H., Conti, J. & De Coninck, J. 2009 Dynamics of wetting revisited. *Langmuir* 25 (22),13034–13044.
- STONE, H. A., STROOCK, A.D. & A. AJDARI 2004 Engineering flows in small devices Microfluidics toward a Lab-on-a-Chip Annual Review of Fluid Mechanics 36, 381–411.
- SNOEIJER, J. H., DELON, G., FERMIGIER, M. & ANDREOTTI, B. 2006 Avoided Critical Behavior in Dynamically Forced Wetting *Physical Review Letters*, **96**, 174504–8
- Ström, G., Fredriksson, M., Stenius, P. & Radoev B. 1989 Kinetics of steady—state wetting. *Journal of Colloid and Interface Science* **134** (1), 107–116.
- Takada, N., Matsumoto, J., Matsumoto, S. & Ichikawa, N. 2008 Application of a Phase–Field Method to the numerical analysis of motion of a two–phase fluids with high density ratio on a solid surface. *Journal of Computational Science and Technology* 2 2, 318–329.
- Tanner, L. H. 1979 The spreading of silicone oil drops on horizontal surfaces. *Journal of Physics D* 12, 1473–1484.
- Taylor, G. I.1960 Deposition of a viscous fluid on the wall of a tube. *Journal of Fluid Mechanics* **10** (2), 161–165.
- Teshigawara, R. & Onuki, A. 2010 Spreading with evaporation and condensation in one-component fluids. *Physical Review E*, **82**, 021603.
- Thomson, P. A. & Robbins, M. O. 1989 Simulations of contact-line motion slip and the dynamics contact-angle. *Physical Review Letters* **63** (7) 766–769
- VILLANUEVA, W. & AMBERG, G. 2006a Some generic capillary-driven flows. *Int. Journal of Multiphase Flow* **32** (9), 1072–1086.
- VILLANUEVA, W., SJÖDAHL, J., STJERNSTRÖM, M., ROERAADE, J. & AMBERG, G. 2006b Microdroplet deposition under a liquid medium. *Langmuir*, **23** (3), 1171–1177.

- VILLANUEVA, W. 2007 Diffuse-interface simulations of capillary phenomena. *Phd Thesis from The Royal Institute of Technology*.
- Voinov, O. V. 1976 Hydrodynamics of wetting. *Izvestiya Akademii Nauk SSSP*, Makhanika Zhidkosti i Gaza **5** (76–84).
- VAN DER WAALS, J. 1893. The thermodynamic theory of capillarity under the hypothesis of a continuous variation of density. *J.D. Verhandel. Konink. Akad. Weten.* 1 (J. Stat. Phys., 20, 1979 (in English)).
- Wang, XP. & Wang, YG. 2007 The sharp interface limit of a phase field model for moving contact line problem. *Methods of applications and analysis* **14** (3), 287–294.
- Winkels, K.G., Peters, I.R., Evangelista, F. Riepen, M., Daerr, A., Limat, L., & J.H. Snoeijer 2011 Receding contact lines: from sliding drops to immersion lithography. *European Physics Journal Special Topics* **192**,195–205
- WROBEL, S. 2004 Bubbles, Babies and Biology: The Story of Surfactant. *The FASEB Journal* 18 (13).
- Wong, T.-S., Kang, S.-H., Tang, S. K. Y, Smythe, E. J., Hatton, B. D., Grinthal, A. & Aizenberg, J. 2011 Bioinspired self-repairing slippery surfaces with pressure-stable omniphobicity *Nature* 477, 443–447.
- Yue, P., Zhou, C. & Feng, J.J. 2010 Sharp-interface limit of the Cahn-Hilliard model for moving contact lines. *Journal of Fluid Mechanics* **645** (1), 279 294.
- Yue, P. & Feng, J. J. 2011. Wall energy relaxation in the Cahn–Hilliard model for moving contact lines *Physics of Fluids* **23**, 012106-1–8.
- Yue, P., & Feng, J.J. 2011 Can diffuse—interface models quantitatively describe moving contact lines? European Physics Journal Special Topics 197, 37–46.
- Unverdi, S. O. & Tryggvason, G. 1992 A front-tracking method for viscous, incompressible, multifluid flows. *Journal of Computational Physics* 1, 25–37.

Part II

Papers

Paper 1

Droplet dynamics in a bifurcating channel

By Andreas Carlson, Minh Do-Quang and Gustav Amberg

Linné FLOW Centre, Department of Mechanics, The Royal Institute of Technology, 100 44 Stockholm, Sweden.

International Journal of Multiphase Flow 36 (5), 397–405, 2010.

In the present paper we present a phenomenological description of droplet dynamics in a bifurcating channel that is based on three–dimensional numerical experiments using the Phase Field theory. Droplet dynamics is investigated in a junction, which has symmetric outflow conditions in its daughter branches. We identify two different flow regimes as the droplets interact with the tip of the bifurcation, splitting and non–splitting. A distinct criterion for the flow regime transition is found based on the initial droplet volume and the Capillary (Ca) number. The Rayleigh-Plateau instability is identified as a driving mechanism for the droplet breakup close to the threshold between the splitting and non-splitting regime.

1. Introduction

Droplet dynamics is a very common phenomenon that can be observed in everyday life, for instance during rainfall and in your kitchen sink. Due to their ubiquitous occurrence with fascinating physical phenomena they have attracted the attention of scientists for more than a century. Nonetheless, many flows involving droplets are yet not fully understood. This is a direct consequence of the complex physical picture formed by the competition between hydrodynamic and free—surface forces, in addition to the wetting phenomenon that governs the nature of the interaction between the interface and the solid surface.

During the last decade there has been a rapid growth of droplet microfluidic applications, which has resulted in an increased interest in flow physics at the micro scale. In these applications it is of utmost importance to obtain well-defined droplet behaviors as they traverse geometrically complex networks of channels.

One avenue of droplet microfluidics is the use of droplets as compartments for a desired physical phenomenon such as mixing, as shown by Garstecki, Fischbach, and Whitesides (2005). Mixing in micro scale is a well-known obstacle, since it is merely driven by molecular diffusion. One direction to follow in order to foster mixing is emulsion, which can be realized by design of droplet—droplet interaction. The potential use of an emulsion technique is often limited by the

possibility to precisely control the droplets size distribution. Passive droplet formation, in a device requiring no moving parts, have been demonstrated in a flow focusing device by Anna, Bontoux, and Stone (2003) and by geometrically mediated droplet division in a λ junction (Menetrier-Deremble and Tabeling (2006)) and droplet formation in T-junctions (Link et al. (2004)). Droplets can also be introduced in microfluidic devices to perform specific tasks, where they have shown promise as flow parameters to perform logical operations (Prakash and Gershenfeld (2007)) and used to code/decode various signals (Fuerstman, Garstecki, and Whitesides (2007)).

The importance of understanding droplet and bubble dynamics in complex networks goes well beyond its relevance to design and applications in microfluidic technology. They are also widely encountered in medical technology where they are used as vehicles for drug transport, part of medical treatment strategies (gas embolotherapy) or an undesired bi-product of a clinical treatment (air embolism). Air embolism occurs as an air bubble enters the vascular system that may have a dangerous or even fatal outcome, if appropriate measures are not taken. As the bubble traverses through the vascular system it might lodge in one of its micro-circulations occluding the natural blood flow, causing ischemia (Bull (2005)). If a bubble should be trapped in one of the critical sections in the body such as a capillary in the brain or in a coronary circulation the outcome could be disastrous. Embolotherapy on the other hand is a medical treatment strategy that exploits bubbles and their free surfaces (Bull (2005)), where a bubble is introduced in order to occlude the blood flow to certain parts of the tissue thus excluding its oxygen supply.

The medical relevance of embolism and embolotherapy has initiated experimental investigations of bubbles in artery and capillary geometries (Calderon, Fowlkes, and Bull (2005), Calderon et al. (2006) and Eshpuniyani, Fowlkes, and Bull (2005)), in an attempt to predict which blood vessel it will occlude. Different flow regimes for bubble splitting and lodging were observed. Eshpuniyani et al. (2005) found the non–splitting bubbles to be sensitive to gravity, with regard to which branch it would choose to lodge into. Baroud, Tsikata, and Heil (2006) made a similar observation about the disturbance sensitive nature of slug flow in a symmetric Y-junction. For velocities above a certain threshold the long, low viscous, liquid plugs divided asymmetrically as they propagated into a junction that was filled with air. The initial perturbation was believed to originate from a small imperfection, near the tip of the bifurcation, in the fabrication of the channel, as the fastest finger was always associated with the same branch.

In contrast to the vast amount of experimental results on droplet and bubble transport in complex geometries the literature on numerical experiments is scarce. Historically, computational multifluid dynamics has been restricted to rather simple geometries. As a result there is available today a great deal of knowledge about droplet and bubble dynamics in straight pipes and channels (Bretherton (1961), Taylor (1960), Aussillous and Quere (2000)). Numerical

prediction of two phase flows in T-junctions have been previously demonstrated by van der Graaf et al. (2006) with the Lattice Boltzman method and, low resolution simulations, performed by De Menech et al. (2008), De Menech (2006) with the Phase Field method. We recognize that numerical results on droplet dynamics in Y-junctions are elusive. Manga (1996) investigated the motion of drops in a Y-junction with equally sized daughter branches with the boundary-integral method (Pozrikidis (2001)). He based his analysis on the assumption of a channel flow of Stokes type ($Re \ll 1$). His two–dimensional simulation results indicated that the drops have a tendency to follow the channel branch with the highest flow rate, and that two drops could interact at the tip of the bifurcation. Such a droplet–droplet interaction points at a plausible mixing effect by emulsification.

In order to numerically capture all physical aspects of droplet dynamics in complex geometries there are several obstacles that need to be overcome both in terms of modeling and in the numerical treatment. First, such simulations should rest on a physically sound description and numerically consistent treatment of complex wetting phenomena and free surface forces. The computational technology needs to be able to handle two or more phases with different densities and viscosities that undergo topology changes such as droplet breakup. We also need the capability to deal with numerical domains of unstructured meshes. Solving the Cahn–Hilliard and the Navier Stokes equations with a finite element method appears as a computational platform realizing these requirements, opening a window of opportunity for numerical experiments on interfacial dynamics in complex geometries.

In the present paper we aim to elucidate parts of the physics governing droplet dynamics in bifurcating channels. Our investigation is based on three–dimensional numerical experiments by solving the Cahn–Hilliard and the Navier Stokes equations with a finite element method. A multiphase flow consisting of two binary immiscible liquids is simulated in a bifurcating channel, which is frequently encountered in medical technology and microfluidic applications.

We seek in particular to define the parameter range that controls the resulting droplet dynamics. In other words, for what critical condition does the droplet split or not as it interacts with the tip of the bifurcation. To reduce the number of parameters that might affect such phenomena and to isolate effects from the capillary force, we consider here two phases with equal density and viscosity. In what follows we will show that a type of Rayleigh-Plateau instability, which is not captured in two-dimensional simulations (Pozrikidis (2001)), can be a driving mechanism for droplet breakup. Two distinct flow regimes are characterized, splitting and non-splitting droplets. A relation between the two regimes has been identified, based on the initial droplet size and the Capillary (Ca) number. We find the non-splitting flow regime to inherit an unstable nature, which has a direct impact on the mass flow distribution in the channel branches.

2. Mathematical formulation

2.1. The phase field theory

The phase field theory is based on the thermodynamical consideration of the free energy of a binary system. The two components are here assumed to be immiscible and separated by a narrow diffuse interfacial region. By considering that two immiscible components actually mix over an interfacial region van der Waals (1893) proposed the idea of a diffuse interface. The composition profile of the interface can be seen as the competition between the random molecular motion and the molecular attraction.

Cahn and Hilliard (1958) derived the free energy by making a multivariable Taylor expansion about the free energy per molecule,

$$f = \beta \Psi(C) + \frac{\alpha}{2} |\nabla C|^2 \tag{1}$$

following here the phase field derivation and notation by Jacqmin (1999) where C is an order parameter. The creation of an interface is established by the competition between the bulk free energy $\beta\Psi(C)$, and the interfacial energy $\frac{\alpha}{2}|\nabla C|^2$ due to composition variations. α and β are constants that comes out directly from the Taylor expansion, see Cahn and Hilliard (1958), and are proportional to the surface tension coefficient σ and the interface width ϵ , $\beta \sim \frac{\sigma}{\epsilon}$ and $\alpha \sim \sigma \epsilon$. The free energy functional Ψ and the phase field parameters α , β and the mobility M control the interfacial dynamics and width. Ψ is taken as a double–well function, $\Psi(C) = \frac{1}{4}(C+1)^2(C-1)^2$, which will give the two equilibrium states at $C=\pm 1$. Integration over the volume of the systems gives the total free energy defined by $F = \int_{\Omega} f dV$. The functional derivative of F with respect to the order parameter C gives rise to the chemical potential,

$$\phi = \frac{\delta F}{\delta C} = \beta \Psi'(C) - \alpha \nabla^2 C. \tag{2}$$

By minimizing the chemical potential with respect to C we obtain the equilibrium profile to the interface, here given in one dimension as $C_0(x) = \tanh(\frac{x}{\sqrt{2\epsilon}})$. $\epsilon = \sqrt{\frac{\alpha}{\beta}}$ is the mean field thickness and the surface tension is defined by the integral,

$$\sigma = \alpha \int_{-\infty}^{\infty} \left(\frac{dC_0}{dx}\right)^2 dx = \frac{2\sqrt{2}}{3} \alpha^{\frac{1}{2}} \beta^{\frac{1}{2}}.$$
 (3)

By taking into account the effects of the fluids motion a convection–diffusion equation is obtained, also referred to as the Cahn–Hilliard equation

$$\frac{\partial C}{\partial t} + \mathbf{u} \cdot \nabla C = \nabla \cdot (M \nabla \phi) = \nabla \cdot \left(M \nabla (\beta \Psi'(C) - \alpha \nabla^2 C) \right), \tag{4}$$

where the mobility M is considered as a constant. We require that there is no flux of the chemical potential through the boundaries of the domain, which is fulfilled by the Neumann boundary condition

$$\frac{\partial \phi}{\partial \mathbf{n}} = 0,\tag{5}$$

where \mathbf{n} is the normal vector to the boundary. The surface free energy contribution is postulated as (Carlson, Do-Quang, and Amberg (2009))

$$F_{wall} = \int \left[\sigma_{SL} + (\sigma_{SV} - \sigma_{SL})g(C) \right] dA, \tag{6}$$

where $\sigma_{()}$ is the surface energy between the three different phases; liquid (L), gas (V) and solid (S). $g(C) = 0.5 + 0.75C - 0.25C^3$ is a smooth function between zero and one, and its derivative g'(C) will be non-zero only at the diffuse contact line. In eq. 6 it is assumed that the interface is at or close to equilibrium as it wets the solid surface. θ_0 is the equilibrium contact angle, formed between the tangent of the interface and the solid surface, given by Young's Law; $\cos(\theta_0) = \frac{\sigma_{SV} - \sigma_{SL}}{\sigma}$. Through the variational derivative of the total free energy of the system, with respect to C, and integration by parts, the natural boundary condition for the concentration at the wall is obtained,

$$\alpha \frac{\partial C}{\partial \mathbf{n}} + \sigma \cos(\theta_0) g'(C) = 0 \tag{7}$$

governing the diffusively controlled wetting at local equilibrium (Carlson et al. (2009)).

2.2. Governing equations for the motion of the fluids

Both phases are considered as incompressible in an isothermal system,

$$\nabla \cdot \mathbf{u} = 0. \tag{8}$$

The interfacial two-phase flow is governed by Navier Stokes equations,

$$\rho \left(\frac{\partial \mathbf{u}}{\partial t} + (\mathbf{u} \cdot \nabla) \mathbf{u} \right) = -\nabla P + \nabla \cdot \left(\mu (\nabla \mathbf{u} + (\nabla \mathbf{u})^T) \right) - C \nabla \phi \tag{9}$$

where \mathbf{u} is the velocity and P is the modified pressure (Jacqmin (1999)). ρ and μ are the fluids density and dynamic viscosity, which are equal in both phases. The last term is expressing the surface tension force that is based on the model proposed by Jacqmin (1999). We impose a no–slip boundary condition at the wall $\mathbf{u}=0$ and prescribe a velocity profile at the inlet with the shape of a paraboloid. To obtain a well-posed problem we apply a Neumann boundary condition on the pressure at the inlet,

$$\frac{\partial P}{\partial \mathbf{n}} = 0. \tag{10}$$

At the outlets the pressure is defined with an essential boundary condition P = 0, and a Neumann boundary condition is used for the velocities,

$$\frac{\partial \mathbf{u}}{\partial \mathbf{n}} = 0. \tag{11}$$

2.3. Scaling laws

The governing equations are made dimensionless based on the characteristic parameters of the flow, giving the dimensionless variables (denoted by *)

$$x = L_c x^*, \ t = \frac{L_c}{U} t^*, \ P = \rho U^2 P^*, \ u = U u^*, \ \phi = \frac{3\sigma}{2\sqrt{2}\epsilon} \phi^*$$
 (12)

where L_c is a characteristic length scale and U is the reference velocity. By introducing this scaling into the Navier Stokes and Cahn–Hilliard equations we obtain their non–dimensional form, where the * notation is left out,

$$\nabla \cdot \mathbf{u} = 0,\tag{13}$$

$$\frac{\partial C}{\partial t} + \mathbf{u} \cdot \nabla C = \frac{1}{Pe} \nabla^2 \phi = \frac{1}{Pe} \nabla^2 \left(\Psi'(C) - Cn^2 \nabla^2 C \right), \tag{14}$$

$$\rho\left(\frac{\partial \mathbf{u}}{\partial t} + \left(\mathbf{u} \cdot \nabla\right) \mathbf{u}\right) = -\nabla P + \frac{1}{Re} \left(\nabla \cdot \left(\mu (\nabla \mathbf{u} + (\nabla \mathbf{u})^T)\right) - \frac{C \nabla \phi}{Cn \cdot Ca}\right). \tag{15}$$

Here four non-dimensional numbers appear:

$$Pe = \frac{2\sqrt{2}U\epsilon L_c}{3M\sigma}, \ Cn = \frac{\epsilon}{L_c}, \ Re = \frac{\rho UL_c}{\mu}, \ Ca = \frac{2\sqrt{2}\mu U}{3\sigma}.$$
 (16)

The Peclet (Pe) number expresses the ratio between advection and diffusion. The Cahn (Cn) number expresses the ratio between the interface width and the characteristic length scale. The Reynolds (Re) number expresses the ratio between the inertia and the viscous force. The Capillary (Ca) number expresses the ratio between the viscous and the surface tension force.

2.4. Computational technology

2.4.1. The numerical toolbox femLego

The computations have been carried out using the numerical toolbox femLego (Amberg et al. (1999)), a symbolic tool for solving partial differential equations. The user has full control over the mathematical modeling and the numerical solution procedure as the partial differential equations, boundary conditions and numerical solvers are all defined in a single Maple worksheet. The code inherits adaptive mesh refinement and parallel computation capabilities (Do-Quang et al. (2007)).

Due to the stiff nature of the Cahn–Hilliard equation, great care needs to be taken in the solution procedure in order to avoid numerical instabilities. The equation is treated and solved in accordance with Villanueva and Amberg (2006) with a type of preconditioned Conjugate Gradient (CG) method. The Navier Stokes equations are solved using a projection scheme, proposed by Guermond and Quartapelle (1997). The non-linear convective term is treated semi-implicitly permitting larger time steps during the computations, its linear systems for the velocies and pressure are, respectively, solved with a Generalized

Cn	0.04	0.04	0.06	0.08
Δx	0.013	0.02	0.02	0.027
P_{error}	0.6%	2.0%	0.6%	0.9%

Table 1: Deviation between the numerical and analytical pressure for different Cn numbers and mesh resolutions. Δx is the mesh spacing and P_{error} is defined as the relative error between the analytically and the numerically predicted pressure jump, $P_{error} = 100 \cdot (1 - \frac{(\Delta P)_{\text{numerical}}}{(\Delta P)_{\text{analytical}}})$.

Minimal Residual method and a CG method. A first order forward Euler scheme has been applied for the time marching and all variables are discretized in space using piecewise linear functions.

2.5. Model validation

2.5.1. The Laplace Law

In order to assure that the mathematical modeling in three dimensions is correctly implemented it has been validated against the Laplace law. The Laplace law gives an analytical expression for the pressure difference inside and outside of a static droplet or bubble submerged in a liquid. This test does in particular concern the treatment of the surface tension force that is directly balanced by the pressure force.

We have measured the pressure jump for different mesh spacing and Cn numbers. The Cn number gives the ratio between the width of the diffuse interface and the characteristic length scale in the flow, here being the droplet diameter d. The results are summarized in table(1), where we have kept the Ca=1, $Pe=3\cdot 10^{-3}$ and Re=1 fixed. These dimensionless numbers gives an analytical pressure difference $(\Delta P)_{\rm analytical}=8\sqrt{2}/3$. The numerical domain has an extension of $[2d\times 2d\times 2d]$ and an equidistant mesh has been applied. Table(1) is summarizing the relative error between the computed and analytical pressure prediction for different Cn numbers and mesh spacings, after eight time steps. It is noted that the correct pressure is immediately obtained with good agreement between the numerical and analytical solution. One trend in table(1) is that the error in pressure depends on the numerical resolution of the interface. Another observation is that the correct pressure jump is obtained even with wide interfaces.

2.5.2. Deformation of a droplet in Couette flow

The dynamic behavior of the surface tension force has also been verified by validating the numerical solution of the deformation of a three–dimensional droplet in a Couette flow. Taylor (1934) derived analytically the deformation (D) of a droplet in a shear flow in the limit of low Re numbers $(Re \ll 1)$, which

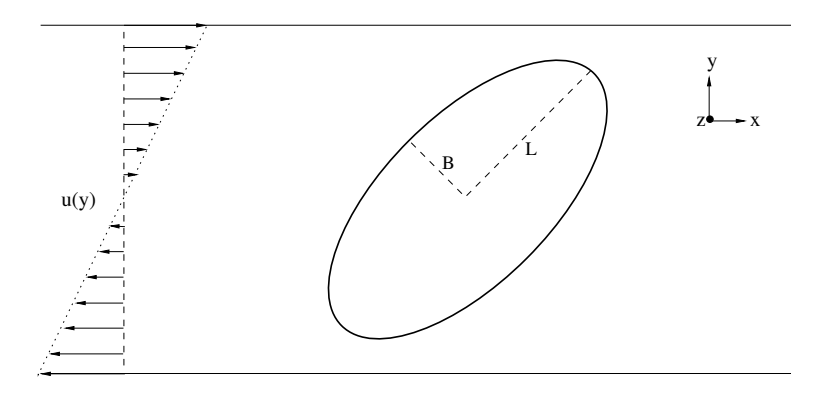


Figure 1: Illustration of the Couette flow and a description of the minor (B) and major (L) axis of a droplet at steady–state.

he also verified in experiments,

$$D = \frac{19\lambda + 16}{16\lambda + 16}Ca = \frac{L - B}{L + B}.$$
 (17)

Here the viscosity ratio of the two liquids is λ , L and B are the major and minor axes, respectively. The Ca number $Ca = \frac{\mu \dot{\gamma} d}{\sigma}$ is defined by the shear rate $\dot{\gamma}$, μ the viscosity of the continuous liquid and d the droplet diameter. The deformation parameter D can be extracted from experiments and numerical simulations by measuring the major and minor axis when the droplet has reached steadystate. A two-dimensional sketch of the domain and a schematic description of the droplets minor (B) and major (L) axis is given in fig. 1. Initially the droplet is spherical and it deforms into an elliptic shape.

Table(2) gives the relative difference between the analytical and numerical results for a droplet in a Couette flow for various Ca numbers. All results are found to be in good agreement with the analytical prediction from Taylor given in eq. 17. Fig. 2 shows the velocity vectors in a plane extracted at the center of the domain with a normal $[0 \cdot \bar{e}_x, 0 \cdot \bar{e}_y, 1 \cdot \bar{e}_z]$ and the iso–surface of C=0 is describing the droplet shape. The simulation has reached steady–state, meaning that the capillary force balances the viscous force acting on the droplet. Three stagnation points are observed in the extracted plane, one at the center of the droplet and the two others are symmetrically placed at the left and right side of the droplet, see fig. 2.

2.5.3. Geometrical description of the domain

Droplet dynamics is investigated in a three–dimensional Y–junction described by the two-dimensional sketch given in fig. 3, where the z-direction goes into the plane of the figure. A velocity profile with a shape of a paraboloid, with a non–dimensional mean velocity $\bar{u}=1$, has been prescribed at the inlet of the parent channel, and a Neumann boundary condition is defined for the pressure.

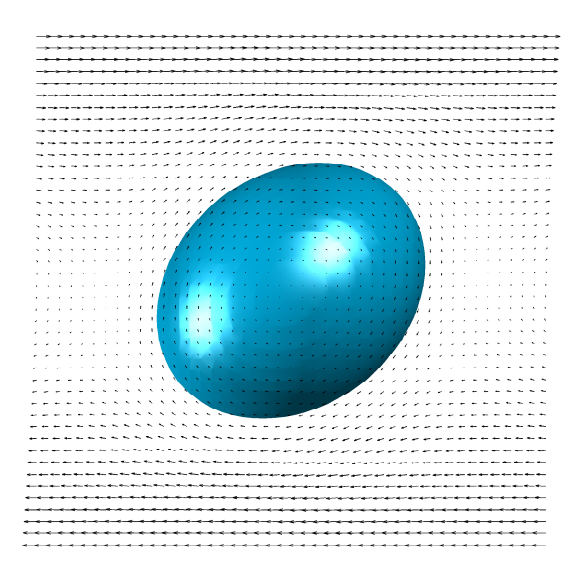


Figure 2: The two–dimensional velocity profile in the plane [0, 0, 1] and the droplets iso-contour C=0 at steady–state in a Couette flow.

Ca	0.15	0.1	0.08	0.06
D_{error}	2.8%	1.1%	0.8%	1.0%

Table 2: The relative deviation between the analytical and computed deformation parameter is given for different Ca numbers. All other parameters have been kept constant Re=0.01, $Pe=10^3$, Cn=0.06 and $\lambda=1$ and the mesh is equidistant with a spacing $\Delta x=0.02$.

A symmetric outlet condition is given for the pressure (P=0) at the upper and lower daughter branch. The parent channel has a quadratic cross section L^2 , L being the width of the channel, and the daughter branches have a rectangular cross section $L \cdot L_B$ where L is in the z-direction. The daughter to parent channel area is $\frac{L \cdot L_B}{L^2} = 0.75$ and θ is the bifurcation angle. The droplet has initially a volume V_i and the non-dimensional volume is defined as $V = \frac{V_i}{L^3}$. The walls are hydrophobic, having an affinity of the continuous phase, with an equilibrium contact angle of θ_e =180 degrees. This prevents wetting of the dispersed phase on the channel surfaces. The non-dimensional numbers given in eq. 16 are defined with the characteristic length scale chosen as the width of the parent channel $L_c = L$ and the reference velocity has been chosen as the mean velocity at the inlet.

Droplets are an important part in microfluidic applications that often consist of complex networks of channels. Microfluidic flows are laminar, but the Re

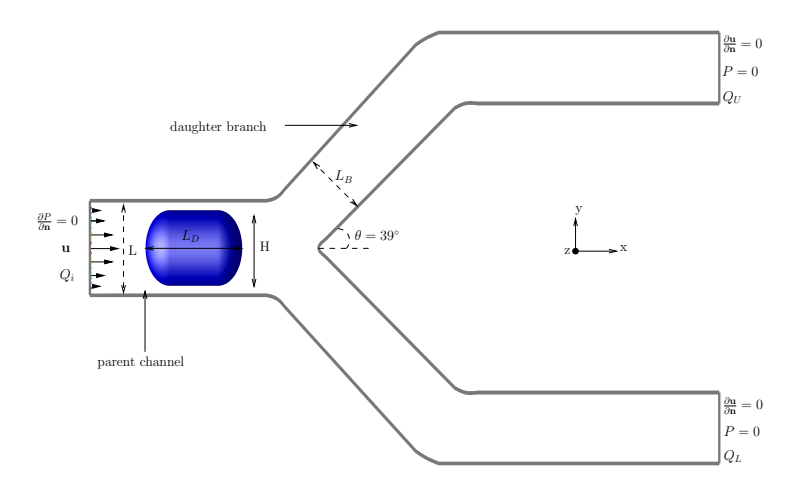


Figure 3: Geometrical description of the numerical domain.

number can be greater than unity (Song et al. (2003)) as the droplets traverses through these complex geometries. The focus here is on the detailed droplet dynamics in a generic flow configuration at small scales, a bifurcating channel, rather than simulating a whole microfluidic system. Here the Re number is small, but larger than unity Re=14.7 and $Pe=1\cdot 10^3$, both kept constant in all simulations. These non-dimensional numbers can be interpreted as a flow consisting of two immiscible liquids with, say, material properties similar to water ($\rho=10^3kg/m^3$, $\mu=0.001Pas$) with a bulk diffusion coefficient $D_B=1.47\cdot 10^{-8}m^2/s$. The continuous phase would then have a mean velocity at the inlet U=0.0147m/s and the width of the parent channel is L=1mm. These dimensions are typical of many microfluidic systems, see for instance Song et al. (2003), Calderon et al. (2005) and Eshpuniyani et al. (2005). The only material property we vary in the simulations is the surface tension coefficient for the two phases; $1.4\cdot 10^{-4} \le \sigma < 7.8\cdot 10^{-3}$ (0.1 > $Ca \ge 1.8\cdot 10^{-3}$).

The channel has an extension in the x-direction of about 10L. A nearly equidistant mesh has been employed between the inlet and the straight section (in x-direction) of the branches, with few skewed cells near the point of the bifurcation. L is discretized by 50 node points. In the straight section of the branches where they are aligned with the x-direction, has a coarse mesh with $L{\sim}10$ node points in order to reduce the computational time. The extension of the branches ensures that the droplet behavior is not influenced by the outlet boundary condition in the simulations. The mesh consists of nearly 7.5 million

tetrahedron elements and the computational time on 1024 processors for a single case was about 24 hours.

3. Freely evolving droplet dynamics

3.1. Flow regimes: splitting and non-splitting

In the quest to identify the parameters that govern the process of droplet splitting or non–splitting in the junction, a set of simulations with different Ca numbers and initial droplet size were performed. Fig. 4, 5, 6 displays the three–dimensional droplet iso-surface for C=0and the velocity field in the cross section, taken at the centre line in the channel, with a normal $[0 \cdot \bar{e}_x, 0 \cdot \bar{e}_y, 1 \cdot \bar{e}_z]$. In these three simulations the droplets have the same initial shape, as a liquid slug, with the aspect ratio $\frac{L_D}{H} = 2$, a volume V = 0.67 and Cn = 0.06.

Fig. 4 describes the temporal droplet evolution with its velocity vectors for $Ca=3.0\cdot 10^{-3}$. Fig. 4a shows the elongated droplet as it is just about to come in contact with the edge of the junction. It deforms symmetrically forming two identical liquid fingers in the upper and lower daughter branch, which almost completely fill the channel, (fig. 4b). The droplet rear forms a small curvature, with a large radius, at the entrance of the bifurcation, bulging in the upstream direction (fig. 4b). A cylindrical liquid thread is formed between the tip of the junction and the droplet rear, which drains symmetrically into the branches, see fig. 4c. As the circumference of the thread becomes less than its normal length, the surface tension force starts to contract it radially. This eventually results in a pinch–off and the formation of two equally sized daughter droplets, with a spherical shape. The two droplets propagate downstream in the channel branches, and a thin film is formed of the continuous phase, between the channel surface and the droplet interface, see fig. 4d.

Fig. 5 describes the temporal droplet evolution with its velocity vectors for $Ca = 2.2 \cdot 10^{-3}$. In comparison with the results in fig. 5 the capillary force is here just slightly stronger, resulting in an almost identical droplet shape as it approaches the junction (fig. 5a). Fig. 5b shows the droplet as it has deformed in the junction. Due to the stronger capillary force it has a larger curvature at its rear than observed fig. 4b. The deformation of the interface converts work done by inertial and viscous forces into surface energy, leading to a deceleration of the droplet at the tip of the junction. Notice that the magnitude of the velocity vectors inside the droplet is smaller in comparison with the outer flow. It stays at the junction until the incipience and growth of an instability similar to the Rayleigh-Plateau (R-P) (Rayleigh (1882)) instability. This instability appears as the length of the liquid thread exceeds its circumference, meaning that its surface area can be reduced by breakup as this is energetically favorable. The instability is here not initiated exactly at the centre of the channel, causing a slight asymmetric drainage of the liquid bridge, with a higher flow rate entering the lower branch (fig. 5c). Finally, the thread pinches off forming two droplets, where the droplet in the lower branch is slightly larger than the droplet in the upper branch (Fig. 5d).

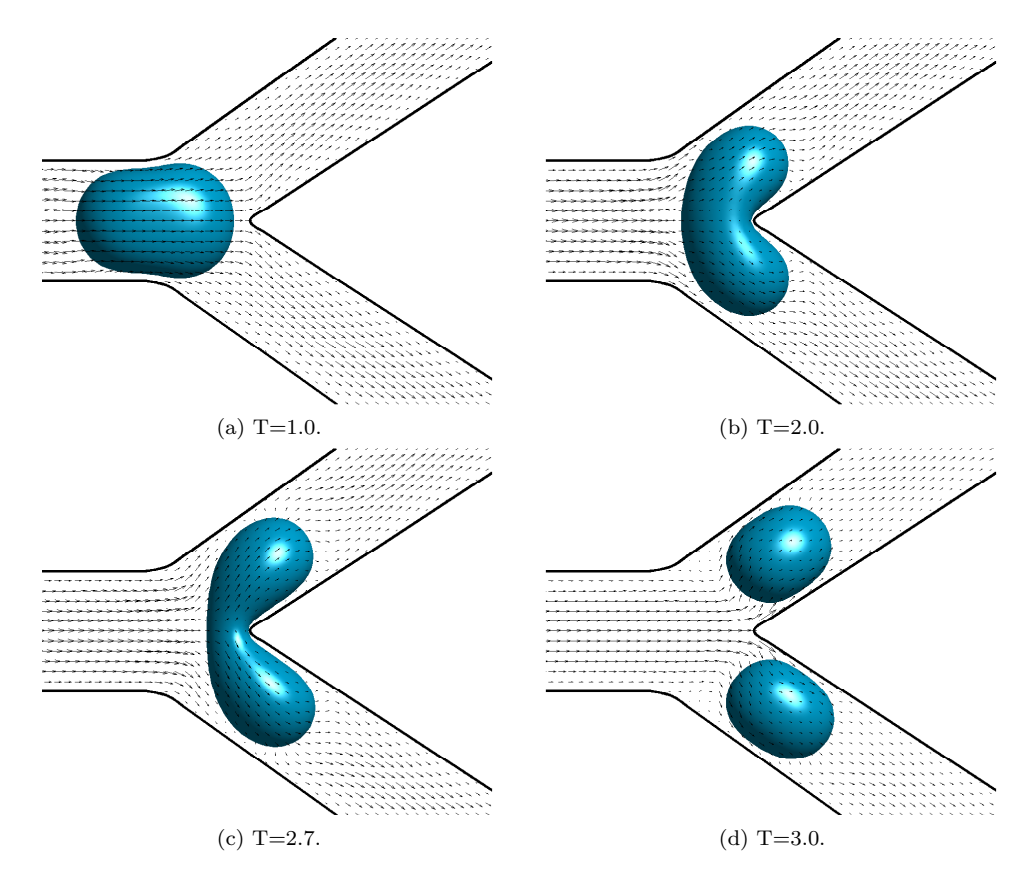


Figure 4: Droplet dynamics in a bifurcating channel at four different snapshots in time with $Ca = 3.0 \cdot 10^{-3}$ and V=0.67, in the splitting regime. The figure shows the iso-surface for the order parameter C=0 with Cn = 0.06 and the velocity vectors in the plane [0,0,1].

Fig. 6 describes the temporal droplet evolution with its velocity vectors for $Ca = 1.8 \cdot 10^{-3}$. By further reducing the Ca number, in comparison with fig. 4, 5, through an increase in the surface tension force, we observe a different droplet behavior. Initially, the droplet approaches the junction in a similar fashion as reported above. But the dominating surface tension force reduces the ability of the inertia and viscous force to deform the droplet and it obtains a quasi steady-state condition, with no internal flow, as it sticks in the junction, see fig. 6a.

Due to the stronger capillary force, a larger curvature is generated at the droplet rear, resulting in a larger radius of the liquid thread. This has a direct consequence on the resulting droplet dynamics, as the birth of a R-P instability is prevented. Although the droplet preserves this state for several hundred

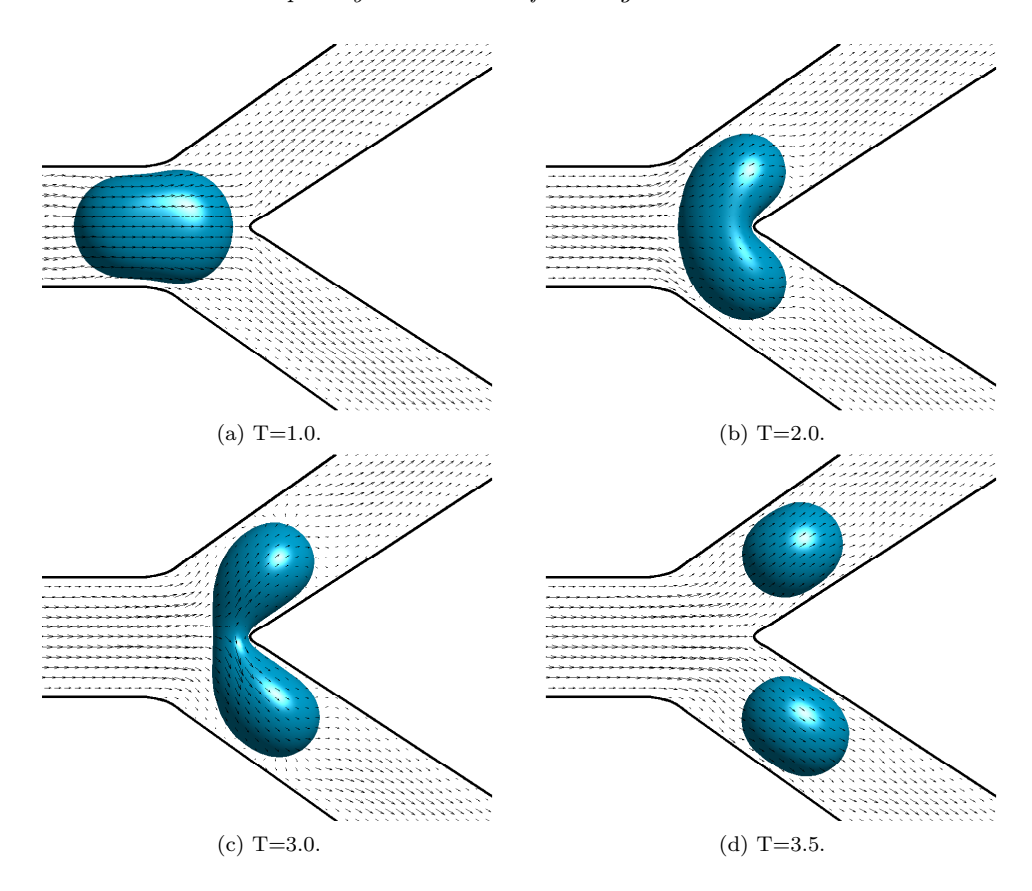


Figure 5: Droplet dynamics in a bifurcating channel at four different snapshots in time with $Ca = 2.2 \cdot 10^{-3}$ and V=0.67, in the splitting regime. The figure shows the iso-surface for the order parameter C=0 with Cn=0.06 and the velocity vectors in the plane [0,0,1].

time steps, we find this sticking behavior to inherit an unstable nature as the droplet always exits into one branch. The incipience of a numerical disturbance, generates a slightly asymmetric flow in the film formed between the droplet interface and the channel surface, which initiates droplet slipping see fig. 6b. As the perturbation grows the droplet migrates into the lower daughter branch (fig. 6c). This leaves an asymmetric distribution of the phases in the daughter branches and the droplet wrapping generates a flow recirculation in the upper branch. For flows with $Re \ll 1$ such recirculation patterns would be absent, as they would be damped by the viscosity. Finally the droplet propagates into the lower branch, see fig. 6d.

The temporal evolution of the surface area for the three cases reported above are shown in fig. 7. The vertical axis depicts the non–dimensional

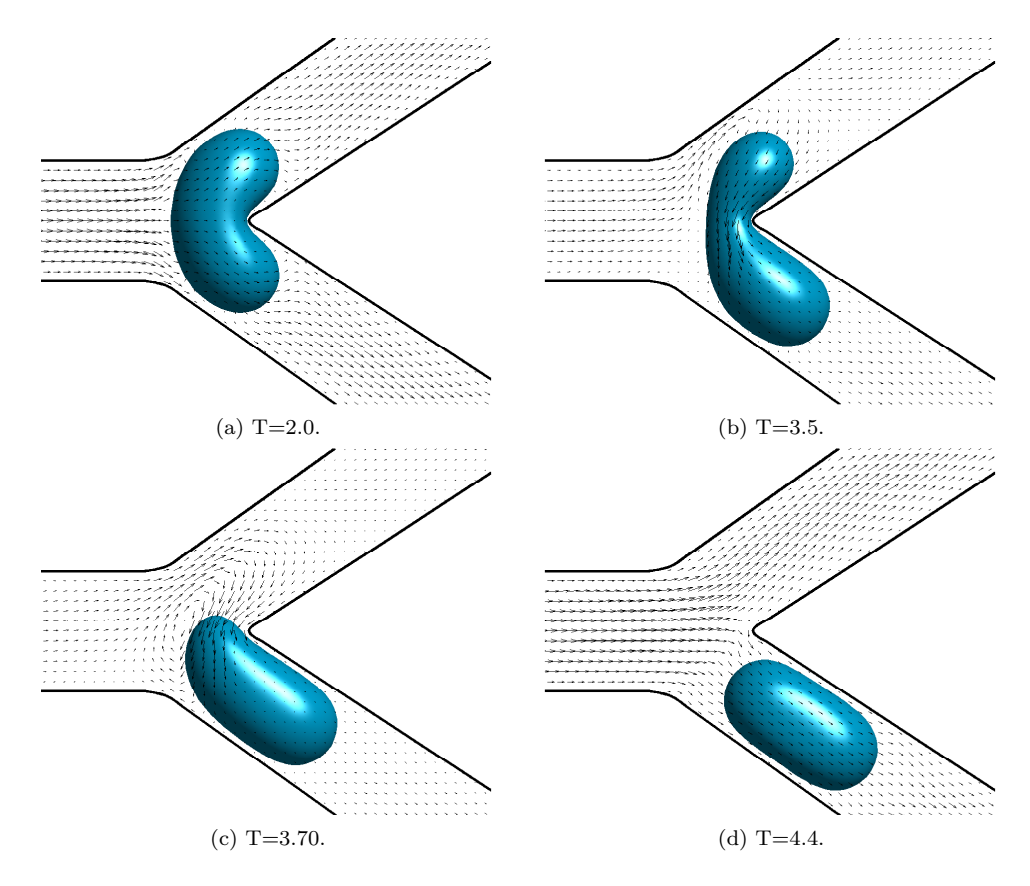


Figure 6: Droplet dynamics in a bifurcating channel at four different snapshots in time with $Ca = 1.8 \cdot 10^{-3}$ and V=0.67, in the splitting regime. The figure shows the iso-surface for the order parameter C=0 with Cn = 0.06 and the velocity vectors in the plane [0,0,1].

droplet surface area, where A_i is the initial droplet area. The droplets have initially the same shape, but different surface tension coefficients. As shown in fig. 4, 5, 6, small variations in the magnitude of the capillary force can have a large influence on the droplets ability to deform in the bifurcation. We notice in fig. 7 that their initial shape is not being energy minimized, explaining the small deviation from the value one at the first output at T=0.1. As the droplets approach the tip of the bifurcation they deform in a similar manner, with a continuous decrease in surface area. They obtain the same minimum surface area as the major part of the droplet occupies the region where the channel bifurcates, see fig. 7 at $T\sim1.5$. At this place in the channel the droplet is least confined between the walls, so that it attains a shape with a surface area being less than what it had in the parent channel. As the droplets nose interacts with

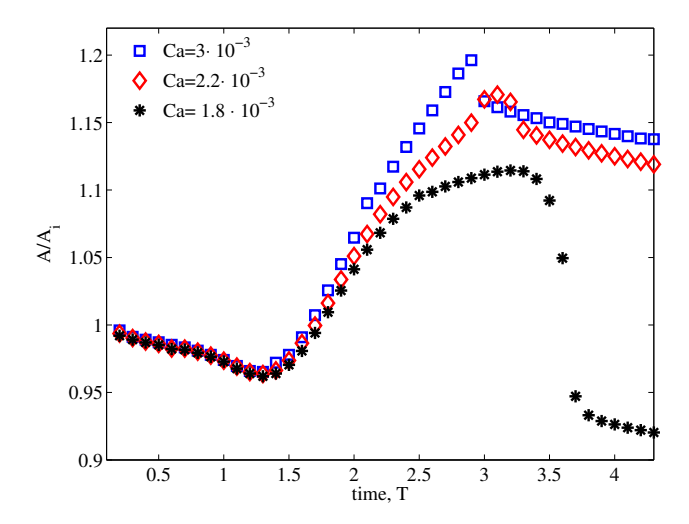


Figure 7: The temporal evolution of the surface area for three droplets with different Ca number, with V=0.67 and A_i is the initial droplet surface area.

the tip of the junction it deforms into its two branches. This leads to an increase in surface area, where the three droplets deform in a similarly fashion until the time T=2. Around this time, the effect of the different Ca numbers starts to manifest itself. The case with the lowest surface tension force $(Ca = 3 \cdot 10^{-3})$ has a linear increase in surface area from the time T=1.5 until droplet breakup at T=2.8. An abrupt change in surface area is then observed, demonstrating that splitting is energetically favorable. Afterwards, the two droplets readjust into their equilibrium shape as they propagate into the two daughter branches.

For the case with $Ca = 2.2 \cdot 10^{-3}$ the slope of the surface area in time becomes different around time T=2. Here the surface force becomes comparable with the inertia and the viscous forces acting on the droplet, which increases the deformation. The change in Ca changes also the temporal timescale in the flow, and breakup takes place at T=3.1.

The non-splitting droplet ($Ca = 1.8 \cdot 10^{-3}$) has a different behavior than the two cases with lower surface tension coefficients described above. Its surface area increases up to around time T=2.4, then its growth almost ceases with just a small change in surface area until T=3.3 when the droplet stops at the tip of the bifurcation, see fig. 6, 7. Around T=3.3 the droplet starts to wrap into the lower branch, having a large effect on its surface area that rapidly reduces by around fifteen percent between time T=3.2 and T=3.7. As the droplet has migrated into the lower branch it adjusts into its energy minimizing shape, obtaining a lower surface area than it had at time T=0. That its surface area is less in the smaller branch than in the larger parent channel may seem counterintuitive. This is due to that the speed in the channel

containing the droplet is decreased, giving a lower local Ca, and thus a smaller droplet distortion.

 Q_i , Q_U and Q_L are the mass fluxes through the inlet, upper and lower outlet, respectively, see fig. 3. Fig. 8 shows how the non-splitting droplets influence the mass flow distribution in the junction. The figure describes the ratio between the outflow in the upper branch (Q_U) , which is not occupied by the droplet, and the inflow (Q_i) . It should be noted that by monitoring the ratio between the lower branch and the inlet produces a symmetric plot as seen in fig. 8. The splitting droplets, of equal size, produce a symmetric outflow of the two daughter branches. The asymmetric effect generated by the non-splitting droplets is clearly demonstrated in fig. 8 and portray that the droplets, although having the same density and viscosity as the continuous phase, acts as a flow resistance in the branch they occupy. This effect is primarily generated by the interface, which is sensed by the outer flow. We note that such an observation has also been made in droplet experiments performed by Garstecki et al. (2005). The blue hollow circles describe the mass flow ratio, in this context, of a large droplet, which does not obtain a steady outflow before entering the section of the branch that is aligned with the x-direction. Nonetheless for smaller droplets one can observe in fig. 8 that there is a dependence on the droplet size and the distribution of the continuous phase in the two branches. These results reveal that the flow ratio between the upper and lower branch converge towards a constant value, depending on droplet size.

By monitoring the outflow ratio in time we can observe the effect of the perturbation as the droplet wraps into the branch. This is illustrative for the two cases where the droplet has the same size (V=0.52), but different Ca numbers. For these cases the path to the final outflow distribution between the branches are highly different, but their final value is nearly the same. This also shows, for the parameters space investigated here, that the Ca number plays a minor effect with regard to the outflow ratio, see fig. 9.

By plotting the final outflow ratio between the upper and lower branch, we find the relationship for the flow resistance that is dependent on the droplet size, see fig. 9. The outflow ratio is found to depend linearly on the droplets volume, the dashed line in fig. 9 is described by $\frac{Q_U}{Q_L} = 0.94 + 0.70V$. The large droplet, see blue hollow circles fig. 8, have been disregarded here as the outflow ratio does not reach steady-state in the branch.

3.2. Flow regime map

The droplet splitting or non–splitting phenomenon depends mainly on the relative dominance of the surface tension force, represented in the Ca number. The resulting droplet dynamics seem to also highly depend on its initial configuration, identifying the droplet size and the Ca number as two of the key parameters for the definition of the multiphase flow characteristics in the junction. Similar experimental observations have been made in both T- (Link

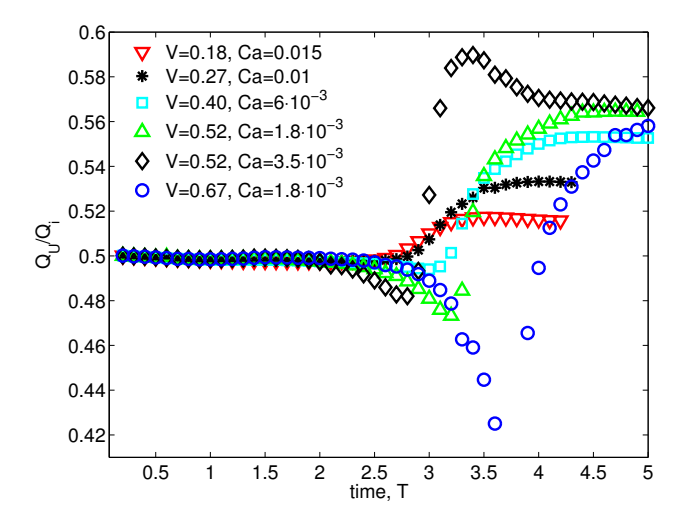


Figure 8: The mass flow ratio between the upper outflow branch and the inflow, where the vertical axis describe the outflow ratio $\frac{Q_U}{Q_i}$.

et al. (2004)) and λ -junctions (Menetrier-Deremble and Tabeling (2006), Eshpuniyani et al. (2005)). These parameters form a non–dimensional space, which is explored in numerical experiments, describing the relationship between the splitting and non–splitting flow regimes as shown in fig. 10.

Note in particular that there seem to be a distinct, well-defined, condition for the flow regime transition between splitting and non-splitting droplets. Close to this threshold we recognize that a slight variation in droplet size or the surface tension force could have a tremendous affect on the flow physics in the junction. These findings identify that large droplets favor splitting and that such a process is hard to obtain with small droplets. Strikingly, the threshold for splitting or non-splitting falls on a single curve given by $V = -0.79 - 0.53 \cdot \log(Ca)$, see fig. 10.

The red circles in fig. 10 represent the results for simulations with a thicker interface Cn=0.08. We note that the criterion for splitting and non-splitting changes with the interface width. Close to the splitting/non-splitting threshold it is expected that even small changes in parameters, like the interface width, will have an effect on the results. By reducing the interface width the splitting curve might shift slightly towards higher Ca numbers, although the shape of the curve and the actual interfacial dynamics are not believed to change significantly.

There are some salient points that need to be emphasized. We note that the disturbance initiating droplet motion into the lower branch in the nonsplitting regime has a numerical nature. Flows involving droplets that will not split or rigid particles that enter a bifurcation are inherently unstable. Here the

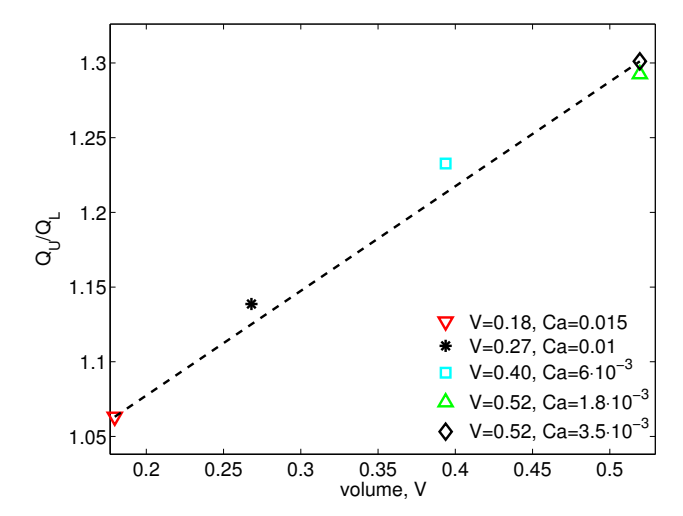


Figure 9: The droplet volume V is plotted against the mass flow distribution between the upper and lower branch $\frac{Q_U}{Q_L}$. The dotted line is added as a guide to the eye. A linear relationship between the mass flow ratio and volume is found to be approximated to; $\frac{Q_U}{Q_L} = 0.94 + 0.70V$.

droplet always enters the same branch, demonstrating that the perturbation is numerically consistent for all cases. One hypothesis for the perturbations is that there is a slight asymmetry in the mesh near the point of bifurcation. Another explanation could be that this effect is caused by the convergence criteria, even though they are small at each time step ($\epsilon \sim 10^{-7}$) they are of finite size and accumulate in time. In order to quantify the magnitude of the perturbation needed to control the droplet motion, we introduce a small asymmetry between the two outlet boundary conditions. This is done in practice by restarting the simulations from a state when the droplet sticks in the junction, placing a small variation between the pressure outlets. We observed that the droplet change branch when a pressure difference of $\Delta P = \frac{P_{upper} - P_{lower}}{P_{ln}} \sim 0.04$ is placed between the two branches, where P_{in} is the inlet pressure at the restarted time step. This indicates the disturbance sensitivity nature of the non-splitting flow regime and illustrates that the symmetric placement of a drop at the junction is highly unstable. Experimentally such unstable two phase flow phenomena have been observed in similar geometries by Baroud et al. (2006) and Calderon et al. (2005).

4. Conclusion

The present paper reports on three–dimensional numerical experiments based on phase field theory of droplet dynamics in a bifurcating channel with symmetric outflow conditions. Two distinct flow regimes are identified as the droplets

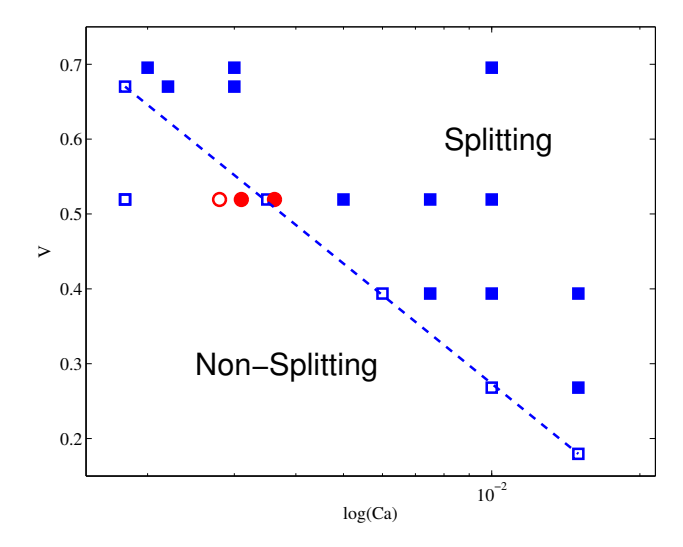


Figure 10: Semi-logarithmic map of the splitting and non–splitting flow regime, the dotted line has been added as a guide to the eye. The square markers are results with Cn=0.06 and the circles Cn=0.08, hollow markers denote non-splitting and filled markers splitting droplets. The dashed line describes the threshold for splitting or non-splitting approximated by $V = -0.79 - 0.53 \cdot \log(Ca)$.

interact with the junction, splitting and non–splitting. In particular we show the effects of the initial droplet size and Ca number on the resulting two-phase flow characteristics.

Droplets that split equally, produce a symmetric distribution of both phases in the channel daughter branches. Near the threshold between the two regimes, we observe that the R-P instability can be a driving parameter for droplet division.

In the non–splitting regime the droplet migrates into one of the channel branches, leading to a strong temporal asymmetric flow in the junction. A linear relationship is found for the droplet size and the outflow ratio between the upper and lower branch. By placing a small difference between the upper and lower outflow condition we demonstrate the disturbance sensitive nature of the flow. This is illustrating that a symmetric placement of the droplet in the parent channel is highly unstable.

These results identify the Cahn-Hilliard Navier Stokes equations solved with a finite element method as a viable computational platform for the description of multiphase flow characteristics in complex geometries at small scales. One prospect for the future is a further description and identification of novel interfacial dynamics. Future studies should include the influence of the tip geometry, multiple droplet interaction and wettability effects, in order to obtain more pieces of the puzzle forming the physical picture of droplet dynamics in bifurcating channels.

Acknowledgements

Computer time provided by Swedish National Infrastructure for Computing (SNIC) is gratefully acknowledged.

References

- Amberg, G., Tonhardt, R., Winkler, C. 1999. Finite element simulations using symbolic computing. *Mathematics and Computers in Simulation* **49** (4), 257–274
- Anna, S. L., Bontoux, N., Stone, H. A. 2003. Formation of dispersions using "flow focusing" in microchannels. *Applied Physics Letters* **82** (3), 364–366.
- Aussillous, P. & Quere, D. 2000. Quick deposition of a fluid on the wall of a tube. PHYSICS OF FLUIDS 12 (10), 2367–2371.
- Baroud, C. N., Tsikata, S. & Heil, M. 2006. The propagation of low-viscosity fingers into fluid-filled branching networks. *Journal of Fluid Mechanics* 546, 285–294.
- Bretherton, F. P. 1961. The motion of long bubbles in tubes. *Journal of Fluid Mechanics* **10** (2), 166–188.
- Bull, J. L. 2005. Cardiovascular bubble dynamics. Critical Review Biomedical Engineering 33 (4), 299–346.
- Cahn, J. W. & Hilliard, J. E. 1958. Free energy of a nonuniform system. i. interfacial free energy. The Journal of Chemical Physics 28 (2), 258–267.
- CALDERON, A. J., FOWLKES, J. B. & BULL, J. L. 2005. Bubble splitting in bifurcating tubes: a model study of cardiovascular gas emboli transport. *Journal of Applied Physiology* 99 (2), 479–487.
- Calderon, A. J., Heo, Y. S., Huh, D., Futai, N., Takayama, S., Fowlkes & J. B., Bull, J. L. 2006. Microfluidic model of bubble lodging in microvessel bifurcations. *Applied Physics Letters* 89 (24), 244103.
- CARLSON, A., Do-Quang, M., Amberg, G. 2009. Modeling of dynamic wetting far from equilibrium. Physics of Fluids 21 (12), 121701–4.
- DE MENECH, M. 2006. Modeling of droplet breakup in a microfluidic t-shaped junction with a phase-field model. *Physical Review E* 73, 031505-1–9.
- DE MENECH, M., GARSTECKI, P., JOUSSE, F. & STONE, H. A. 2008. Transition from squeezing to dripping in a microfluidic t-shaped junction. *Journal of Fluid Mechanics* **595**, 141–161.
- Do-Quang, M., Villanueva, W., Singer-Loginova, I. & Amberg, G. 2007 Parallel adaptive computation of some time-dependent materials-related microstructural problems. *Bulletin of the Polish Academy of Sciences-Technical Sciences* **55** (2), 229–237.

- ESHPUNIYANI, B., FOWLKES, J. B. & BULL, J. L. 2005. A bench top experimental model of bubble transport in multiple arteriole bifurcations. *International Journal of Heat and Fluid Flow* **26** (6), 865–872.
- FUERSTMAN, M. J., GARSTECKI, P. & WHITESIDES, G. M. 2007. Coding/decoding and reversibility of droplet trains in microfluidic networks. *Science* 315 (5813), 828–832.
- GARSTECKI, P., FISCHBACH, M. A. & WHITESIDES, G. M. 2005. Design for mixing using bubbles in branched microfluidic channels. *Applied Physics Letters* **86** (24), 86–88.
- Guermond, J. L. & Quartapelle, L. 1997. Calculation of incompressible viscous flows by an unconditionally stable projection fem. *Journal of Computational Physics* **132** (1), 12–33.
- JACQMIN, D. 1999. Calculation of two-phase navier-stokes flows using phase-field modeling. *Journal of Computational Physics* 155 (1), 96–127.
- LINK, D. R., ANNA, S. L., WEITZ, D. A. & STONE, H. A. 2004. Geometrically mediated breakup of drops in microfluidic devices. *Physical Review Letters* **92** (5), 054503-1–4.
- MANGA, M. 1996. Dynamics of drops in branched tubes. *Journal of Fluid Mechanics* **315**, 105–117.
- MENETRIER-DEREMBLE, L. & TABELING, P. 2006. Droplet breakup in microfluidic junctions of arbitrary angles. *Physical Review E* **74** (3), 035303-1–4.
- Pozrikidis, C. 2001. Interfacial dynamics for stokes flow. *Journal of Computational Physics* **169** (2), 250–301.
- Prakash, M. & Gershenfeld, N. 2007. Microfluidic bubble logic. *Science* 315 (5813), 832–835.
- RAYLEIGH, L., 1882. On the equilibrium of liquid conducting masses charged with electricity. *Philos. Mag.* **14** (184–186).
- Song, H., Tice, J. D. & Ismagilov, R. F. 2003. A microfluidic system for controlling reaction networks in time. *Angewandte Chemie–International Edition* 42 (7), 768–772.
- Taylor, G. I. 1934. The Formation of Emulsions in Definable Fields of Flow. *Royal Society of London Proceedings Series A* **146**, 501–523.
- Taylor, G. I. 1960. Deposition of a viscous fluid on the wall of a tube. *Journal of Fluid Mechanics* **10** (02), 161–165.
- VAN DER GRAAF, S., NISISAKO, T., SCHROEN, C. G. P. H., VAN DER SMAN, R. G. M. & BOOM, R. M. 2006. Lattice boltzmann simulations of droplet formation in a t-shaped microchannel. *Langmuir* **22** (9), 4144–4152.
- VAN DER WAALS, J. 1893. The thermodynamic theory of capillarity under the hypothesis of a continuous variation of density. J.D. Verhandel. Konink. Akad. Weten. 1 (J. Stat. Phys., 20, 1979 (in English)).
- VILLANUEVA, W. & Amberg, G. 2006. Some generic capillary-driven flows. *International Journal of Multiphase Flow* **32** (9), 1072–1086.

Paper 2

Modeling of dynamic wetting far from equilibrium

By Andreas Carlson, Minh Do-Quang and Gustav Amberg

Linné FLOW Centre, Department of Mechanics, The Royal Institute of Technology, 100 44 Stockholm, Sweden.

Physics of Fluids 21 (12), 121701-1-4, 2009.

In this paper we present simulations of dynamic wetting far from equilibrium based on phase field theory. In direct simulations of recent experiments [J. C. Bird, S. Mandre and H. A. Stone, *Physical Review Letters* **100** (23), 234501 (2008)], we show that in order to correctly capture the dynamics of rapid wetting, it is crucial to account for non-equilibrium at the contact line, where the gas, liquid and solid meet. A term in the boundary condition at the solid surface that naturally arises in the phase field theory is interpreted as, allowing for the establishment of a local structure in the immediate vicinity of the contact line. A direct qualitative and quantitative match with experimental data of spontaneously wetting liquid droplets is shown.

How a liquid spreads on a dry solid surface is an everyday experience, and an important part in numerous industrial applications. The actual physics that governs the phenomenon of moving contact lines, and the prediction of such processes in practice, still today remains unclear (Blake (2006), Ren & E (2007)). Part of the reason for the lack of definite and conclusive answers is that the resulting dynamics is dictated by physical phenomena taking place on different length scales. The large-scale dynamics are typically governed by hydrodynamic theory, while the movement of the contact line is determined by processes on or just above molecular length scales.

One reason that dynamic wetting has remained mysterious is that experiments are difficult, with a large span in length scales, and, in this context, very rapid timescales. The emergence of ultra fast cameras have made rapid dynamic wetting experimentally accessible. The spontaneous spreading of partially wetting liquid droplets on surfaces with different wettability were described in a recently published article by Bird et al. (2008). They were able to capture in detail the dynamic evolution of the contact line and the droplet shape, also during the very rapid first phase. It was shown that viscous scaling fails to describe the initial wetting behavior, as it was found to be driven by inertia. Rapid wetting has also been identified in molecular dynamics simulations by

Ren & E (2007) at the nano scale. They described this regime as the onset of non-linear response, and proposed that a molecular diffusive or active processes governs the contact line motion.

There exists two principal theories for the description of dynamic wetting phenomena, namely the molecular-kinetic theory and the hydrodynamic theory. Molecular-kinetic theory describes dynamic wetting as the disturbance of adsorption equilibria at the contact line, where the three phases meet. Its movement is explained by statistical dynamics of the molecular motion in the vicinity of the contact line. Within this zone the molecules have a characteristic rate constant (k_0) and length (λ) of random displacements (Blake (2006)).

In hydrodynamic theories, built on a continuum description, the classical no-slip condition of zero fluid velocity at a solid surface leads to an essential singularity in stress (Huh & Scriven (1971)). Nonetheless, dynamic wetting models have been developed for the region near the contact point (Voinov (1976)). These models allow for local slip near the contact line, and consider the formation of the dynamic contact angle as an outcome of the viscous bending force acting on the free surface. It is notable that both the molecular-kinetic and hydrodynamic theory have been applied with success, pointing out that both models captures different key aspects of the phenomenon.

Another way to handle moving contact lines without violating the no-slip condition is the phase field theory (Jacqmin (2000)), which enables contact line motion by diffusive interfacial fluxes. Its theoretical framework stems from a thermodynamic formulation (Cahn & Hilliard (1958)), based on a description of the free energy in the system. In what follows we will use this formulation in order to study the very rapid wetting observed by Bird $et\ al.\ (2008)$. We will show that in order to capture the observed behavior it is necessary to allow for non-equilibrium in the contact line condition. The parameters in the model are, apart from the properties of the fluids and the surface energies, the interface width (ϵ) and a mobility (D_w^*) associated with the contact line. The value of this mobility is estimated from comparisons between simulations and experiments by Bird $et\ al.\ (2008)$. Its interpretation and physical significance is discussed.

The governing Cahn-Hilliard Navier Stokes equations for incompressible flow of a binary system Jacqmin (2000), are given in eq. 1, 2, 4:

$$\nabla \cdot \mathbf{u} = 0,\tag{1}$$

$$\rho(C)\frac{D\mathbf{u}}{Dt} = -\frac{1}{Re}\nabla P + \frac{1}{Re}\nabla \cdot \tau - \frac{Bo}{We}\mathbf{e}_z - \frac{C\nabla\phi}{We\cdot Cn}.$$
 (2)

These equations have been made non-dimensional with the material properties of the liquid phase (subscript l), the capillary speed $U = \frac{\sigma}{\mu_l}$ and the characteristic length L, giving the dimensional velocity $\mathbf{u}^* = U \cdot \mathbf{u}$ and pressure $P^* = \frac{\mu_l U}{L} P$. μ_l is the liquid viscosity and σ is the surface tension coefficient. $\tau = \mu(C)(\nabla \mathbf{u} + (\nabla \mathbf{u})^T)$ is the Newtonian viscous stress tensor. C denotes the continuous phase field variable, which takes the value -1 in the gas and 1

in the liquid. The density $\rho(C)$ and the viscosity $\mu(C)$ depend on C according to $\rho(C)=\frac{1}{2}(C+1)-\frac{\rho_g}{2\rho_l}(C-1)$, and $\mu(C)=\frac{1}{2}(C+1)-\frac{\mu_g}{2\mu_l}(C-1)$, where subscript g denotes gas phase. The Reynolds (Re) number $Re=\frac{\rho_l U L}{\mu_l}$ describes the relative importance between the inertial and viscous force in the flow. The Bond (Bo) number expresses the ratio between the buoyancy and the surface tension force $Bo=\frac{(\rho_l-\rho_g)gL^2}{\sigma}$. g is gravity and \mathbf{e}_z is the unit vector in z-direction. The Weber (We) number expresses the ratio between the inertia and surface tension force, $We=\frac{2\sqrt{2}\rho_l L U^2}{3\sigma}$. The term $C\nabla\phi$ is modeling the surface tension force (Jacqmin (2000)) where ϕ is the chemical potential. The Cahn number (C_n) is expressing the ratio between the interface width (ϵ) and the characteristic length scale, $C_n=\frac{\epsilon}{L}$.

The phase field theory is based on a description of the free energy in the system, here postulated as in Jacqmin (2000),

$$F = \int_{\Omega} \left(\beta \Psi(C) + \frac{\alpha}{2} |\nabla C|^2 \right) d\Omega + \int_{\Gamma} \left(\sigma_{sl} + \Delta \sigma \right) d\Gamma.$$
 (3)

The volume integral (Ω) represents the bulk free energy and the surface integral (Γ) the free energy contribution from the surface. Here, $\Psi = \frac{1}{4}(C+1)^2(C-1)^2$ is a double-well function with two stable minima that expresses the two equilibrium concentrations for gas $(C_g = -1)$ and liquid $(C_l = 1)$. α and β are phase field parameters proportional to; $\alpha \sim \sigma \epsilon$, $\beta \sim \frac{\sigma}{\epsilon}$. $\Delta \sigma = (\sigma_{sg} - \sigma_{sl})w(C)$ where σ_{sg} and σ_{sl} are the surface energies for the solid-gas (sg) and solid-liquid (sl) interfaces, and $w(C) = 0.5 - 0.75C + 0.25C^3$ is a normalized function varying smoothly from 0 to 1. Based on the free energy formulation the Cahn-Hilliard equation can be derived in a standard way, that determines the phase field variable C, omitting here the surface contribution:

$$\frac{DC}{Dt} = \frac{1}{Pe} \nabla^2 \phi = \frac{1}{Pe} \nabla^2 \left(\Psi'(C) - C_n^2 \nabla^2 C \right). \tag{4}$$

Here Pe is the Peclet number, expressing the ratio between advection and diffusion, $Pe = \frac{UL}{D}$, where D is the bulk diffusivity (Villanueva & Amberg (2006)). The chemical potential ϕ^* is non-dimensionalized as $\phi^* = \phi \beta$ and defined as the variation in free energy with respect to $C \phi^* = \frac{\delta F}{\delta C}$, which results in the second equality in eq. 4.

Following the methods of phase field theory the boundary condition for C on a solid surface is derived by collecting all boundary terms in the variation of the free energy (F) with respect to C,

$$\delta_{\Gamma} F = \int_{\Gamma} \left(\sigma \epsilon \nabla C \cdot \mathbf{n} + (\sigma_{sg} - \sigma_{sl}) w'(c) \right) \delta C d\Gamma$$
 (5)

where \mathbf{n} is the surface normal. Here the first term on the right hand side arises from the gradient energy term in the bulk.

In keeping with the strategy of phenomenological non-equilibrium thermodynamics, we now require the evolution of C to be such that further changes

 $\delta C \sim \frac{\partial C}{\partial t}$ are associated with a decrease in free energy. This leads to a general form of the boundary condition for C, see Jacquin (2000),

$$D_w^* \frac{\partial C}{\partial t} = \sigma \epsilon \nabla C \cdot \mathbf{n} + (\sigma_{sg} - \sigma_{sl}) w'(C)$$
 (6)

where D_w^* is a phenomenological parameter.

This boundary condition accounts for non-equilibrium and has previously been discussed by Jacqmin (2000). Qian et al. (2003) obtained a direct match between phase field and molecular dynamics simulations of moving contact lines at the molecular scale. This was achieved by extracting the phase field parameters and the local slip at the surface from the MD simulations, that was used as input in the phase field model, using a similar boundary condition as the one above. It should be noted that these wetting simulations does not lie within the rapid regime, studied here. To our knowledge, the boundary condition given in eq. 6 has never been explored in practical simulations, as the contribution from its left hand side has been neglected. Such an assumption applies for small D_w^* , leading to the immediate enforcement of the equilibrium contact angle as the liquid wets the solid. This has been a common and generally successful assumption in phase field simulations of wetting phenomena (Jacqmin (2000), Villanueva & Amberg (2006), Do-Quang & Amberg (2009), Khatavkar et al. (2007)). In some of these simulations fast interfacial dynamics takes place, but the contact angle close to the surface does not deviate significantly from the static equilibrium value. However, we will show below that in very rapid wetting situations, such as observed in Bird et al. (2008), this is inadequate, but by retaining the time derivative in eq. 6 the appropriate non-equilibrium effects are captured.

We interpret D_w^* as a phenomenological parameter that stems from the molecular interaction at the contact line and propose a definition of D_w^* , based on parameters from the molecular-kinetic theory. The molecules have a thermal energy (k_BT) and move over a length (λ) . The molecular movement is associated with the rate constant of random displacement (k_0) as they interchange adsorption sites at the solid surface, forming new contact line. This is analogous to the temporal breaking of wall-liquid bonds and implies that the dynamic contact angle is caused by molecular diffusion, in a dissipative process, as the molecules reorganize near the contact line. D_w^* is defined accordingly, $D_w^* = \frac{k_B T}{\lambda^2 k_0}$. The factor $\frac{k_B T}{\lambda^2} = \sigma_M$ corresponds to the surface energy needed for the molecules to make an interchange in adsorption sites and $k_0\lambda = U_M$ is the molecular mean velocity caused by adsorption site hopping. This leads to the dimensionless non-equilibrium wetting boundary condition,

$$D_w \frac{\partial C}{\partial t} = C_n \nabla C \cdot \mathbf{n} + \cos(\theta_e) w'(C) \tag{7}$$

where $\cos(\theta_e) = \frac{\sigma_{sg} - \sigma_{sl}}{\sigma}$. θ_e is the static equilibrium contact angle and D_w is defined as $D_w = \frac{D_w^*}{\mu_l L} = \frac{Kn}{Ag}$. We have chosen to express the coefficient multiplying $\frac{\partial C}{\partial t}$ in terms of two additional non-dimensional numbers; $Ag = \frac{\mu_l U_M}{\sigma_M}$ is

a new dimensionless number expressing the ratio between the work done by the viscous force and the energy needed for a molecular site interchange. $Kn=\frac{\lambda}{L}$ is similar to a Knudsen number denoting the ratio between the typical molecular displacement and the characteristic macroscopic length. Based on the present derivation we recognize that the term that accounts for the relaxation towards equilibrium becomes less significant for highly viscous fluids and large scale wetting.

In order to estimate the magnitude of the parameter D_w^* we introduce values that are commonly reported in the literature from the molecular-kinetic theory (Blake (2006)) for $\lambda=0.5nm$, $k_0=10^6s^{-1}$ and apply $k_B=1.23\cdot 10^{-23}JK^{-1}$, T=300K. It should be noted that these material constants vary for different liquids and solids. By applying these values we obtain $D_w^*=1.5\cdot 10^{-8}Nsm^{-1}$. We also note that the energy required for the interchange of adsorption site/breaking solid-liquid bonds $\sigma_M=0.015Nm^{-1}$, with $Kn=6.4\cdot 10^{-7}$ and $Ag=3.3\cdot 10^{-5}$, giving $(D_w)_{m-k}=0.019$ where the subscript (m-k) denotes molecular kinetic. Jacqmin (2000) gave a rough estimate of the magnitude of D_w^* based on data from molecular dynamics simulations. His result is $(D_w^*)_J \sim 10^{-9}Nsm^{-1}$, in reasonable accordance with our prediction.

To summarize the model formulation, the equations (1, 2, 4, 7) now include the properties of the liquid and the gas, i.e. densities, viscosities and surface energies for the three interfaces that appear, and the bulk mass diffusion coefficient. The only additional parameters in the model are the interface width ϵ , and the rate coefficient D_w^* in eq. 6. The interface width and bulk diffusivity were seen, in additional simulations not presented here, to have a limited influence on the results. Thus we keep $Pe = 10^4$ and $Cn = 10^{-2}$ constant in all simulations. D_w^* , as discussed above, we believe is an independently measurable quantity that characterizes rapid wetting. The model in itself has no adjustable parameters, even though at the present time we could only obtain the order of magnitude for D_w^* from independent data.

A water droplet ($\rho_l = 998kg/m^3, \mu_l = 10^{-3}Pa \cdot s$) with a radius of L=0.78mm in air ($\rho_g = 1.2kg/m^3, \mu_g = 1.6 \cdot 10^{-5}Pa \cdot s$) with the surface tension $\sigma = 72.7mN/m$ is modeled as it spontaneously wets three dry surfaces with different wettability ($\theta_e = [3, 43, 117]^{\circ}$). These material parameters have been kept constant in all simulations. The simulation setup is in accordance with the experiments performed by Bird et al. (2008). Initially a spherical droplet is pinned at the upper wall mimicking the needle used in the experiments see fig. 2, with an equilibrium contact angle of $\theta_e = 90^{\circ}$, and it wets the lower solid surface by diffusion. Axi-symmetric simulations have been performed with the Finite Element code FemLego (Do-Quang & Amberg (2009)), a symbolic tool for solving partial differential equations, and the equations have been solved in accordance with Villanueva & Amberg (2006). An equidistant base mesh has been applied with ~ 40 elements over the initial droplet radius and an adaptive mesh refinement method (Villanueva & Amberg (2006)) has

been used, enabling a high resolution of the interface here being 6.5 times finer than the base mesh.

Fig. 1 shows the temporal evolution of the droplet spreading radius (r). Our results reveals that the assumption of local equilibrium $D_w = 0$ fails, as the contact lines travel too fast. A set of simulations were performed where we only vary D_w to obtain its correct value, since the physical properties for λ and k_0 are, to our knowledge, not accessible for these different solid-liquid-gas systems. From a physical perspective D_w should differ in different systems. Fig. 1 shows the best fit and a direct match with the experimental results on three surfaces with equilibrium contact angles equal to $\theta_e = [3^{\circ}, 43^{\circ}, 117^{\circ}]$ corresponding to $D_w = [0.05, 0.07, 0.01]$. It still remains unclear why D_w is behaving non-monotonically with regard to the equilibrium contact angle. Note that the numerical predicted values for D_w are in agreement with the order of magnitude analysis given above, based on the data from the molecular kinetic theory $(D_w)_{m-k} = 0.019$. These results indicate that dynamic wetting is driven by the relaxation towards thermodynamic equilibrium, by minimizing the free energy. In order to correctly capture the wetting speed, and recreate the wetting physics, it is crucial to account for non-equilibrium effects.

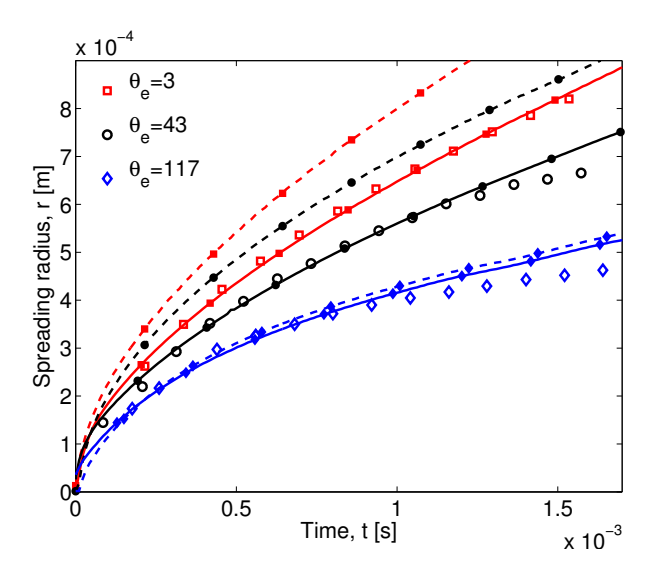


Figure 1: Temporal contact line evolution; square, round and diamond shaped markers denote results for $\theta_e = [3^{\circ}, 43^{\circ}, 117^{\circ}]$. Full lines corresponding to $D_w = [0.05, 0.07, 0.01]$ and dashed lines to $D_w = 0$. The experimental results from Bird *et al.* (2008) are given by the large open symbols.

The behavior at very early times is most likely dominated by the rupture of a film, or incipience of wetting, similar to a nucleation event. The simulations are not intended to capture this accurately, note in fig. 1 that we have little

data at times less than 0.1 ms. Late time spreading dynamics disclose that the simulations even capture the change of slope for the radius observed between the dimensionless time 2 and 3 see Fig. 3 in reference Bird et al. (2008). The shift in power-law spreading is believed to be a contraction of the droplet after detaching from the wall due to an overshoot in contact angle, rather than a transition from inertial to a viscously dominated spreading as hypothesized by Bird et al. (2008). This kink was observed with both wetting boundary conditions. Space does not allow us to report this in detail here, but this will be presented elsewhere.

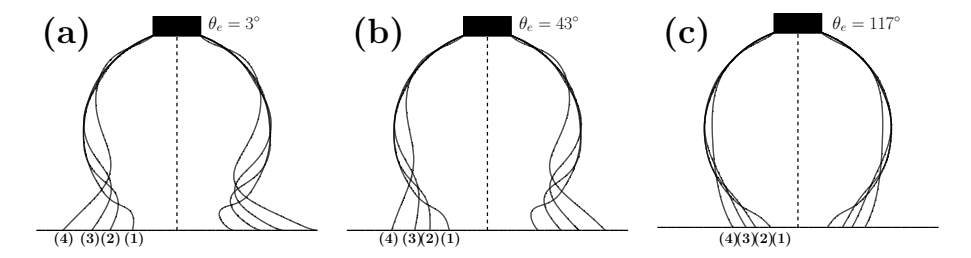


Figure 2: Droplet shapes at (1) t=0.4ms, (2) t=0.8ms, (3) t=1.2ms and (4) t=1.9ms, for three different surfaces: a) $D_w=0.05, \ \theta_e=3^\circ$, b) $D_w=0.07, \ \theta_e=43^\circ$, c) $D_w=0.01, \ \theta_e=117^\circ$. The right half of each panel shows the corresponding simulated result for equilibrium conditions, $D_w=0.01$.

Fig. 2 shows four snapshots of the droplet as it spontaneously wets dry surfaces, for three different wettabilities. The left half of each panel in fig. 2 displays the results with a non-equilibrium wetting boundary condition and the right side displays the results with the assumption of wetting at local equilibrium $(D_w = 0)$. At time (1) the droplet has just come in contact with the solid surface, and it wets the surface in the successive times (2,3 and 4). The results with the dynamic wetting model (left) shows that the droplet initially forms a large contact angle $\sim 150^{\circ}$ as it wets the surface. As the droplet spreads, the dynamic contact angle relaxes towards its equilibrium value θ_e . One clear observation is that the dynamic contact angle differs substantially from the static equilibrium value θ_e . The results with the assumption of local equilibrium (right half) show that, as the liquid wets the solid at time (1), a local equilibrium contact angle is immediately enforced. As the contact line propagates in time (2,3,4) the contact angle remains nearly constant. Notice in particular that the wetting line for the non-equilibrium condition propagates slower than with the equilibrium treatment. This is due to the additional energy dissipation at the contact line, as it relaxes towards equilibrium. A significant difference is found for the droplet shapes for the two different treatments in the partial wetting regime fig. 2a, b.

Comparison of the droplet shapes in fig. 2 and the experimental results of spontaneously wetting droplets (Bird et~al.~(2008); Drelich & Chibowska (2005)) shows that the equilibrium assumption is deficient. It overpredicts the capillary wave in all three cases. The dynamic wetting treatment on the other hand produces wetting characteristics in striking similarity with the experimental results in Bird et~al.~(2008); Drelich & Chibowska (2005). Note in particular that the droplets in fig. 2, with a radius L=0.78mm for the times t (1,2,3), are in direct correspondence with the temporal evolution given in reference Bird et~al.~(2008)-Fig. 1 for a droplet with a radius L=0.81mm.

In summary we have shown that with a wetting boundary condition that accounts for non-equilibrium at the contact line, the phase field formulation, built on the primary thermodynamical properties of the system, correctly captures dynamic wetting phenomena of spontaneously spreading liquid droplets. The presented model has one additional, physically reasonable, and in principle measurable parameter (D_w^*) . We propose a definition of this term as $D_w^* = \frac{k_B T}{\lambda^2 k_0}$, based on parameters from the molecular kinetics theory. In this context, the model encompasses both the hydrodynamic and the molecular kinetic theories. A direct qualitative and quantitative match is obtained with experimental results on the droplet-spreading rate and shape, respectively. The results indicate that contact line motion and the dynamic contact angle formation are due to molecular interactions at the vicinity of the contact line. In the partial wetting regime, the simulations did not show much viscous bending, and the dissipation of energy at the contact line is believed to be related to a diffusive reorganization of molecules at the contact line, rather than viscous dissipation.

References

- BIRD, J. C., MANDRE, S. & STONE, H. A. 2008 Short-time dynamics of partial wetting. Physical Review Letters, 100(23), 234501-1-4.
- Blake. T. D. 2006 The physics of moving wetting lines. *Journal of Colloid and Interface Science*, **299**, 1–13.
- CAHN, J. W. & HILLIARD, J. E. 1958 Free energy of a nonuniform system. i. interfacial free energy. The Journal of Chemical Physics, 28 (2), 258–267.
- Do-Quang, M. & Amberg, G. 2009 The splash of a solid sphere impacting on a liquid surface: Numerical simulation of the influence of wetting. *Physics of Fluids*, 21 (2), 022102.
- Drelich, J. & Chibowska, D. 2005 Spreading kinetics of water drops on self-assembled monolayers of thiols: Significance of inertial effects. *Langmuir*, **21**(17):7733–7738.
- Huh, C. & Scriven, L. E. 1971 Hydrodynamic model of steady movement of a solid/liquid/fluid contact line. *Journal of Colloid and Interface Science*, **35** (1), 85–101.

- JACQMIN, D. 2000 Contact-line dynamics of a diffuse fluid interface. Journal of Fluid Mechanics, 402, 57–88.
- Khatavkar, V. V., Anderson, P. D., Duineveld, P. C. & Meijer, H. E. H. Diffuse-interface modelling of droplet impact. *Journal of Fluid Mechanics*, **581**:97–127, 2007.
- QIAN, T. Z., WANG, X. P. & SHENG, P. Molecular scale contact line hydrodynamics of immiscible flows. *Physical Review E*, **68** (1).
- REN, W. & E. W. 2007 Boundary conditions for the moving contact line problem. *Physics of Fluids*, **19** (2), 022101-1–15.
- O. V. Voinov. 1976 Hydrodynamics of wetting. Izvestiya Akademii Nauk SSSP, Makhanika Zhidkosti i Gaza, 5 (76–84).
- VILLANUEVA, W. & AMBERG, G. 2006 Some generic capillary-driven flows. *International Journal of Multiphase Flow*, **32**(9), 1072–1086.

Paper 3

Dissipation in rapid dynamic wetting

By Andreas Carlson, Minh Do-Quang and Gustav Amberg

Linné FLOW Centre, Department of Mechanics, The Royal Institute of Technology, 100 44 Stockholm, Sweden.

Journal of Fluid Mechanics 682, 213–240, 2011.

In this article we present a modeling approach for rapid dynamic wetting based on the phase field theory. We show that in order to model this accurately it is important to allow for a non-equilibrium wetting boundary condition. Using a condition of this type, we obtain a direct match with experimental results reported in the literature for rapid spreading of liquid droplets on dry surfaces. By extracting the dissipation of energy and the rate of change of kinetic energy in the flow simulation, we identify a new wetting regime during the rapid phase of the spreading. This is characterized by the main dissipation to be due to a reorganization of molecules at the contact line, in a diffusive or active process. This regime serves as an addition to the other wetting regimes that have previously been reported in the literature.

1. Introduction

Contact lines between solids and liquid or gas interfaces appear in very many instances of fluid flows. This could be coffee stains, water-oil mixtures in oil recovery, hydrophobic feet of insects or surfaces of leaves in nature. Due to their ubiquitous occurrence in nature and our daily life, as well as in industrial processes, they have attracted the attention of researchers since many years. What kind of physical mechanisms that actually govern dynamic wetting phenomena have been a matter of controversy and argument in the recent literature (Eggers & Evans (2004) Blake & Shikhmurzaev (2002), Shikhmurzaev & Blake (2004)), where these viewpoints have been based on different theoretical approaches (Blake (2006), Bonn et al. (2009)). Even though extensive research has been directed towards wetting physics, many phenomena with moving contact lines are still not well understood. An example of such is the understanding of the physical processes that govern rapid dynamic wetting, which still holds challenges.

Despite the apparent simplicity of placing a small water droplet on a glass plate, the prediction of its evolution after contact with the solid surface is non-trivial. A number of physical phenomena in the bulk and at the solid surface influence the evolution of the spreading droplet. This is particularly true during

the initial phase of wetting, when the contact line speed is typically the greatest. In this case, experimental investigations show (Bird *et al.* (2008), Biance *et al.* (2004), Drelich & Chibowska (2005)) that the initial speed of the contact line of water on a hydrophilic surface is in the order of meters per second.

General reviews of wetting phenomena are given by de Gennes (1985), Blake (2006) and Bonn *et al.* (2009). In the following we will discuss literature particularly relevant for the very rapid wetting processes that are the subject of this paper.

The contact line is formed as the interface between a gas and a liquid, or two immiscible liquids, interacts with a solid substrate. A classical problem in fluid dynamics has been that the Stokes equations allow a solution for the flow in the vicinity of the contact line, which however exhibits a non-integrable singularity of the viscous stress at the wall, Huh & Scriven (1971). This singularity can be removed formally if the no-slip condition at the wall is relaxed. The root of the problem is however that the continuum description breaks down and that phenomena at molecular length scales must somehow be accounted for. Allowing slip on the wall and using Navier Stokes equations, Voinov (1976) and Tanner (1979) derived a relationship between the apparent or observable contact angle and the Capillary number (Ca) (Blake (2006)),

$$\theta_D^3 - \theta_m^3 = 9Ca \ln(\frac{h}{h_m}). \tag{1}$$

Here θ_D is the apparent contact angle, i.e. the angle between the macroscopically observable interface and the solid wall. θ_m is the microscopic contact angle at the solid surface, which is usually assumed to be the equilibrium contact angle. Ca is the Capillary number, $Ca = \mu U/\sigma$, giving the ratio between the viscous and surface tension force. μ is the droplet viscosity, U the wetting speed and σ is the surface tension coefficient.

The equation is derived based on the assumption that $\theta_D < 3/4\pi$ and that the characteristic length h, e.g. droplet diameter, is much larger than the microscopic length h_m , $h \gg h_m$. The singularity at the solid surface is here circumvented by introducing the slip-length, an ad-hoc length of microscopic size h_m . It is commonly determined (h_m) by curve fitting of the equation to experimental results. A similar result to Voinov (1976) and Tanner (1979) was obtained by Cox (1986), based on an asymptotic reduction of the Navier Stokes equations. These results generally match available experimental data well, such as the experiments from Hoffman (1975). In the hydrodynamic theory, the surface tension force generated by the local curvature near the contact line is believed to be the driving mechanics behind contact line motion, whereas viscosity in the bulk is resisting its motion.

Another physical explanation of contact line motion was proposed by Blake & Haynes (1969), a theory that is often referred to as the molecular kinetics (MK) theory. Contact line movement is here considered to be an active process at the molecular adsorption sites on the solid surface. The molecules are

assumed to hop back and forth between adsorption sites with a characteristic frequency (k_0) , where they move over a molecular distance (λ) . Based on Eyring's theory of absolute reaction rates (Glasstone *et al.* (1941)) the frequency of molecular transfer due to the forward (K^+) and backward (K^-) hopping can be expressed as (Ren & E (2007)),

$$K^{+} = k_0 \exp(\frac{w}{2nk_bT}), \ K^{-} = k_0 \exp(\frac{-w}{2nk_bT})$$
 (2)

where n the number of adsorption sites per unit area, k_b the Boltzmann constant and T the temperature. $w = \sigma(\cos(\theta_0) - \cos(\theta))$ is the work done due to the uncompensated Young's stress by having a non-equilibrium contact angle, where θ_0 is the equilibrium contact angle and θ is the dynamic contact angle. This gives the relationship for the velocity of the moving contact line as,

$$V_{MK} = \lambda (K^+ - K^-) = 2k_0 \lambda \sinh\left(\frac{\sigma(\cos(\theta_0) - \cos(\theta))}{2nk_b T}\right). \tag{3}$$

At equilibrium the backward and forward hopping are equal as are the dynamic and equilibrium contact angle, predicting no contact line motion.

Despite the fact that these two theories are formulated on different length scales and from very different points of view, they have both been applied with success. This suggests that the hydrodynamic and molecular kinetic theory each captures different wetting physics. It should be noted that no active molecular processes are accounted for in the hydrodynamic theory and that the MK theory does not include any influence from viscosity. A combined model was proposed by Petrov & Petrov (1992) that merge these two approaches, in an attempt to capture a broader spectrum of wetting phenomena.

Experimental investigations of droplet spreading have historically been mainly focused on the rather slow viscously dominated spreading regime, such as the work by Hoffman (1975) and Ngan & Dussan V. (1982) to name a few. These experiments have been well explained by already existing theoretical models, such as the one by Voinov-Tanner. Experiments have earlier been limited in both temporal and spatial resolution, making certain rapid wetting phenomena inaccessible. An example of such is the short-time spreading of a water droplet on a glass surface. The advent of high-speed cameras has now made such wetting phenomena experimentally accessible, and in recent years experimental results have appeared (Bird et al. (2008), Biance et al. (2004), Drelich & Chibowska (2005), Saiz & Tomsia (2004)). The observations have many similarities, such as the temporal evolution of the droplet shape, where the observable contact angle highly differs from the equilibrium value as the droplets spreads. In these rapid spreading experiments, the contact line moves with a characteristic velocity in the order of meters per second.

Bird et al. (2008) captured in detail, with a high-speed camera (67000fps), the temporal contact line evolution for droplets spreading on solid surfaces with varying wettability. In these experiments, also the initial rapid wetting phase was captured. By varying the droplet size, viscosity and surface wettability

they showed that the time scale for the phenomena failed to follow a viscous scaling. A striking finding was made, as the experiments fell on a master curve based on an inertial time scale. This indicates that inertia might resist wetting. They also found that the slope of the spreading rate depended on the equilibrium contact angle of the surface. Additional spreading data was provided in Courbin *et al.* (2009), in an attempt to expand the collapse with a viscous scaling. It was also shown that the spreading power law response depended on the initial shape of the droplets.

Ren & E (2007) identified a similar rapid wetting regime, at the nano scale, in molecular dynamics simulation. They described this flow regime as the onset of non-linearity, due to the large local forcing acting in the contact line region. This flow was suggested to be an active or diffusive process, at the contact line. It was pointed out that this type of wetting physics still remains unclear, and further investigations are needed to identify the governing wetting mechanisms.

An alternative way to obtain models of wetting phenomena is through the use of phase field theory, which is based on a phenomenological description of the free energy of the system. The phase field framework enables contact line motion due to diffusive interfacial fluxes, in other words, a different mechanism from those mentioned above. For relatively slow wetting phenomena, situated in the same wetting regime as Voinov-Tanners theory and Hoffmann's experiments, the phase field theory has proven both analytically (Jacqmin (2000)) as well as numerically (Villanueva & Amberg (2006), Yue et al. (2010) and Briant & Yeomans (2004)) to capture such wetting physics. Briant & Yeomans (2004) found the contact line diffusion to vary over a length scale different than the interface width, and by scaling arguments showed that this length is related to the mobility constant multiplying the chemical potential. Yue et al. (2010) made a modification to the scaling of the diffusion length and interpreted the microscopic length in Voinov-Tanners theory (h_m) in terms of the contact line diffusion length from the phase field theory. It should be noted that all of these results are obtained by making the physical assumption that the interface is close to an equilibrium state as it wets the solid.

The equilibrium boundary condition, mentioned above, has been expanded to a general boundary condition by Qian et~al.~(2006a), which has been explained by Onsager's principles of minimum dissipation (Qian et~al.~(2006b)). By extracting the phase field parameters and local slip at the surface from molecular dynamics simulations, used as input parameters in the phase field model, a direct match of the interface and slip profile could be obtained at the nano scale, see Qian et~al.~(2006b), Qian et~al.~(2004). An important point, is that these simulations fall in the same category as the results from Villanueva & Amberg (2006), Yue et~al.~(2010) as they are in this context considered to have rather slow wetting dynamics.

In our recent paper Carlson et al. (2009) we showed that the assumption of local equilibrium at the solid surface is deficient in the rapid dynamic

wetting regime, and that the phase field, or diffuse interface, framework, provides a rather natural way to incorporate non-equilibrium effects at the contact line. This implies that there is an important relaxation process from a nonequilibrium towards an equilibrium state. Within the phase field framework the boundary condition that accounts for such wetting physics, follows directly from the variational formulation of the free energy in the system, see Jacquin (2000). We showed (Carlson et al. (2009)) that by including the effects of nonequilibrium in the boundary condition at the solid surface, a direct match could be obtained with the detailed experimental results by Bird et al. (2008). In the contact line formulation at the solid surface a rate coefficient D_W appears, which was interpreted in terms of parameters from the MK theory. Jacquin (2000) was to our knowledge the first to discuss this boundary condition and he made a rough estimate of the magnitude of D_W , based on molecular dynamics simulation data from Matsumoto et al. (1995). The magnitude of the coefficient found by Carlson et al. (2009) and Jacquin (2000) are in reasonable agreement. Thus, it is believed that this general wetting formulation encompasses wetting regimes that have previously been captured with the hydrodynamic and the MK theory.

Four different regimes have been presented in the literature, which are said to describe the force balances and dissipation mechanisms in dynamic wetting, at different stages. These are the initial cusp, inertia and viscous wetting from the hydrodynamic theory and molecular contact line friction from the molecular kinetic theory. In the very first short-time spreading, the interface forms a small cusp region where viscosity is believed to dominate the spreading dynamics (Eggers $et\ al.\ (1999)$, Biance $et\ al.\ (2004)$). This initial spreading regime takes place as the droplet starts to spread onto the solid, where a small region with a high curvature drives the flow. As the length scales are small the flow has a low Reynolds number (Re), describing the relative importance between inertia and viscous forces, and viscosity is impeding the contact line motion that is driven by interfacial energy.

As the contact line propagates across the solid surface the spreading radius increases and the liquid in the bulk of the droplet is accelerated, consequently increasing the inertial forces in the flow. When sufficient bulk liquid is accelerated, inertia is dominating over the initial viscous dissipation and constitutes the main hindrance for droplet spreading. The inertial spreading was found to obey the laws predicted by Eggers et al. (1999), also found experimentally by Aarts et al. (2005). By following the same reasoning as Eggers Biance et al. (2004), Aarts et al. (2005) found the spreading radius for inertial wetting to also scale with the square root of time. Geometrical arguments about the flow, forced by symmetry in the direction perpendicular to contact and that both seemingly are driven by gradients in curvature provides an analogy between droplet coalescence and spreading. Nonetheless, droplet spreading can not be fully explained by gradients in curvature since the solids equilibrium

contact angle is experimentally found to influence the power-law response to the spreading curve (Bird *et al.* (2008)).

In the late time dynamics, the droplet has a slow, nearly steady motion as it relaxes towards its equilibrium contact angle. This slow wetting dynamics is often characterized by the capillary number Ca, and viscous dissipation in the whole bulk is the main source for the resistance to contact line motion. The slow viscously dominated wetting has been well defined by classical wetting relations as derived by Voinov (1976), Tanner (1979), Cox (1986)). By assuming that the droplet has a spherical cap and applying Tanners law (Biance $et\ al.\ (2004)$) the relationship between the spreading radius (r) and time (t) can be derived, and scales with $r \sim t^{\frac{1}{10}}$. The expressions for the inertial and viscous spreading radii then yield a criterion for the transition between inertial and viscous wetting, as described by Biance $et\ al.\ (2004)$.

The molecular kinetic theory describes a different dissipative mechanism than what is predicted with the hydrodynamic theory. Here, the dissipation arises from the advancing contact line region due to the attachment of liquid molecules at the solid surface (De Coninck et al. (2001)). The spreading radius in this regime is found to scale with $r \sim t^{\frac{1}{7}}$ and has been identified at later time scales, taking place after the inertial spreading regime described above (Seveno et al. (2009), De Coninck et al. (2001)).

Recent experimental findings suggest that at even shorter time spreading none of the regimes discussed above are appropriate, one indication being that the equilibrium contact angle seems to be a less important parameter here (Bird et al. (2008)). Two questions that remain are; if there exist additional dissipative mechanisms that might influence the spreading dynamics at very short times; and at what time scales do they govern the contact line motion?

The main purpose of the present paper is to present a mathematical model of very rapid spreading and, guided by results from this, elucidate the physics governing a rapid dynamic wetting process. In the next section the mathematical model is motivated and presented, including a new rate coefficient (D_W) , which we will argue captures molecular interactions at the contact line. In section 3 we present detailed simulations of recent experiments on rapidly spreading droplets. In section 4 we wish to identify the primary cause for resistance to spreading, by computing the evolution of the kinetic energy in the flow, as well as dissipation due to viscous stresses, and molecular processes at the contact line, etc. The relative magnitude of these is studied as the droplet evolves. We finally make some concluding remarks.

2. Phase field theory

The phase field, or diffuse interface, model is formulated here for a binary mixture of two immiscible fluids (gas or liquid), and includes the surface energies of fluid-fluid and fluid-solid interfaces. The formulation starts from a postulated free energy F of the system, as a functional of the fluid mixture composition

C,

$$F = \int_{\Omega} \left(\beta \Psi(C) + \frac{\alpha}{2} |\nabla C|^2 \right) d\Omega + \int_{\Gamma} \left(g(C)(\sigma_{sg} - \sigma_{sl}) + \sigma_{sl} \right) d\Gamma. \tag{4}$$

The free energy has one contribution from the bulk (Ω) and one from the bounding solid surfaces (Γ) . The first term in the integral over the volume Ω is the bulk potential, which is chosen here in the conventional way as $\Psi=\frac{1}{4}(C+1)^2(C-1)^2$. This function has two local minima which implies that the only stable equilibrium values that C can take are +1 or -1. These values thus denote regions occupied by one of the two pure fluids in the mixture. In what follows we will consider water and air, with C=1 for water and C=-1 for air. The second term in the bulk integral introduces the surface energy of fluid-fluid interfaces. The competition between the bulk and interfacial energy forms an interface, separating the two phases. β and α are phase field parameters, originating from the multivariable Taylor expansion about the free energy per molecule, see Cahn & Hilliard (1958). These determine the surface energy σ and the width of fluid-fluid interfaces ϵ according to $\beta=\frac{3\sigma}{2\sqrt{2}\epsilon}$ and $\alpha=\sigma\epsilon\frac{3}{2\sqrt{2}}$, or conversely $\sigma=\frac{2\sqrt{2}}{3}\sqrt{\alpha\beta}$ and $\epsilon=\sqrt{\frac{\alpha}{\beta}}$.

The free energy at the solid surface (Jacqmin (1999)), is formulated as an integral over the solid boundary Γ of the local surface energy. The function $g(C) = 0.5 - 0.75C + 0.25C^3$ is a smoothly varying function which is equal to 0 for a wet wall (C=1) and 1 for a dry wall (C=-1). It thus acts as a switch that changes the surface energy between σ_{sg} for a dry and σ_{sl} for a wet solid surface. The choice of the function g(C) is made so that, together with the choice of the double well function $\Psi(C)$, it will give an equilibrium contact angle consistent with Youngs law.

By taking the variational derivative of the free energy (F) with respect to the order parameter C and integration by parts we obtain:

$$\delta F = \int \left(\beta \Psi'(C) - \alpha \nabla^2 C \right) \delta C d\Omega + \int \left(\alpha \nabla C \cdot \mathbf{n} + g'(C) [\sigma_{sg} - \sigma_{sl}] \right) \delta C d\Gamma.$$
(5)

The integrand of the volume integral defines the bulk chemical potential $\phi^* = \beta \Psi'(C) - \alpha \nabla^2 C$. The surface integral defines the boundary condition for the chemical potential, accounting for the variation in free energy at the surface. The surface integral is representing the wetting boundary condition where \mathbf{n} is the surface normal. This boundary condition will be analyzed further below. By minimizing both the bulk contribution of the chemical potential with respect to the order parameter C the equilibrium profile for a flat interface can be obtained as $C_0(x) = \tanh(\frac{1}{\sqrt{2}\epsilon}x)$. The expression for surface energy $\sigma = \frac{2\sqrt{2}}{3}\sqrt{\alpha\beta}$ is readily obtained by inserting the equilibrium profile for C in the expression for free energy 4 and integrating over the interface. Van der Waals was the first to propose a free energy formulation similar to the one given above, where a diffuse interface separates the two different fluids. Cahn

& Hilliard (1958) extended Van der Waals theory to a time-dependent situation by approximating the diffusive fluxes as proportional to gradients of the chemical potential,

$$\frac{\partial C}{\partial t} + \mathbf{u}^* \cdot \nabla C = -\nabla \cdot \mathbf{J} = \nabla \cdot \left(M \nabla (\beta \Psi'(C) - \alpha \nabla^2 C) \right), \tag{6}$$

where $-\mathbf{J} = M\nabla \phi^*$ is a flux. We have here also accounted for the effects of the fluids motion and M is a mobility that is considered to be constant.

2.1. Equilibrium wetting boundary condition

Within the phase field theory the boundary condition that accounts for the free energy distribution between the different phases, sets the wetting boundary condition for the interface, see eq. 5. By making the assumption that the interface is at local equilibrium as it wets the solid surface the boundary condition becomes (Villanueva & Amberg (2006)),

$$\alpha \nabla C \cdot \mathbf{n} + \sigma \cos(\theta_0) g'(C) = 0. \tag{7}$$

We have here used Young's equation relating the equilibrium static contact angle to the surface tension coefficients (σ) : $\sigma \cos(\theta_0) = \sigma_{sg} - \sigma_{sl}$.

The assumption of local equilibrium at the solid surface has been a widespread assumption in phase field wetting simulations, which has proven to be successful in describing numerous physical phenomena involving moving contact lines (Do-Quang & Amberg (2009), Villanueva & Amberg (2006a), Ding & Spelt (2007), Jacquin (1999) and Yue et al. (2010)). One of the strong arguments that speak in favor of the equilibrium assumption is that it has been found in good agreement with the hydrodynamic wetting theory. Yue et al. (2010) matched phase field simulations with the wetting relation by Cox (1986) and proposed a new interpretation of the ad-hoc microscopic length needed in this relation. This length was found to scale with the mobility between the phases and the viscosity. Villanueva & Amberg (2006) showed that numerical phase field wetting simulations were in good agreement with the experimental results of Hoffman (1975). Hoffmann's experiments show a fairly universal relationship between the apparent, observable, contact angle and the capillary number. This is in good agreement with the analytical expressions by Voinov (1976), Tanner (1979) and Cox (1986). Based on the equilibrium wetting condition Jacqmin (1999) showed using asymptotic analysis that the phase field boundary condition given in eq. 7 converged to a relationship between the apparent contact angle and the capillary number.

2.2. Non-equilibrium wetting boundary condition

Although the equilibrium wetting assumption has been found to capture many physical wetting phenomena, it has been demonstrated by Carlson *et al.* (2009) that this assumption is inadequate for rapidly spreading droplets. In order to capture this rapid wetting regime, which has an additional dissipative mechanism, it is crucial to allow for a relaxation from non-equilibrium towards an

equilibrium state. A non-equilibrium boundary condition is incorporated in the phase field framework, and has been discussed previously by different authors, see Jacqmin (2000), Qian *et al.* (2003). However, its importance in practical simulations has only just recently been investigated (Carlson *et al.* (2009)).

The boundary condition in eq. 7 is modified to account for non-equilibrium at the contact line. The phenomenological argument inherent in the phase field method, leading from a free energy to partial differential equations, consists of requiring the irreversible evolution of the system to be such that the free energy is always decreasing. The boundary condition as given in equation 7 will not give any dissipation at the contact line. This is readily modified to allow for dissipation, if, instead of setting the argument of the surface integral in equation 5 to zero, permissible changes in C are made proportional to $\alpha \nabla C \cdot \mathbf{n} + \sigma \cos(\theta_0) g'(C)$, so that the resulting change in free energy is negative definite. The off equilibrium perturbations are counter acted by a diffusive flux proportional to $D_W^* \frac{\partial C}{\partial t}$, where D_W^* is a phenomenological parameter, analogous to a mobility, leading to a non-zero contribution on the right hand side of eq. 7. This gives then the non-equilibrium boundary condition governing rapid wetting

$$\alpha \nabla C \cdot \mathbf{n} + \sigma \cos(\theta_0) g'(C) = D_W^* \frac{\partial C}{\partial t}.$$
 (8)

 D_W^* is believed to originate from the molecular interactions at the contact line, as they reorganize in a diffusive process causing contact line motion (Carlson *et al.* (2009)). No-slip is prescribed at the solid surface.

2.3. Governing equations for the fluids motion

We consider here a system consisting of a two phase flow of air and water, where both are considered as incompressible. Experiments have shown (Bird et al. (2008)) that the contact line has a maximum speed of around one meter per second, so no significant compressible effect is expected in the air and it is therefore treated here as an incompressible phase.

$$\nabla \cdot \mathbf{u}^* = 0. \tag{9}$$

$$\rho^{*}(C) \left(\frac{\partial \mathbf{u}^{*}}{\partial t} + (\mathbf{u}^{*} \cdot \nabla) \, \mathbf{u}^{*} \right) = -\nabla P^{*}$$

$$+ \nabla \cdot \left(\mu^{*}(C) (\nabla \mathbf{u}^{*} + (\nabla \mathbf{u}^{*})^{T}) \right) - \rho(C) g \mathbf{e}_{\mathbf{z}} - C \nabla \phi^{*}$$
(10)

where \mathbf{u}^* is the velocity and P^* is the modified pressure, see Jacqmin (1999). $\rho(C)$ and $\mu(C)$ are the fluids density and dynamic viscosity, which are given as functions of the order parameter C; $\rho^*(C) = \frac{1}{2} \left(\rho_l(C+1) - \rho_g(C-1) \right)$, $\mu^*(C) = \frac{1}{2} \left(\mu_l(C+1) - \mu_g(C-1) \right)$. The subscript l denotes liquid and the subscript l denotes gas, using the material parameters for water and air. l is gravity and l is the unity vector in the z-direction. The

last term is expressing the potential form of the surface tension force, proposed by Jacqmin (1999).

2.4. Non-dimensional formulation

The governing equations are made dimensionless based on the characteristic parameters of the flow, giving the dimensionless variables

$$z^* = Lz, \ t^* = \frac{L}{U}t, \ P^* = \frac{\mu_l U}{L}P, \ u = Uu^*, \ \phi^* = \frac{3\sigma}{2\sqrt{2}\epsilon}\phi$$
 (11)

where the dimensional variables are denoted with *. L is a characteristic length scale, here chosen as the initial droplet radius, and U is the reference velocity. The reference velocity is considered to be the capillary speed $U = \frac{\sigma}{\mu}$. By introducing this scaling into the Navier Stokes and the Cahn–Hilliard equation we obtain their non-dimensional form, here considered in cylindrical coordinates,

$$\nabla \cdot \mathbf{u} = 0, \tag{12}$$

$$\frac{\partial C}{\partial t} + \mathbf{u} \cdot \nabla C = \frac{1}{Pe} \nabla^2 \phi = \frac{1}{Pe} \nabla^2 \left(\Psi'(C) - Cn^2 \nabla^2 C \right), \tag{13}$$

$$\frac{\rho(C)}{\rho_l} \left(\frac{\partial \mathbf{u}}{\partial t} + (\mathbf{u} \cdot \nabla) \mathbf{u} \right) = -\nabla P
+ \frac{1}{Re} \left(\nabla \cdot \left(\frac{\mu(C)}{\mu_l} (\nabla \mathbf{u} + (\nabla \mathbf{u})^T) \right) - \frac{Bo}{Ca} \frac{\rho(C)}{\rho_l} \mathbf{e_z} - \frac{C \nabla \phi}{Cn \cdot Ca} \right).$$
(14)

This gives five non-dimensional numbers;

$$Pe = \frac{2\sqrt{2}U\epsilon L}{3M\sigma}, \quad Cn = \frac{\epsilon}{L}, \quad Re = \frac{\rho_l UL}{\mu_l}, \quad Ca = \frac{2\sqrt{2}\mu_l U}{3\sigma}, \quad Bo = \frac{(\rho_l - \rho_g)gL^2}{\sigma}.$$
(15)

The Peclet number (Pe) expresses the ratio between the advection and diffusion. The Cahn number (Cn) expresses the ratio between the interface width and the characteristic length scale. The Reynolds number (Re) expresses the ratio between the inertia and viscous forces. The Capillary number (Ca) expresses the ratio between the viscous and the surface tension force. The Bond number (Bo) expresses the ratio between the gravitational and surface tension force.

The wetting boundary condition is scaled in accordance with Carlson *et al.* (2009) $D_W^* = \frac{k_B T}{\lambda^2 k_0}$, here λ is the molecular hopping length, k_0 their characteristic frequency, k_b is the Boltzmann constant and T the temperature. This gives the dimensionless general wetting boundary condition

$$D_W \frac{\partial C}{\partial t} = Cn\nabla C \cdot \mathbf{n} + \cos(\theta_0)g'(C). \tag{16}$$

 $D_W = \frac{D_W^*}{\mu L} = \frac{Kn}{Ag}$ is a phenomenological parameter and described in terms of two additional non-dimensional numbers, where $Kn = \frac{\lambda}{L}$ is a type of Knudsen number giving the ratio between the molecular hopping length and the characteristic length scale. In the phase field context it is natural to interpret Kn in terms of the Cahn number, which we will return to below. $Ag = \frac{\mu_l U_M}{\sigma_M}$ is a new non-dimensional number where $U_M = k_0 \lambda$ is the mean molecular hopping velocity and $\sigma_M = \frac{k_b T}{\lambda^2}$ is the energy required to break the liquid-solid bonds due to the hopping between adsorption sites. Thus, Ag represents the ratio between the viscous force and the energy needed to break solid-liquid bonds associated with the molecular hopping (Carlson et al. (2009)).

On all solid walls a no–slip boundary condition $\mathbf{u}=0$ is imposed, and a Neumann boundary condition is applied for the pressure. Vise-versa apply for the outlets of the domain, with a Neumann boundary condition for the velocities and the pressure is defined as P=0.

2.5. Computational methodology

The axi-symmetric governing equations have been solved numerically with the finite element toolbox FemLego (Amberg et al. (1999)). FemLego is an open source symbolic tool for solving partial differential equations. Within a single Maple worksheet the partial differential equations, boundary conditions and numerical solvers are all defined. It inherits parallel computational and adaptive mesh refinement capabilities, see Do-Quang et al. (2007) for details.

The Cahn-Hilliard equation has been solved with a type of precondition Conjugate Gradient (CG) solver, described by Villanueva & Amberg (2006). The multifluid Navier-Stokes equations have been solved with a projection scheme, which was proposed by Guermond & Quartapelle (2000). The linear system for the velocities and pressure have been, respectively, solved with the General Minimum Residual method and a CG solver. All variables are approximated with linear base-functions and the mesh consist of triangular elements.

An adaptive mesh refinement method has been applied in the simulations (Do-Quang et al. (2007)), enabling a high resolution of the key features in the flow, here being the interface. This allows us to resolve small length scales in the flow without having an excessive computational time. The droplet radius is discretized with approximately forty node points and the interfacial area has about a six times higher mesh resolution.

3. Prediction of spontaneous spreading of water droplets

3.1. Scope and simulation setup

Here we will present numerical simulations in direct accordance with the droplet spreading experiments performed by Bird *et al.* (2008). A water droplet with a radius L=0.78mm in air is simulated as it wets three solid surfaces with different degrees of wettability. The material properties for air are denoted

by the subscript g and the material properties for water are denoted by the subscript l. The density is $\rho_l = 998kg/m^3$, $\rho_g = 1.2kg/m^3$, the viscosity is $\mu_l = 10^{-3}Pas$, $\mu_g = 1.6 \cdot 10^{-5}Pas$, gravity is $g = 9.81m/s^2$ and the surface tension coefficient is $\sigma = 0.073 N/m$. This gives the characteristic capillary velocity $U = \frac{\sigma}{\mu_l} = 73m/s$, it should however be noted that the actual speed in the simulations are much less than this value $U_{max} \sim 1 \text{m/s}$. This gives then the non-dimensional numbers based on the liquid material properties, Re=56940, Ca=1 and Bo=0.08. The mass diffusion coefficient has been chosen as $D = 5.7 \cdot 10^{-6} m^2/s$ giving a Peclet number $Pe = 1 \cdot 10^4$. The choice of Pe for the simulations presented here does not influence the results. A short discussion around the influence of Pe on the flow is presented below. In addition to the material properties for the gas and liquid we define the static equilibrium contact angle for the three solid surfaces as $\theta_0 = [3^{\circ}, 43^{\circ}, 117^{\circ}]$. Since these parameters are the same as in the experiments by Bird et al. (2008) we choose to keep these fixed in the simulations, where we only vary the rate coefficient D_W that is determined from the experimental data. After determining D_W the model has in principle no adjustable parameters, as we will show below that the width of the interface does not influence the simulation results in a noticeable way. The model as presented enables then modeling of dynamic wetting without making any ad-hoc physical assumptions.

Fig. 1 shows the axis-symmetric simulation setup and the initial condition. Initially the droplet has a spherical shape and is placed underneath a rod, imitating the needle used in the experiments. In the simulations the contact line is allowed to move across the surface of the rod, while in the experiments liquid is always retained at the tip of the needle. In order to keep the droplet attached to the rod surface, it has been given an equilibrium contact angle of $\theta_0 = 90^{\circ}$. At the lower surface, which the droplet spreads onto, the non-equilibrium boundary condition 8 is used. In order to minimize the influence of the initial condition in the simulations, the droplet is at first not put in direct contact with the wall. It is placed so that a thin air layer, in the wall normal direction, separates the interface and the wall with a thickness that is less than the interface width. This way the onset of wetting is captured without initially prescribing an artificial contact angle at the surface.

3.2. Spreading rate

The detailed evolution of the contact line motion of droplets spreading over solid surfaces with different degrees of wettability was described by Bird et al. (2008). Their experiments provide excellent data for a fidelity check of macroscopic contact line models for dynamic wetting, as the observed contact angle, in these experiments, changes in time as the droplets spread. We have here extracted and focused on the experimental results of water droplets with a radius L=0.78mm, that wets three solid surfaces with different degrees of wettability $\theta_0 = [3^{\circ}, 43^{\circ}, 117^{\circ}]$.

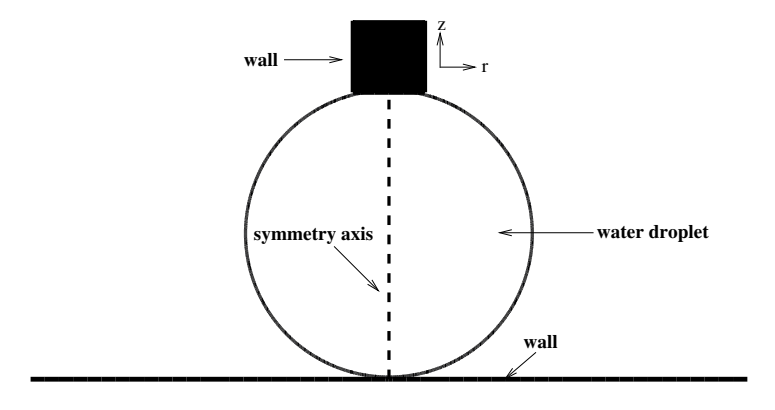


Figure 1: Simulation setup and the initial condition.

Fig. 2 shows the sensitivity and influence of the parameter D_W on the spreading rate as the water droplets wet the different surfaces. Fig. 2a shows the temporal evolution of the contact line as the droplet spreads over a surface with an equilibrium angle $\theta_0 = 3^{\circ}$. One clear observation is that the equilibrium assumption $(D_W = 0)$ is deficient, as the contact line propagates too fast over the surface. By increasing the coefficient D_W , dissipation is added at the contact line, resulting in a deceleration of the relaxation process towards thermodynamic equilibrium. Best fit with the experimental result is found for $D_W = 1.0$.

For wetting on a solid surface with an equilibrium contact angle $\theta_0 = 43^{\circ}$, see fig. 2b, a similar overall picture as in fig. 2a is observed. The assumption of local equilibrium at the contact line, makes it propagate too fast in comparison with the experimental result by Bird *et al.* (2008). The best match with the experimental results was found for $D_W = 1.4$. We notice that the speed of the contact line is lower here ($\theta_0 = 43^{\circ}$) than what was observed on a surface that is more wettable, see fig. 2a. This effect is due to a lower local forcing in the contact line region, as the initial wetting is closer to its equilibrium state.

For a nearly hydrophobic surface ($\theta_0 = 117^{\circ}$) the equilibrium assumption seems to give results that are quite coherent with the experimental wetting, see fig. 2c. A slight improvement might be seen in the spreading prediction using the coefficient, $D_W = 0.2$.

To summarize the results in fig. 2 we notice that, for the case studied here, the equilibrium wetting boundary condition fails to correctly predict the wetting speed on hydrophilic surfaces. By introducing another dissipative mechanism, we thus obtain a direct agreement with the experimental results by Bird et al. (2008). The rate coefficient appearing in the non-equilibrium boundary condition is determined from the experimental data, and best fit is observed for

 $D_W = [1.0, 1.4, 0.2]$ for surfaces with $\theta_0 = [3^{\circ}, 43^{\circ}, 117^{\circ}]$, and have been condensed into fig. 1 in Carlson et al. (2009). D_W is believed to be a physically reasonable parameter, that should naturally vary for different systems. We are at the present time lacking a rational explanation for the non-monotonic behavior of the coefficient D_W for the different contact angles, investigated here. However it should be noted that ongoing work based on a micro scale analysis is in progress, but beyond the scope of the present paper.

One peculiar feature that was identified by Bird et~al.~(2008) was that, by using an inertial time scale, the experimental spreading results fell on a master curve, irrespective of droplet size. The spreading curve was found to follow a power law, but the exponent found in the experiments changed with the wettability of the solid substrate. The data did not collapse when a more intuitive viscous time scaling was used. In fig. 3 droplet radius is plotted versus time in logarithmic units, where the triangles are intended to more clearly illustrate the different exponents observed in the power-law for the different solid substrates. Here a nondimensional time $\tau = \frac{t}{\sqrt{\rho_1 L^3}}$ is used, to facilitate comparison with Bird et~al.~(2008). It should be noted that Bird et~al.~(2008) points out that less emphasis should be placed on their results for the initial wetting $(\tau = \frac{t}{\sqrt{\rho_1 L^3}} < 0.1)$, due to the spatial accuracy of their measurements.

The slight discrepancy at late times is likely an effect of differences in the experimental and computational setup. At late times in the experiments the droplet starts to detach from the needle by forming a thin liquid neck that finally pinches off, where liquid is always retained at the tip of the needle. In the simulations a rod mimics the needle, allowing the contact line to move. This would influence the size of the smaller secondary droplet as well as the time for the collapse of the liquid neck as the larger droplet detaches.

A dramatic change in the spreading characteristics is observed for all three cases around the time $\tau=3$ in both the simulations and the experiments. The same behavior was found also with the equilibrium boundary condition. This spreading behavior was explained as a transition between the inertial and the viscously dominated wetting (Bird *et al.* (2008)). The simulations of a highly wettable surface ($\theta_0=3^\circ$) are stopped before this time, since the contact line leaves the domain before reaching the transition. Later in this article we will present the dissipative mechanisms and the rate-of-change of kinetic energy.

By applying the criterion for the transition between inertial and viscous wetting, proposed by Biance et al. (2004), we obtain a specific time $\tau_t \sim \left(\frac{\rho \sigma L}{\mu^2}\right)^{\frac{1}{8}}$ where the transition should approximately take place. By introducing the material parameters for the simulated cases we obtain $\tau=3.9$, which is in good agreement with the experimental and numerical data, see fig. 3.

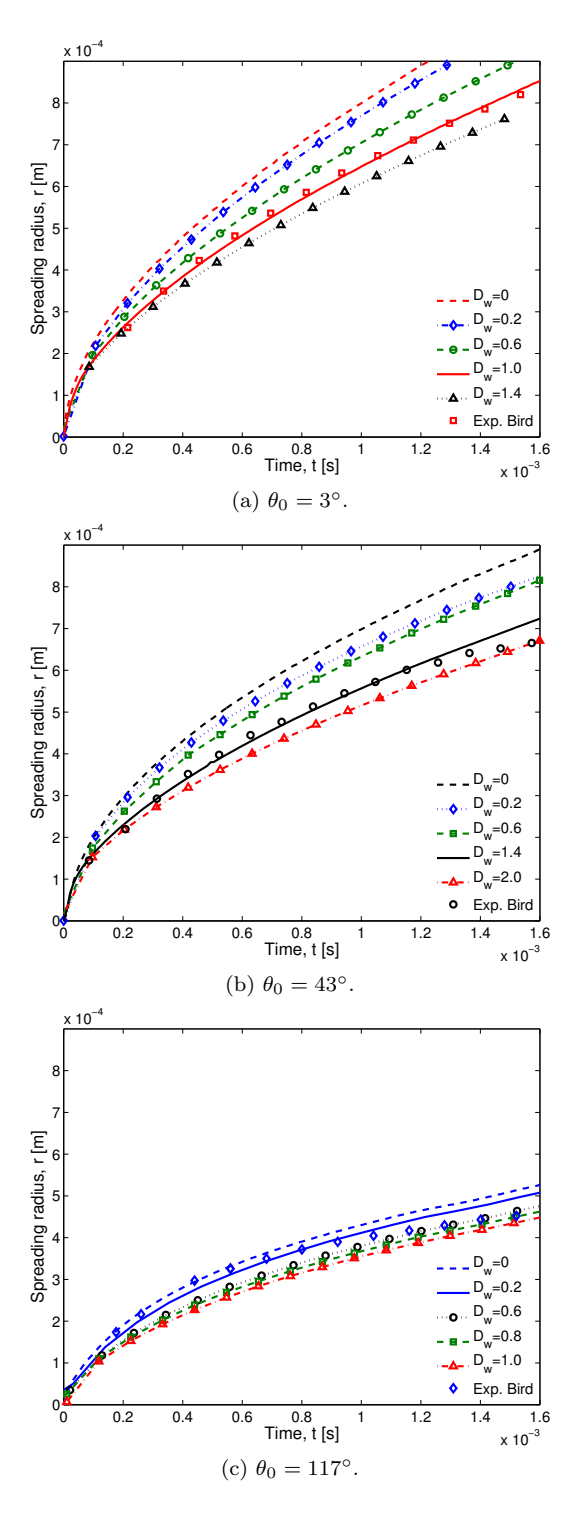


Figure 2: The temporal evolution droplets spreading radius with L=0.78mm and the influence of D_W on the results as it wets three solid surfaces with different degrees of wettability; $\theta_0 = [3^\circ, 43^\circ, 117^\circ]$. The fully drawn line, in each sub-figure, represents the best match with the experiment.

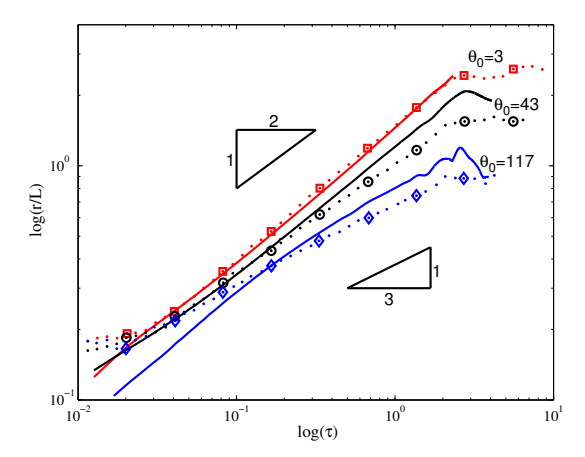


Figure 3: Comparison between the experimental and numerically predicted droplet spreading radius with logarithmic axes. The full lines denote the simulations and the dotted lines with markers the experimental master curve from Bird *et al.* (2008).

3.3. Interfacial evolution and dynamic contact angles

Fig. 4, 5, 6 show the droplet shape and velocity vectors for a water droplet spreading on three solid surfaces with an equilibrium contact angle of $\theta_0 = [3^{\circ}, 43^{\circ}, 117^{\circ}]$. The left half of each panel in fig. 4, 5, 6 shows the simulations with the non-equilibrium wetting boundary condition 8, labeled dynamic, and the right panel the results with the local equilibrium condition 7, labeled static. The wording "dynamic" and "static" does in this context denote the contact angle boundary condition at the solid surface, which is changing in time in the former and fixed in the latter. The apparent contact angle is changing in time with both of the boundary conditions.

Fig. 4 shows four snapshots in time of the droplet as it spreads on a solid surface with an equilibrium contact angle $\theta_0 = 3^{\circ}$. In fig. 4a the droplet has just started to wet the solid surface and has propagated about one third of its initial radius. A larger contact angle is observed with the non-equilibrium boundary condition, left half, than with the assumption of local equilibrium, right half. Both of the wetting boundary conditions produce a smooth velocity profile in the domain, being largest in the vicinity of the contact line. A flow recirculation is observed with both models, with a larger local curvature is predicted with the static model.

The two different models predict a somewhat different shape of the droplets interface. We see clearly that the equilibrium assumption propagates too fast over the solid surface, see fig. 4b. A capillary wave is generated at the onset of wetting, fig. 4a, which propagates across the droplet. This wave is visible in all of the sub-plots in fig. 4. The wave propagates across the droplet before its

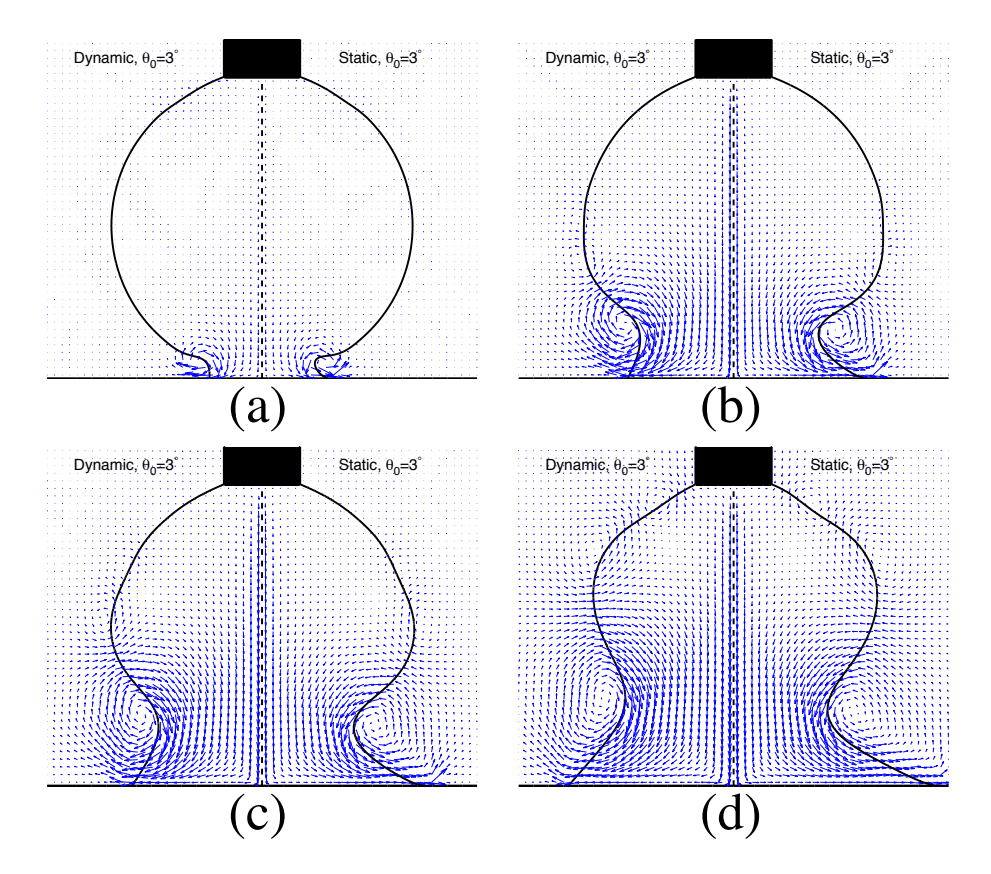


Figure 4: Numerically predicted velocity profile and droplet shape for a droplet spreading on a solid surface with an equilibrium contact angle $\theta_0 = 3^{\circ}$ at four snapshots in time [a: $\tau = 0.04$, b: $\tau = 0.22$, c: $\tau = 0.43$, d: $\tau = 0.63$]. The left subfigure in each panel shows the result with the dynamic treatment with $D_W = 0.5$ and the right subfigure the result using equilibrium assumption with $D_W = 0$.

energy is finally dissipated. By comparing these results with the experiments by Bird et al. (2008) we notice that the equilibrium condition over-predicts the amplitude of the capillary wave, as it relaxes faster towards its equilibrium contact angle. As the contact line moves across the solid surface we notice two small secondary flows close to the rod, see fig. 4d. These flow patterns are generated due to a local change in the curvature of the interface.

We have extracted the contact angle from the numerical simulations with the non-equilibrium boundary condition, as the equilibrium assumption has been found deficient. This was done by extracting the points along the zero contour for C, at several interfacial lengths in the wall normal direction. By

$\theta_0 = 3^{\circ}$	$\tau = 0.16$	$\tau = 0.31$	$\tau = 0.47$
$ heta_e$	71°	58°	52°
$ heta_s$	78°	63°	52°

Table 1: Comparison of the experimental and numerical predicted dynamic contact angle for a solid surface with an equilibrium contact angle $\theta_0 = 3^{\circ}$, where θ_e is the experimental and θ_s is the numerically predicted apparent dynamic contact angle.

drawing a tangent through these points, we were able to measure the observable dynamic contact angle. These results have been compared with the experimental results from Bird et al. (2008), see table (1). The apparent contact angle from Bird et al. (2008) has been extracted in a similar fashion as the simulation results, by drawing a tangent along the interface close to the solid surface. Here θ_e is the experimental and θ_s numerically predicted contact angle with the non-equilibrium condition. A direct match is found in time, between the measured numerical and experimental apparent dynamic contact angle, indicating that we have captured the correct value for the coefficient D_W , see tab.(1).

Fig. 5 shows the simulation results of a water droplet that spreads on a solid surface with an equilibrium contact angle $\theta_0 = 43^{\circ}$. In the initial stage of the spreading, see fig. 5a, we notice a large discrepancy between the predicted apparent contact angles with the two different wetting boundary conditions. By comparing the result using the equilibrium assumption with the experimental results by Bird *et al.* (2008), we observe that neither the contact angle nor the capillary wave is in coherence with the experiments. Good agreement is found with the local dynamic treatment. As the contact line moves in time the difference in droplet shape predicted by the two boundary conditions becomes more pronounced, see fig. 5b. A large flow recirculation is observed at the capillary wave (fig. 5c) where two secondary vortices are formed as the wave approaches the needle/rod, see fig. 5d.

A comparison between the predicted contact angle from the dynamic treatment and the experiments in time are given in table (2). In this partial wetting regime, there is a slight deviation between the experimental and numerical dynamic contact angle. One explanation for the deviation can be that the coefficient D_W could be better fitted, for instance maybe against θ_e in time instead of the spreading radius.

Fig. 6 shows the droplet spreading on a solid surface with an equilibrium contact angle $\theta_0 = 117^{\circ}$. We notice, as also observed in fig. 2c, that the result with the non-equilibrium and equilibrium boundary conditions are hard to distinguish from each other. The flow field is almost identical with the two boundary conditions. A slight difference in the droplet shape can be seen in the initial wetting, where the contact angle is slightly larger with the dynamic treatment, see fig. 6a-6b. A flow recirculation is observed as the capillary

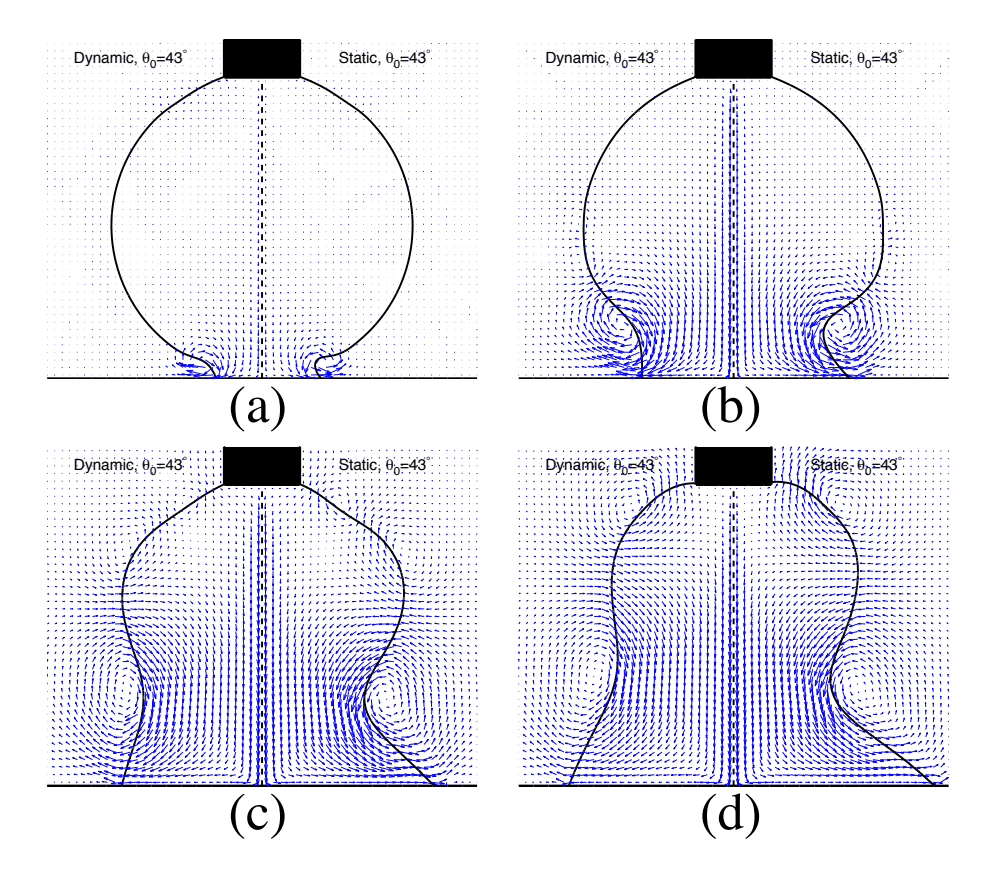


Figure 5: Numerically predicted velocity profile and droplet shape for a droplet spreading on a solid surface with an equilibrium contact angle $\theta_0 = 43^{\circ}$ at four snapshots in time [a: $\tau = 0.04$, b: $\tau = 0.22$, c: $\tau = 0.63$, d: $\tau = 0.82$]. The left subfigure in each panel shows the result with the dynamic treatment with $D_W = 0.7$ and the right subfigure the result using equilibrium assumption with $D_W = 0$.

.

wave propagates across the droplet (fig. 6c). In comparison with the observed wetting in fig. 4, 5 the droplet relaxes faster to its equilibrium state, see fig. 6d. The numerically predicted dynamic contact angle gives a direct match with the experimental results from Bird *et al.* (2008), see table (3).

3.4. Dynamic contact angle relaxation

Based on the results presented in fig. 4, 5, 6 it is clear that the dynamic contact angle predicted with the two boundary conditions are different. The dynamic contact angle (θ_s) has been extracted from the simulations as it evolves in time,

$$\begin{array}{cccc} \theta_0 = 43^\circ & \tau = 0.16 & \tau = 0.31 & \tau = 0.47 \\ \theta_e & 107^\circ & 99^\circ & 96^\circ \\ \theta_s & 107^\circ & 88^\circ & 79^\circ \end{array}$$

Table 2: Comparison of the experimental and numerical predicted dynamic contact angle for a solid surface with an equilibrium contact angle $\theta_0 = 43^{\circ}$, where θ_e is the experimental and θ_s is the numerically predicted apparent dynamic contact angle.

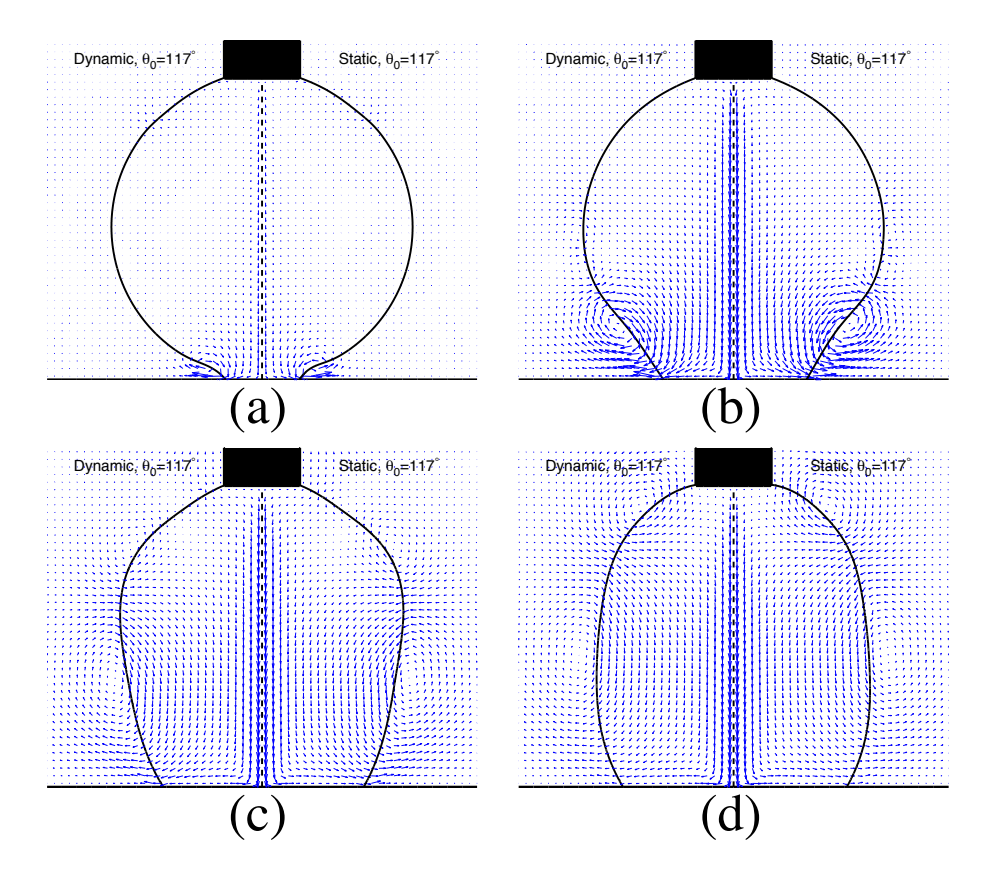


Figure 6: Numerically predicted velocity profile and droplet shape for a droplet spreading on a solid surface with an equilibrium contact angle $\theta_0 = 117^{\circ}$ at four snapshots in time [a: $\tau = 0.04$, b: $\tau = 0.43$, c: $\tau = 0.63$, d: $\tau = 0.82$]. The left subfigure shows the dynamic treatment with $D_W = 0.1$ and the right subfigure the equilibrium assumption with $D_W = 0$.

$\theta_0 = 117^{\circ}$	$\tau = 0.16$	$\tau = 0.31$	$\tau = 0.47$
$ heta_e$	147°	125°	120°
θ_s	132°	123°	120°

Table 3: Comparison of the experimental and numerical predicted dynamic contact angle for a solid surface with an equilibrium contact angle $\theta_0 = 117^{\circ}$, where θ_e is the experimental and θ_s is the numerically predicted apparent dynamic contact angle.

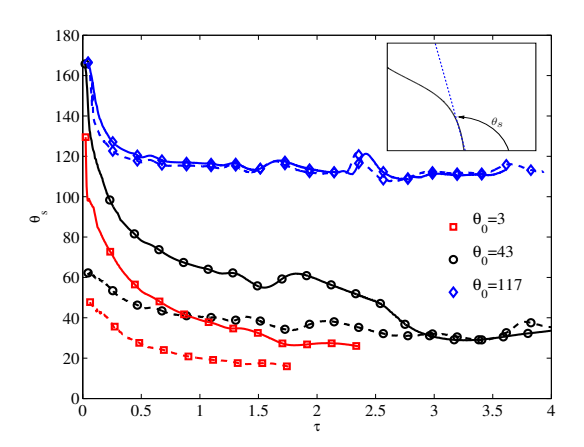


Figure 7: Temporal evolution of the dynamic contact angle evolution using the local equilibrium assumption boundary condition (dotted lines) and the non-equilibrium boundary condition (full lines). The inset in the upper right shows schematically how the contact angle is extracted along the C=0 contour.

see fig. 7. This was done by fitting a tangent through the points along the zero contour of the phase field parameter C, at a well defined height in the wall normal direction (z-axis). In order to say something with fidelity about the dynamic contact angle, several points are needed in the interpolation. As the droplet starts to wet the dry solid surface, the interface forms a small radius of curvature see fig. 4, 5, 6. To extract the proper dynamic contact angle it is important not to interpolate the contact angle at a too small or large height in the z-direction from the solid surface, since the former would produce an inaccurate result and the latter interpolate the wrong angle. The first time steps, when the radius of curvature is in the same order of magnitude as ϵ , have been disregarded, as there are not sufficient points in order to extract the contact angle with fidelity. In the first spreading phase the radius of curvature in the foot-region changes rapidly, and the interpolation height in z-direction has been taken to be equal to this radius. The wall normal interpolation height

is fixed to 15ϵ when the radius of curvature exceeds this length. The inset in fig. 7 shows schematically how the dynamic contact angle is extracted. For the simulations with the equilibrium boundary condition, points closer than ϵ from the wall have been neglected when extracting the dynamic contact angle, since the equilibrium contact angle is imposed here.

One observation to be made in fig. 7 is that the results obtained with the non-equilibrium boundary condition evolve towards the static contact angle (θ_0) much more slowly than with the equilibrium condition. For the cases with the non-equilibrium condition the droplet starts to wet with a high contact angle, close to 160° . As it spreads across the surface, the contact angle changes and relaxes towards its equilibrium condition. In the initial short-time spreading the dynamic contact angle varies rapidly.

The results with the equilibrium condition reveal that the droplet starts to wet with a contact angle that is much closer to its equilibrium angle. As the droplet spreads the dynamic contact angle varies, although not with such a span in angles as observed with the non-equilibrium condition. It seems that the temporal contact angle relaxation is much shorter with the equilibrium assumption than with the non-equilibrium condition.

The evolution of the contact angle for the surface that does not wet well, ($\theta_0 = 117^{\circ}$), shows that there is no significant effect by using the non-equilibrium condition for this hydrophobic case. This result is in accordance with the finding in fig. 2c.

Fig. 7 also reveals that the hydrodynamic forces present in the flow influence the evolution of the dynamic contact angle. For instance an effect from the capillary wave can be seen in all cases around the time $\tau \sim 1.6$. This is due to the formation of a liquid neck along the symmetry axis as the droplet spreads. As the neck breaks off two separate droplets are formed, one large on the lower surface and a small secondary droplet on the needle. This makes the droplets and the contact angles oscillate, see fig. 7 for $\theta_0 = [43^\circ, 117^\circ]$ after time $\tau = 2.0$. The influence of the breakup on the dynamic contact angle is clearly observed for the case when $\theta_0 = 117^\circ$, as the surface tension contracts the droplets. Detachment from the upper wall takes place at a slightly later time, $\tau = 3.1$, with the equilibrium condition when $\theta_0 = 43^\circ$, a different size is also predicted for the two droplets.

3.5. Influence of the interface width and bulk diffusion

One difficulty of the phase field method is that the interface width in practical simulations has to be taken much larger than what can be motivated physically. In the numerical experiments shown here, a Cahn number of $Cn = 10^{-2}$ has been applied. This means that in the simulations the width of the interface is $\epsilon = 7.8 \mu m$. Comparing the numerical and actual physical width of the interface, being in the order of a couple of Ångström, it is clear that this numerical width does not account for the interfacial physics on length scales below ϵ . However, we will verify that the macroscopic results of the simulations are insensitive to

the interface width (i.e. the Cahn number), and that this can be considered as a numerical parameter in the present context.

To show that the phase field method can capture macroscopic phenomena with accuracy, it is important to show that the simulation results are fairly independent of the width of the numerical interface. Several authors, Carlson et al. (2010), Villanueva & Amberg (2006), Yue et al. (2010) and Ding & Spelt (2007), have previously demonstrated this. Since we here explore a term that have typically been neglected in phase field simulations, we have investigated the effect of Cn and Pe on the simulated wetting physics. Fig. 8 shows the shape of the droplet for four simulations, with different Cn and Pe. A direct match between all the different cases is obtained for the droplet shape as well as the wetting foot-region. As these interface widths did not have any noticeable effect on the results, we are satisfied that the results are insensitive to values of Cn and Pe. Additional simulations, not presented here, with the equilibrium boundary condition show that the results were also insensitive to the Cn and Pe numbers presented in fig. 8.

In the phase field context it is thus natural to interpret Kn, appearing in the non-dimensional number $D_W = \frac{D_W^*}{\mu L} = \frac{Kn}{Ag}$ as being similar to the Cahn number Cn. A set of simulations were performed where the interface width was changed nearly one order of magnitude between $Cn = 2 \cdot 10^{-2}$ and $Cn = 0.25 \cdot 10^{-2}$. By changing the Cn number but retaining the same D_W it was observed in the simulations that the contact line did not obtain the same speed. However, if the ratio $\frac{D_W}{Cn}$ is held constant, the droplet shape remains nearly independent of the interface width as it spreads in time. This is shown in fig. 8 where $\frac{D_W}{Cn} = 140$, indicating that it seems reasonable to interpret $\frac{D_W^*}{\epsilon}$ as a constant independent of the interface width.

The results for different Cn numbers are shown in fig. 8, where no significant effect of the interface width was seen in the simulations, demonstrating that the use of a finite interface width can only have a very minor influence on the wetting simulations presented here. It seems for now also reasonable to interpret Ag as a non-dimensional number that is independent of the interface width. Yue et~al.~(2010) showed that to obtain convergent phase field contact line simulations with respect to the interface width, analogous to a sharp-interface limit, the simulations should satisfy $4 > \sqrt{Pe\,Cn}$ with the scaling used in the present work. Remembering that the predicted velocity in the simulations is about two orders of magnitudes less than the characteristic velocity $U = \frac{\sigma}{\mu}$, we notice that all simulations presented here satisfies the proposed condition for convergent results for moving contact lines, as already indicated in fig. 8.

A question that naturally arises is whether the non-equilibrium boundary condition will hold in the limit of a vanishing interface width ($\epsilon \to 0$). Wang & Wang (2007) studied the asymptotic behavior of the solution of the Cahn-Hilliard equations, by expanding the phase field variable in terms of the interface width. Near the contact line the outer solution was shown to behave

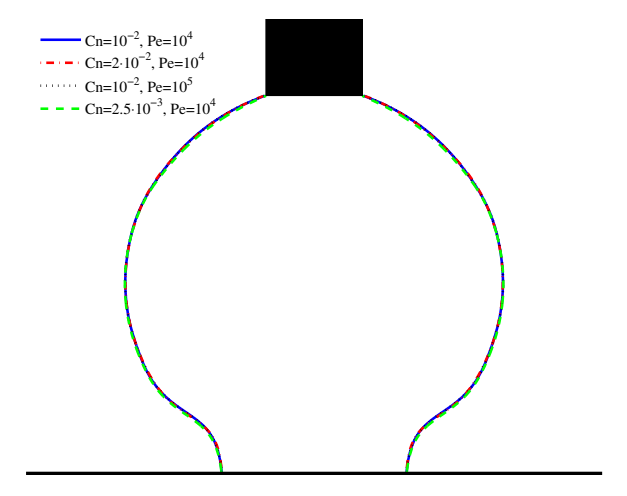


Figure 8: Effects of the interface width and bulk diffusion in the simulations for a wetting droplet on a solid surface with $\theta_0 = 43^{\circ}$ and $D_W = \frac{Kn}{Ag} = \frac{Cn}{Ag}$. $\frac{D_W}{Cn} = 140$ for the four cases shown above with different Cn and Pe.

regularly, although they did not obtain a solution for the inner contact line region. They pointed out that the deviation from the equilibrium contact angle, would indeed depend on the inner structure of the interface at the contact line. It is in this region where the diffusive slip would act as a mechanism for the contact line movement. Based on the study by Wang & Wang (2007), Yue et al. (2010) noted that it still remains unclear wether such a sharp-interface limit exists for the Cahn-Hilliard model. However, Qian et al. (2004) and coworkers made a detailed comparison between the contact line motion predicted with molecular dynamics simulations and with phase field modeling. Excellent agreement was obtained for the slip profile at the nano-scale, where most parameters in the phase field equations were given directly from the molecular dynamics calculations. The non-equilibrium boundary condition, retaining a non-zero D_W , was demonstrated to be of great importance in order to obtain a matching phase field solution with the molecular dynamics simulations. They found that the contact line dissipation is an important contribution to the total dissipation at small length scales, a result that is in agreement with the findings presented in sec. 4.

4. Governing dissipative mechanisms in rapid dynamic wetting

To identify the different mechanisms that govern the dynamic wetting process, the different rates of dissipation have been extracted from the flow. This has been done in accordance with the methodology presented by Qian *et al.* (2009b),

Wang et al. (2008). These dissipative mechanisms are the viscous dissipation (\dot{R}_{μ}^{*}) , the diffusive fluxes of the chemical potential (\dot{R}_{D}^{*}) and the contact line relaxation at the solid surface (\dot{R}_{DW}^{*}) . However, during rapid dynamic wetting, some of the released energy is converted into bulk kinetic energy, and thus the force balance that determines the wetting speed involves the liquid inertia (Biance et al. (2004)). Therefore, the rate of change of kinetic energy (\dot{R}_{ρ}^{*}) is also extracted from the flow. To identify the primary cause for resistance to spreading, the relative magnitude of these four rates $(\dot{R}_{\mu}^{*}, \dot{R}_{DW}^{*}, \dot{R}_{DW}^{*}, \dot{R}_{\rho}^{*})$ are studied as the droplet evolves. These four contributions are scaled with the surface energy $(\dot{R}_{\mu}^{*} = \sigma U L \cdot \dot{R}_{\mu}, \dot{R}_{DW}^{*} = \sigma U L \cdot \dot{R}_{DW}$ and $\dot{R}_{\rho}^{*} = \sigma U L \cdot \dot{R}_{\rho}$) giving their dimensionless form

$$\dot{R}_{\mu} = \int_{\Omega} Ca\mu(C) \nabla \mathbf{u} : (\nabla \mathbf{u} + \nabla^{T} \mathbf{u}) d\Omega, \ \dot{R}_{D} = \int_{\Omega} \frac{C_{n}}{Pe} \left(\frac{\partial \phi}{\partial t}\right)^{2} d\Omega,$$

$$\dot{R}_{DW} = \int_{\Gamma} D_{W} \left(\frac{\partial C}{\partial t}\right)^{2} d\Gamma, \ \dot{R}_{\rho} = \int_{\Omega} \frac{Re \cdot Ca}{2} \frac{\partial \rho(C) \mathbf{u}^{2}}{\partial t} d\Omega.$$
(17)

 \dot{R}_{μ} , \dot{R}_{D} and \dot{R}_{ρ} are bulk contributions (Ω) , while $\dot{R}_{D_{W}}$ is a contribution at the solid surface (Γ) .

Above, the relationship between Cn and D_W was discussed, and it was shown numerically that $\frac{D_W}{Cn} = \frac{1}{Ag}$ is a number independent of the interface width. This indicates also that the dissipation at the contact line as it relaxes towards equilibrium, should also not depend significantly on the interface width. This can also be seen by considering here the rate of change of the order parameter C with the spreading radius (r) at the solid surface where $\frac{\partial C}{\partial t} \sim \frac{\delta C}{\delta r} \frac{\delta r}{\delta t} \sim \frac{1}{\epsilon} \frac{\partial r}{\partial t}$. This gives an estimate for the dissipation from the contact line relaxation; $\dot{R}_{D_W}^* = \int_{\Gamma} D_W^* \frac{\partial C}{\partial t} d\Gamma \sim D_W^* (\frac{1}{\epsilon} \frac{\partial r}{\partial t})^2 2\pi r\epsilon$. This gives then by scaling \dot{R}_{D_W} with the surface energy σUL , $\dot{R}_{D_W} \sim \frac{D_W^*}{\sigma UL} \frac{U^2}{\epsilon^2} r\epsilon \sim \frac{D_W}{Cn} \frac{r}{L} \sim \frac{1}{Ag}$. Assuming here that r is in the same order of magnitude as L and we apply the analogy as introduced above, where D_W is interpreted in terms of Cn. This shows, along with the result presented in fig. 8, that the energy dissipated at the contact line does not significantly depend on Cn.

Fig. 9 shows the rate of dissipation and kinetic energy for a droplet spreading on a solid surface with an equilibrium contact angle $\theta_0 = 43^{\circ}$. Snapshots of the droplet shape at four different times have been placed as insets.

Initially the droplet spreads rapidly across the solid surface and the contact line decelerates as it moves. At time $\tau=2.0$, the extended liquid neck formed along the symmetry axis between the upper and lower wall breaks, forming a large drop on the lower solid surface and a small secondary droplet pinned at the needle tip. It is well known that the contact line dynamics influences the size of the deposited droplets (Qian et al. (2009a)), thus the modeling approach presented here does not only enable a more precise prediction of the contact line spreading but also the prediction of such a droplet deposition process. The breakup time as well as the droplet sizes are different for the equilibrium and

non-equilibrium boundary condition. After breakup of the liquid neck, the droplets on the lower and upper solid surfaces oscillate as they relax into their equilibrium state, see fig. 9. All these processes influence the rate of dissipation as well as the rate of change of kinetic energy, see fig. 9. As the main objective here is to identify the governing mechanisms in the early rapid dynamic wetting we will now focus on the behavior up to the collapse of the liquid neck.

Fig. 10 shows the temporal evolution of the four rates as the droplet spreads over the three different solid surfaces with $\theta_0 = [3^{\circ}, 43^{\circ}, 117^{\circ}]$. These rates are presented until the liquid neck start to collapse ($\tau \sim 1.5$). First, with the incipience of wetting, viscous dissipation is large as seen in all three plots in fig. 10. This is in agreement with the theory proposed by Eggers *et al.* (1999), as a small cusp region is formed at the contact line. This regime has a very short time span, and is quickly replaced by another wetting regime where either the dissipation from the contact line relaxation, or the rate of change of kinetic energy dominates, see fig. 10.

In fig. 10a the four rates are given in time for the initial spreading on a solid surface with $\theta_0 = 3^{\circ}$. Initially the viscous dissipation is large, but reduces rapidly while the dissipation from the contact line and rate of change of kinetic energy starts to increase. In this early wetting, the contact line propagates with a high speed ($\sim 1m/s$) across the solid surface. After the time $\tau \sim 0.05$ the dissipation from the contact line relaxation starts to decrease, and inertia becomes increasingly important. Around time $\tau \sim 0.45$ the dissipation from the contact line and the rate of change of kinetic energy balances each other. Further on, the rate of change of kinetic energy in the bulk dominates the wetting and the spreading dynamics is dominated by inertia. The contribution from the bulk diffusion of the chemical potential is here much less than the three other contributions, and has an insignificant influence on the results.

A similar scenario is observed for the initial wetting on a solid surface with $\theta_0=43^\circ$, see fig. 10b. In comparison with the results for the solid surface with $\theta_0=3^\circ$, it is seen that the transition between the relaxation and inertial wetting takes place at a later point in time, $\tau\sim1.1$, as compared to $\tau\sim0.45$ for $\theta_0=3^\circ$. This result is also in accordance with the values determined for the rate coefficient D_W , as D_W is found to be larger for $\theta_0=43^\circ$ than for $\theta_0=3^\circ$. The magnitude of the different rates are here less than those observed for $\theta_0=3^\circ$, since the contact line moves slower.

A different picture is observed for the spreading on a solid surface that does not wet well ($\theta_0 = 117^{\circ}$), see fig. 10c. Here, viscous dissipation dominates initially, as for the two cases reported above. However, the dissipation from the contact angle relaxation seems to play a minor role in comparison with the viscous dissipation and rate of change of kinetic energy. Instead the viscous dissipation increases in time, contrary to the observations in fig. 10a, 10b, and there is a transition between viscous and inertially dominated wetting around $\tau \sim 0.15$. After this transition, inertia dominates and the viscous dissipation slowly decreases.

The contact line relaxation regime is to our understanding a new dissipative mechanism, which has not previously been known to dominate the initial droplet spreading. This dissipative mechanism is believed to be a reorganization of molecules, in a type of diffusive or active process, at the contact line. In order to model rapid dynamic wetting processes with fidelity, it is important to account for this dissipative mechanism. This term, $(\sim 2\pi r \epsilon D_W(\frac{\partial C}{\partial t})^2)$ resembles the term for contact line dissipation proposed by de Gennes (1985). It is also similar to the dissipation estimated from the molecular kinetics theory (de Ruijter et al. (1999)). At the present time we are not able to determine whether these mechanisms are indeed the same, as this would require first principles studies at the molecular scale, which goes beyond the scope of the present paper. In should however be noted that the scaling for the spreading radius from the molecular kinetic theory $r \sim t^{\frac{1}{7}}$ was not recovered in the simulations, and that this regime has been shown to take place at much later time scales (Seveno et al. (2009), De Coninck et al. (2001)) than what is observed in the simulations. The initial wetting regime found here, serves as an addition to the other wetting regimes that have previously been reported in the literature.

For all three cases the viscous dissipation and the rate of change of kinetic energy balances each other several times, although at slightly different times. Later on viscous dissipation dominates the flow, influencing the spreading rate as also seen in fig. 3. The time for transition from wetting dominated by inertia to viscosity $\tau_t \sim 1.5 \ (t_t)$ is in reasonable correspondence to the result by Biance et al. (2004), $\tau_t = 3.80 \ (t_t \sim 9.7ms)$. Although, it is clear that for late time dynamics hydrodynamic forces like the collapse of the liquid bridge and droplet oscillation influence the phenomena as illustrated in fig. 9.

4.1. Estimating the duration of the relaxation regime

In view of the above, there seems to be a distinct timescale where the dissipation from the contact line dominates the wetting physics. A force balance between the capillary force generated by interface distortion and the contact line relaxation gives an estimate of the spreading radius in this regime. It is in this context natural to interpret the contact line relaxation as a friction force at the contact line, while the capillary force is driving the flow. By following the same methodology as in Biance et al. (2004) it is possible to estimate the spreading radius as a function of time, assuming that the capillary force balances the contact line relaxation force as,

$$2\pi r \cdot D_W^* \frac{dC}{dt} = 2 \cdot \pi r \sigma$$

$$\sim \frac{D_W^*}{\epsilon} \frac{dr}{dt} \sim \sigma$$

$$r \sim \left(\frac{\sigma \epsilon}{D_W^*}\right) t. \tag{18}$$

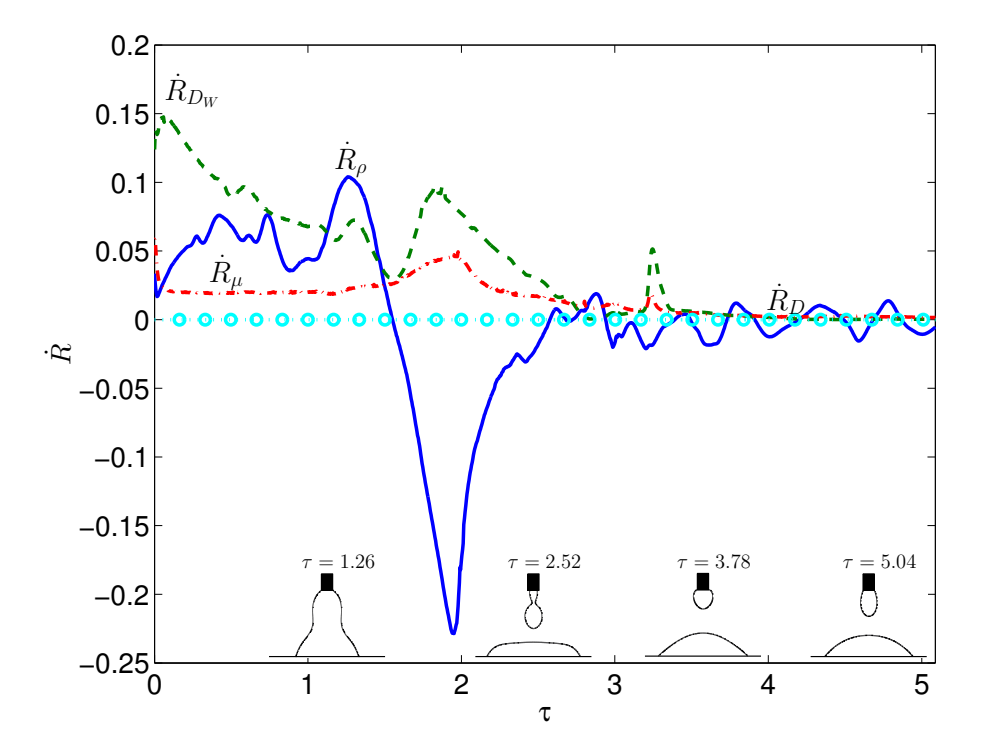


Figure 9: The rate of dissipation in time and the rate of change of kinetic energy for the spreading on a solid surface with $\theta_0=43^\circ$. The full line corresponds to \dot{R}_ρ , dashed line \dot{R}_{DW} , dashed dotted line \dot{R}_μ and the dashed line with round markers to \dot{R}_D . The insets in the lower part of the figure shows the droplet shape corresponding to the time given on the x-axis.

Eq. 18 along with the estimate for the spreading radius for inertial driven wetting (Biance et al. (2004)) $r \sim (\frac{\sigma L}{\rho})^{\frac{1}{4}} t^{\frac{1}{2}}$, gives then a characteristic time for

the transition between the relaxation and the inertial regime,
$$t_t \sim \left(\frac{\left(\frac{\sigma L}{\rho}\right)^{\frac{1}{4}}}{\left(\frac{\sigma \epsilon}{D_w^*}\right)}\right)^2$$
.

By introducing the material properties for the density, rate coefficient, length and surface tension coefficient, the duration of the wetting dominated by the contact line relaxation, and a distinct time for the wetting transition between the inertial and the contact line relaxation regime is obtained. For the three cases reported above the transitional time (t_t) should be $t_t = [0.44, 0.88, 0.018] \text{ms or } \tau_t = [0.18, 0.34, 0.007] \text{ for } \theta_0 = [3^\circ, 43^\circ, 117^\circ]$. These results are in good agreement with the numerically predicted transitional

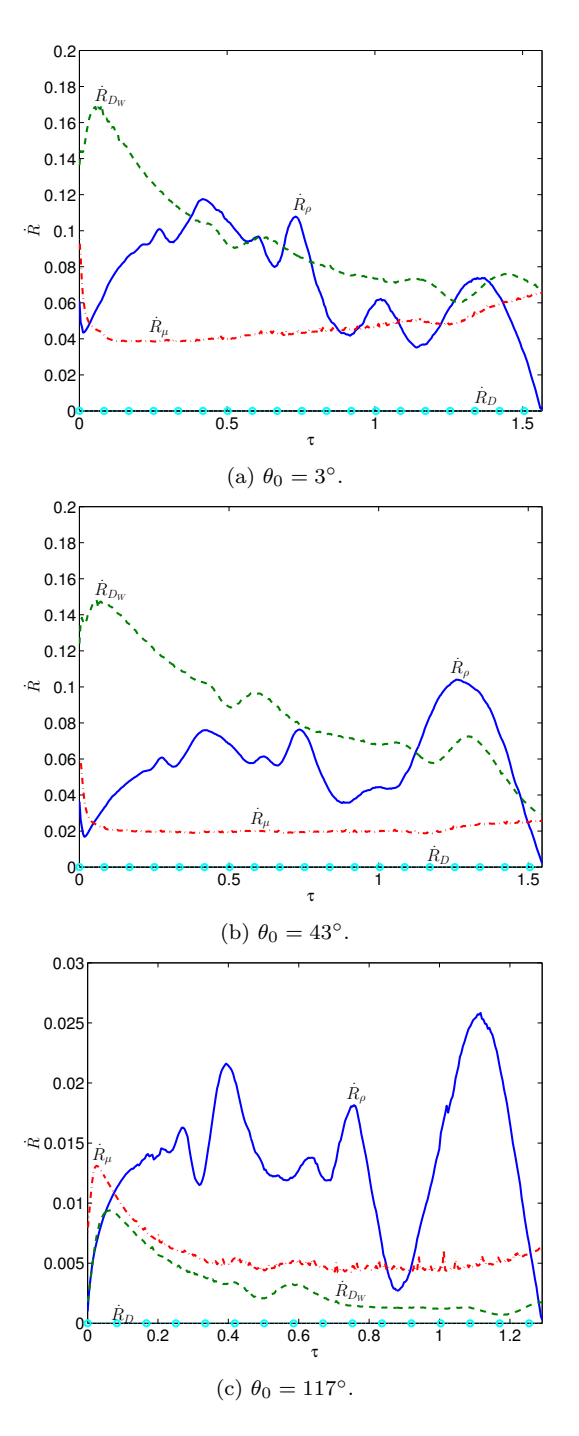


Figure 10: The rate of dissipation in time and the rate of change of kinetic energy at the early stage in the wetting process for a droplet (L=0.78mm) spreading on a solid surface with $\theta_0 = [3^\circ, 43^\circ, 117^\circ]$. The full line corresponds to \dot{R}_ρ , dashed line \dot{R}_{DW} , dashed dotted line \dot{R}_μ and the dashed line with round markers to \dot{R}_D .

time. The transition time for $\theta_0 = 117^{\circ}$ is very short, possibly within the viscous cusp region, where viscosity dominates. The latter is supported by the numerical result, presented in fig. 10c.

5. Conclusion

A phase field modeling approach for rapid dynamic wetting is presented, where the dissipative mechanisms that dictate the evolution are identified. It is shown that it is crucial that the mathematical modeling accounts for non-equilibrium effects at the contact line. In particular we demonstrate that a contact line model assuming local equilibrium will be deficient. A coefficient that appears in the non-equilibrium boundary condition is interpreted as allowing for a diffusive reorganization at the contact line. This coefficient thus represents the molecular processes of the contact line, and parameterizes their influence on the macroscopic spreading rate. At the present time, we could only get the order of magnitude of this coefficient from independent experimental data.

Rapid spontaneous spreading of liquid droplets on solid surfaces with different degrees of wettability was studied numerically. A direct match with the temporal evolution of the experimental spreading radius by Bird et al. (2008) was obtained. Good agreement was also found between the numerical and experimental apparent dynamic contact angle in time. The results presented here were found not to depend significantly on the bulk diffusion or interface width. As a consequence, meaningful simulation results can be obtained by using interface widths that are much larger than what can be physically motivated.

By tracing the rate of dissipation and the rate of change of the kinetic energy we found a new wetting regime, where the dissipation from the contact line relaxation dominates. This is to our knowledge the first time this dissipative mechanism is found to dominate a dynamic wetting process. This serves as a new wetting regime complementing the regimes previously reported in the literature. The three wetting regimes predicted from hydrodynamic theory (Biance et al. (2004), Bird et al. (2008), Eggers et al. (1999)) were also identified in the simulations. A reasonably good match was found for the time of transition from inertial to viscously dominated wetting between the simulations and the theory proposed by Biance et al. (2004).

Finally, a spreading law for the relaxation regime was derived based on a balance between the capillary force and the contact line friction. This along with the spreading law for inertially dominated wetting (Biance *et al.* (2004)) yields as a distinct criterion for the transition between wetting dominated by contact line relaxation and inertia. The transitional times found in the simulations are in good agreement with the theoretical predictions.

Acknowledgment

Funding from the Swedish Research council (VR) through the Linnè Flow Center is acknowledge.

References

- Aarts, D. G. A. L., Lekkerkerker, H. N. W., Guo, H., Wegdam, G. H. & Bonn, D. 2005 Hydrodynamics of droplet coalescence. *Physical Review Letters* **95** (16), 164503.
- Amberg, G., Tonhardt, R. & Winkler, C. 1999 Finite element simulations using symbolic computing. *Mathematics and Computers in Simulation* **49** (4-5), 257–274.
- BIANCE, A. L., CLANET, C. & QUERE, D. 2004 First steps in the spreading of a liquid droplet. *Physical Review E* **69** (1).
- BIRD, J. C., MANDRE, S. & STONE, H. A. 2008 Short-time dynamics of partial wetting. *Physical Review Letters* **100** (23), 234501.
- Blake, T. D. 2006 The physics of moving wetting lines. *Journal of Colloid and Interface Science* **299**, 1–13.
- Blake, T. D. & Haynes, J. M. 1969 Kinetics of liquid/liquid displacement. *Journal of Colloid and Interface Science* **30** (3), 421–423.
- BLAKE, T. D. & SHIKHMURZAEV, Y. D. 2002 Dynamic wetting by liquids of different viscosity. *Journal of Colloid and Interface Science* **253** (1), 196–202.
- Bonn, D., Eggers, J., Indekeu, J., Meunier, J. & Rolley, E. 2009 Wetting and spreading. *Reviews of Modern Physics* 81 (2), 739–805.
- BRIANT, A. J. & YEOMANS, J. M. 2004 Lattice boltzmann simulations of contact line motion. ii. binary fluids. *Physical Review E* **69** (3).
- Cahn, John W. & Hilliard, John E. 1958 Free energy of a nonuniform system. i. interfacial free energy. *The Journal of Chemical Physics* **28** (2), 258–267.
- Carlson, A., Do-Quang, M. & Amberg, G. 2009 Modeling of dynamic wetting far from equilibrium. *Physics of Fluids* **21** (12), 121701–4.
- CARLSON, A., DO-QUANG, M. & AMBERG, G. 2010 Droplet dynamics in a bifurcating channel. *International Journal of Multiphase Flow* 36 5, 397–405.
- Courbin, L., Bird, J. C. & Stone, H. A. 2009 Dynamics of wetting: From inertial spreading to viscous imbibtion. to appear in Journal of Physics-Condensed Matter .
- Cox, R. G. 1986 The dynamics of the spreading of liquids on a solid surface. part 1. visocus flow. *Journal of Fluid Mechanics* **168**, 169–194.
- DE CONINCK, J., DE RUIJTER, M. J. & VOUE, M. 2001 Dynamics of wetting. Current Opinion in Colloid and Interface Science 6 (1), 49–53.
- DING, H. & SPELT, P. D. M. 2007 Wetting condition in diffuse interface simulations of contact line motion. *Physical Review E* 75 (4), 046708.
- Do-Quang, M. & Amberg, G. 2009 The splash of a solid sphere impacting on a liquid surface: Numerical simulation of the influence of wetting. *Physics of Fluids* **21** (2).

- DO-QUANG, M., VILLANUEVA, W., SINGER-LOGINOVA, I. & AMBERG, G. 2007 Parallel adaptive computation of some time-dependent materials-related microstructural problems. Bulletin of the Polish Academy of Sciences-Technical Sciences 55 (2), 229–237.
- Drelich, J. & Chibowska, D. 2005 Spreading kinetics of water drops on self-assembled monolayers of thiols: Significance of inertial effects. *Langmuir* 21 (17), 7733–7738.
- EGGERS, J. & EVANS, R. 2004 Comment on "dynamic wetting by liquids of different viscosity," by t.d. blake and y.d. shikhmurzaev. *Journal of Colloid and Interface Science* **280** (2), 537–538.
- EGGERS, J., LISTER, J. R. & STONE, H. A. 1999 Coalescence of liquid drops. *Journal of Fluid Mechanics* **401**, 293–310.
- DE GENNES, P. G. 1985 Wetting statics and dynamics. Review of Modern Physics 57 (3), 827–863.
- GLASSTONE, S., LAIDLER, K. J. & EYRING, H. J. 1941 The theory of rate processes. McGraw-Hill.
- Guermond, J. L. & Quartapelle, L. 2000 A projection fem for variable density incompressible flows. *Journal of Computational Physics* **165** (1), 167–188.
- HOFFMAN, R. L. 1975 A study of the advancing interface. i. interface shape in liquid—gas systems. *Journal of Colloid and Interface Science* **50** (2), 228 241.
- Huh, C. & Scriven, L. E. 1971 Hydrodynamic model of steady movement of a solid/liquid/fluid contact line. *Journal of Colloid and Interface Science* 35 (1), 85–101.
- JACQMIN, D. 1999 Calculation of two-phase navier-stokes flows using phase-field modeling. *Journal of Computational Physics* **155** (1), 96–127.
- JACQMIN, D. 2000 Contact-line dynamics of a diffuse fluid interface. Journal of Fluid Mechanics 402, 57–88.
- MATSUMOTO, S., MARUYAMA, S. & SARUWATARI, H. 1995 A molecular dynamics simulation of a liquid droplet on a solid surface. *ASME/JSME Therm. Eng. Conf.* **2** (557).
- NGAN, C. G. & DUSSAN, V. E. 1982 On the nature of the dynamic contact angle: an experimental study. *Journal of Fluid Mechanics Digital Archive* 118 (-1), 27–40.
- Petrov, P. G. & Petrov, J. G. 1992 A combined molecular-hydrodynamic approach to wetting kinetics. *Langmuir* 8 (7), 1762–1767.
- QIAN, B., LOUREIRO, M., GAGNON, D. A., TRIPATHI, A. & BREUER, K. S. 2009a Micron-scale droplet deposition on a hydrophobic surface using a retreating syringe. *Physical Review Letters* 102 (16).
- QIAN, T. Z., WANG, X. P. & SHENG, P. 2003 Molecular scale contact line hydrodynamics of immiscible flows. *Physical Review E* **68** (1).
- QIAN, T. Z., WANG, X. P. & SHENG, P. 2004 Power-law slip profile of the moving contact line in two-phase immiscible flows. *Physical Review Letters* **93** (9).
- QIAN, T. Z., WANG, X. P. & SHENG, P. 2006a Molecular hydrodynamics of the moving contact line in two-phase immiscible flows. Communication in Computational Physics 1 (1), 1–52.
- QIAN, T. Z., WANG, X. P. & SHENG, P. 2006b A variational approach to moving contact line hydrodynamics. *Journal of Fluid Mechanics* **564**, 333–360.
- QIAN, T. Z., WU, C. M., LEI, S. L., WANG, X. P. & SHENG, P. 2009b Modeling

- and simulations for molecular scale hydrodynamics of the moving contact line in immiscible two-phase flows. *Journal of Physics-Condensed Matter* **21** (46), 464119.
- REN, W. & E, W. 2007 Boundary conditions for the moving contact line problem. *Physics of Fluids* **19** (2).
- DE RUIJTER, M. J., DE CONINCK, J. & OSHANIN, G. 1999 Droplet spreading: Partial wetting regime revisited. *Langmuir* **15** (6), 2209–2216.
- Saiz, E. & Tomsia, A. P. 2004 Atomic dynamics and marangoni films during liquidmetal spreading. *Nature of Materials* **3** (12), 903–909.
- Seveno, D., Vaillant, A., Rioboo, R., Adao, H., Conti, J. & De Coninck, J. 2009 Dynamics of wetting revisited. *Langmuir* **25** (22), 13034–13044.
- SHIKHMURZAEV, Y. D. & BLAKE, T. D. 2004 Response to the comment on [J. Colloid Interface Sci. 253 (2002) 196] by J. Eggers & R. Evans. *Journal of Colloid and Interface Science* 280 (2), 539–541.
- Tanner, L. H. 1979 The spreading of silicone oil drops on horizontal surfaces. *Journal of Physics D* 12, 1473–1484.
- VILLANUEVA, W. & Amberg, G. 2006 Some generic capillary-driven flows. *International Journal of Multiphase Flow* **32** (9), 1072–1086.
- Voinov, O. V. 1976 Hydrodynamics of wetting. *Izvestiya Akademii Nauk SSSP*, Makhanika Zhidkosti i Gaza 5 (76–84).
- WANG, X. P. & WANG, Y. G. 2007 The sharp interface limit of a phase field model for moving contact line problem. Methods of applications and analysis 14 (3), 287–294.
- Wang, X. P., Qian, T. Z. & Sheng, P. 2008 Moving contact line on chemically patterned surfaces. *Journal of Fluid Mechanics* **605**, 59–78.
- YUE, P., ZHOU, C. & FENG, J. J. 2010 Sharp-interface limit of the Cahn-Hilliard model for moving contact lines. *Journal of Fluid Mechanics* **645** (1), 279 294.

Paper 4

Contact line dissipation in short–time dynamic wetting

By Andreas Carlson, Gabriele Bellani and Gustav Amberg

Linné FLOW Centre, Department of Mechanics, The Royal Institute of Technology, 100 44 Stockholm, Sweden.

EPL 97, 44004-1-6, 2012.

Dynamic wetting of a solid surface is a process that is ubiquitous in nature, and also of increasing technological importance. The underlying dissipative mechanisms are however still unclear. We present here short-time dynamic wetting experiments and numerical simulations, based on a phase field approach, of a droplet on a dry solid surface, where direct comparison of the two allows us to evaluate the different contributions from the numerics. We find that an important part of the dissipation may arise from a friction related to the motion of the contact line itself, and that this may be dominating both inertia and viscous friction in the flow adjacent to the contact line. A contact line friction factor appears in the theoretical formulation that can be distinguished and quantified, also in room temperature where other sources of dissipation are present. Water and glycerin-water mixtures on various surfaces have been investigated where we show the dependency of the friction factor on the nature of the surface, and the viscosity of the liquid.

1. Introduction

A canonical example of dynamic wetting is the time dependent spreading of a liquid droplet on a dry substrate. The droplet spreads by motion of the contact line, i.e. the curve where the liquid-gas interface that constitutes the droplet surface intersects the solid substrate. Contact lines are present in a myriad of flow phenomena in Nature and in industrial applications, such as the formation of coffee stains, water uptake of birds, droplet deposition in biomedical applications, etc. Wetting is also utilized in technology, for example in microfluidic systems, sintering and in immersion lithography techniques. Dynamic wetting has however been difficult to describe theoretically and to model computationally, primarily due to the inherent coupling between molecular and macroscopic length scales. In the immediate vicinity of the contact line microscopic interactions can be important for the dynamic contact angle (Ren & E (2007)) while the bulk viscosity is known to influence spreading dynamics on the macro-scale (Tanner (1979)).

In addition to these different mechanisms, inertia has also been proposed to characterize certain wetting phenomena (Biance et al. (2004), Bird et al. (2008)). Bird et al. (2008)) demonstrated that a set of experimental spreading data for water on solid surfaces with different wettability collapsed if the drop radius was changed. The slope of the spreading curves did however change with the wettability. We have recently shown (Carlson et al. (2012)) that neither an inertial or viscous scaling law can describe our experimental spreading data for a wide range of viscosities (1-85mPas). Instead, the data collapses for a scaling law based on contact line friction factor predicted from the phase field theory, where the slope was found to be the same even if the solid surface wettability was changed. Simulation of such wetting makes it possible to estimate the inertial and contact line friction contribution, allowing a direct comparison of the magnitude of the two. As we will show later here, the latter predicts indeed a larger contribution in simulations.

It is well known (Huh & Scriven (1970)) that continuum hydrodynamic theory cannot give a complete description of the dissipation at the contact line, as it predicts a non-integrable viscous stress at the contact line, if a noslip condition is applied for the liquid flow. Ad hoc models can be generated if the liquid is allowed for instance to slip at the surface (Voinov (1976)), and these are also adequate for predicting the motion of contact lines for flow situations were the dominating dissipation is due to the continuum viscous flow surrounding the contact line. However, there may be parameter ranges where the dominating dissipation mechanism is local to the contact line, and then nanoscale phenomena must somehow be accounted for.

Several different explanations have been proposed for the nanoscale mechanisms at play in dynamic wetting (Bonn et al. (2009)). Blake & Haynes (1969) describe contact line motion as an activated process where molecules are hopping between potential wells at the solid surface. Prevost et al. (1999) used inviscid superfluid helium at cryogenic temperatures (< 2K) in experiments to limit viscous effects at the contact line. They measured the force acting onto the contact line and found that it moved through thermally activated jumps that were related to the roughness of the Cesium substrate. Duvivier et al. (2011) estimated a contact line friction factor for liquids of different viscosity from the molecular kinetic theory Blake & Haynes (1969), by fitting the experimental spreading radius for drops with different viscosity. Ren and E extracted a friction parameter acting at the contact line on the macro (Ren & E (2010)) and micro scale (Ren & E (2007)). Molecular dynamics simulations (Ren & E (2007)) for large capillary numbers (given by the ratio between the viscous and surface tension force) indicated that the contact line might be closer to a diffusive process. In this parameter regime experiments have also shown that classical theory fails to describe the results (Chen et al. (1995)). Eggers (2004) examined theoretically contact line motion at large capillary numbers and pointed out that the interaction between the large scale and the local dynamics near the contact line still holds great challenges.

2. Theory

In spite of the extensive studies of wetting physics, direct measurements of the dissipation in macroscopic wetting has been elusive in both experiments and simulations. Our primary aim here is to quantify the importance of a contact line friction force, and to obtain values for the corresponding friction coefficient. To this end we have conducted droplet spreading experiments, with water-glycerin mixtures with a wide range of viscosities (1-85mPas), on solid surfaces with different wetting properties. To analyze these experiments, corresponding axis-symmetric numerical simulations based on the Navier-Stokes Cahn-Hilliard equations (Jacqmin (1999)) have been made, assuming that thermodynamics of the experimental system is described by the postulated free energy. The simulated results allow us to identify the different contributions to the dissipation, which are needed to reproduce the experimental results.

The Navier-Stokes equations take the form,

$$\rho \frac{D\mathbf{u}}{Dt} = -\nabla P + \nabla \cdot \left(\mu (\nabla \mathbf{u} + \nabla^T \mathbf{u}) \right) + \phi \nabla C - \rho g \cdot \mathbf{n}_z \text{ in } \Omega$$
 (1)

$$\nabla \cdot \mathbf{u} = 0 \text{ in } \Omega \tag{2}$$

D/Dt is the total derivative, Ω denotes in the total volume, while Γ denotes the boundary. $\phi = \frac{\delta F}{\delta C}$ is the chemical potential, where F is the free energy and C the concentration taking the value C=1 in the liquid phase and C=-1 in the gas phase. $\rho = \frac{1}{2}\left(\rho_g(1-C) + \rho_l(1+C)\right)$ and $\mu = \frac{1}{2}\left(\mu_g(1-C) + \mu_l(1+C)\right)$ are representing the density and the viscosity, respectively, as a function of the concentration. The subscript l denotes the liquid phase and the subscript l the gas phase. l = l

The Cahn-Hilliard equation (Cahn & Hilliard (1958), Jacqmin (1999)) is based on a formulation of the free energy in the system,

$$\frac{DC}{Dt} = \nabla \cdot \left(M \nabla \phi \right) \right) = \nabla \cdot \left(M \nabla \left(\frac{\sigma}{\epsilon} \Psi'(C) - \epsilon \sigma \nabla^2 C \right) \right) \text{ in } \Omega$$
 (3)

and can be used together with the Navier-Stokes equations to model contact line motion. $M=8\cdot 10^{-11}m^4/(Ns)$ is a Cahn-Hilliard mobility. The free energy of the system is given by a volume and a solid surface contribution, $F=\int \left(\frac{\sigma}{\epsilon}\Psi(C)+\frac{\sigma\epsilon}{2}|\nabla C|^2\right)d\Omega+\int \left((\sigma_{sl}-\sigma_{sg})g(C)+\sigma_{sg}\right)d\Gamma$. The volumetric free energy consists of two terms representing the bulk $\left(\frac{\sigma}{\epsilon}\Psi(C)\right)$ and interfacial energy $\left(\frac{\sigma\epsilon}{2}|\nabla C|^2\right)$, respectively. $\Psi=\frac{1}{4}(C^2-1)^2$ is a double-well function with two minima, being the equilibrium concentrations (C) of gas and liquid. ϵ is the diffuse interface width and σ is the surface tension coefficient. On the solid surface, the energy is given by either having a wet (σ_{sl}) or dry (σ_{sg}) solid surface, where $g(C)=\frac{1}{4}(2+3C-C^3)$ is allowing for a change in surface energy with respect to the concentration.

By making a variation $\delta F/\delta C$ in the free energy with respect to the concentration, we obtain an expression for the chemical potential. Another outcome

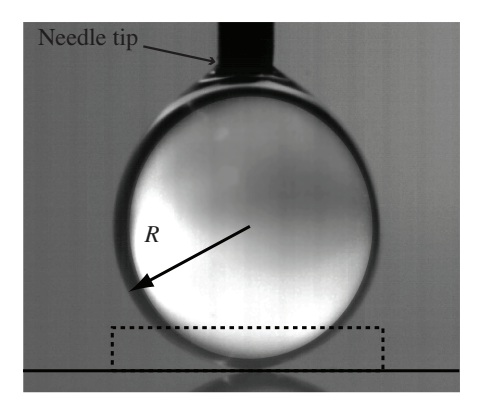


Figure 1: Initial condition taken from the experiments. The mirrored image comes from the reflection from the Si-wafer and the fully drawn line illustrates the solid substrate. R defines the droplet radius and the dashed line the field of view in the experiments.

from the variational procedure is a general wetting boundary condition, formulated from phenomenological thermodynamics. This boundary condition for the concentration on the solid surface, has been demonstrated to indeed capture the main features in macroscopic rapid dynamic wetting (Carlson *et al.* (2011), Carlson *et al.* (2009))

$$\epsilon \mu_f \frac{\partial C}{\partial t} = -\epsilon \sigma \nabla C \cdot \mathbf{n} + \sigma \cos(\theta_e) g'(C). \tag{4}$$

 μ_f is here interpreted as a friction factor at the contact line and θ_e is the equilibrium contact angle. Since a no-slip condition is given for the velocities at the solid surfaces, the contact line moves by interfacial diffusion, overcoming the difficulty that arises at the contact line in classical hydrodynamic theory. The predicted flow at the contact line is also different than the solution from classical theory, as interfacial diffusion allows flow lines to pass through the interface (Seppecher (1996), Yue *et al.* (2010)) a process interpreted by Pomeau (2011) in terms of phase change.

The primary input in the axis-symmetric simulations are given directly from the experiment, meaning that the measured value for density, dynamic viscosity, equilibrium contact angle and surface tension are applied. For the sake of direct comparison between the experiments and simulations, the interface width is chosen to be the same as the pixel size in the experiments ϵ =7.5 μ m. In Carlson et al. (2011) the sensitivity of both ϵ and M was investigated, by varying both about one order of magnitude, the results remained unchanged and no significant increase in viscous dissipation was observed.

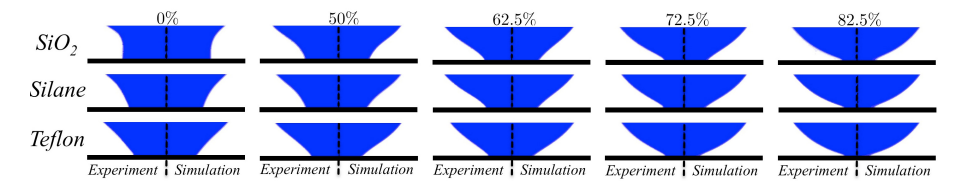


Figure 2: Direct comparison of experimental results and numerical simulations for five droplets with an initial radius $R = (0.5 \pm 0.02)mm$ and 0, 50, 62.5, 72.5, 82.5% glycerin mass fraction (from left to right), spreading on SiO_2 , Silane and Teflon (from top to bottom) at time 0.33ms after start of spreading. Each panel shows a composite of experiment and simulation, where the left half is the experimental picture and the right half the numerical prediction.

A set of droplet spreading experiments have been performed with high-speed imaging at 150k fps (128 × 48 pixels), on Si-wafers coated with: oxide layer, teflon (Teflon AF 1600, DuPont, USA) and silane (trimethyl(vinyl)silane). The surfaces where prepared with a standard silanization process (de Gennes et al. (2003)). Droplets were made of glycerin-water mixtures, with five different mass fractions (0 to 85%) of glycerin. Viscosity was measured before and after the experiments with a commercial viscometer, and the measurements were found to be in good agreement with values reported in literature (Dorsey (1940)). Surface tension was measured by a pendant drop technique. The measured values for viscosity and surface tension are given in table 1. Droplets were generated at the tip of a needle by a syringe-micro-pump

% glycerin	0%	50%	62.5%	72.5%	82.5%
$\mu \pm 0.2 \text{ [mPas]}$	1	6.6	14	31	85
$\sigma \pm 0.2 \; [\mathrm{mN/m}]$	73	66	66	65	64

Table 1: Measured values of the dynamic viscosity (μ) and surface tension coefficient (σ) for the different mixtures of water and glycerin. The upper row shows the mass fraction of glycerin in water.

system, which allowed to control the volume rate. The nominal droplet size was controlled by vertically adjusting the distance from the needle tip to the solid surface (see fig. (1)) using a micrometer screw, although the actual size of the droplet was measured more accurately from the digital images.

The contact line friction factor (μ_f) that appears in eq. 4 is determined by matching the experimental spreading radii in simulations. A non-zero μ_f generates an additional dissipation that slows the relaxation of the contact line to its equilibrium state. It allows us to parametrize on a macroscopic level what is believed to be microscopic effects that generates dissipation at the contact line. After numerically measuring the value of μ_f we compare directly the evolution of the dynamic contact angle (θ) in the experiment and simulation. Since no external force is applied on the system, the uncompensated Young's force $(F = 2\pi r \sigma(\cos(\theta_e) - \cos(\theta)))$ is believed to be the leading mechanism driving the spreading, thus the rate of change of work done by this force to advance the contact line $\dot{W} = u_{cl}F = 2\pi r u_{cl}\sigma(\cos(\theta_e) - \cos(\theta))$ is also directly compared between experiments and simulations, where r is the spreading radius and u_{cl} is the contact line speed.

We next proceed to formulate the different contributions to the dissipation rate for a drop spreading on a substrate (Ren & E (2011)). Based on the governing equations three dissipation contributions appear, namely; viscous dissipation (R_{μ}) , contact line dissipation (R_f) and a diffusive dissipation,

$$\dot{R}_{\mu} = \int \frac{\mu}{2} (\nabla^T \mathbf{u} + \nabla \mathbf{u}) : (\nabla^T \mathbf{u} + \nabla \mathbf{u}) d\Omega$$
 (5)

$$\dot{R}_f = \int \epsilon \mu_f \frac{\partial C}{\partial t}^2 d\Gamma. \tag{6}$$

For clarity we have discarded the diffusive dissipation here $(\dot{R}_M = \int 1/M(\partial\phi/\partial t)^2 d\Omega)$, as it is found to give a very small contribution. Since inertia has been proposed as a mechanism to govern spontaneous capillary driven spreading, we also extract the rate of change of kinetic energy (\dot{R}_{ρ}) to compare its magnitude with viscous and contact line dissipation,

$$\dot{R}_{\rho} = \int \frac{\partial(\frac{1}{2}\rho u^2)}{\partial t} d\Omega. \tag{7}$$

As formulated by de Gennes (1985), among others (de Ruijter et al. (1999), Duvivier et al. (2011), Prevost et al. (1999)), there can be a dissipation ($\dot{R}_{DG} = 2\pi r \mu_f u_{cl}^2$) at the contact line itself, given as a function of the contact line speed and a friction factor μ_f . This is in fact the same form as \dot{R}_f in eq. 6, which is formulated from the boundary condition in eq. 4. In order to see this we estimated \dot{R}_f as $\dot{R}_f = \int_{\Gamma} \epsilon \mu_f \frac{\partial C}{\partial t}^2 d\Gamma \sim 2\pi r \epsilon \mu_f (\frac{\delta C}{\delta r})^2 (\frac{\partial r}{\partial t})^2 \epsilon \sim 2\pi r \mu_f u_{cl}^2$. Note that the variation in concentration at the solid surface with respect to the radial direction is $\delta C/\delta r \sim 1/\epsilon$.

3. Dissipation in dynamic wetting

Fig. 2 shows a direct comparison of experimental results and numerical simulations for five droplets with different viscosities on SiO_2 , Silane and Teflon (from top to bottom, respectively), at time t=0.4ms. The initial condition and the field of view for the experiments is shown in fig. 1. Here the initial radius is $R \sim 0.5$ mm. In the simulations, the friction parameter μ_f acting at the contact line, which is unknown a priori, is measured by matching the spreading radius in time with the experiments. In fact, if μ_f is set to zero, the equilibrium contact angle is enforced at the solid surface and the contact line propagates faster in the simulations than what is observed in the experiments.

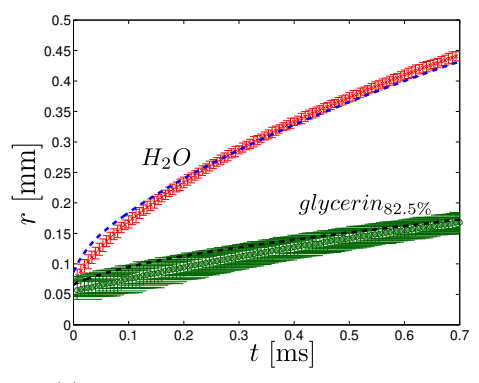
But when the appropriate value for μ_f is introduced, the contact line relaxation is impeded and the simulations match measured parameters from experiment like the spreading radius and apparent dynamic contact angle. Notice that by adjusting this single parameter μ_f the simulations capture the complete droplet dynamics as it spread in time.

As the droplets start to wet the solid surfaces, see fig. 2, the interface forms an apparent contact angle that is much larger than the static equilibrium value. For the spreading of a water droplet, a capillary wave is formed at the contact line at the start of spreading. This wave propagates across the drop, before it is finally dissipated (Carlson et al. (2011), Bird et al. (2008)). Contrary to water, experimental observations of the more viscous fluids does not show any capillary waves, which are immediately damped by viscosity. Still, the apparent contact angle is very different from its static value.

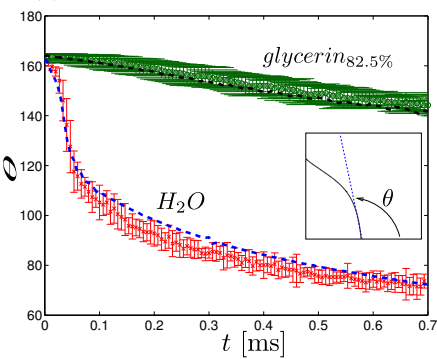
In fig. 3 the measured spreading radius, dynamic contact angle and uncompensated young's force are presented. The errorbars represent the maximum deviation between several realizations of the same experiment, using a minimum of four realizations. Fig. 3a shows the evolution of the spreading radius and fig. 3b the dynamic contact angle (θ) as functions of time for the spreading of water and $glycerin_{82.5\%}$ droplets presented in the first row to the far left and right in fig. 2. The inset in fig. 3b illustrates how the dynamic contact angle has been defined in the experiments and the simulations. The contact angle was measured by computing the tangent over the first seven pixels of the interface contours neglecting the first pixel. Thus the tangent was computed from the remaining six points using the least square method, which showed consistent results for different interpolation heights as long as it is less than the local radius of curvature at the contact line.

As can be seen from fig. 3a, the evolution of the droplet radius is very different for the two cases, with about a factor of two larger speed for the water droplet. The greatest difference can however be observed in the evolution of the contact angle in fig. 3b. For the water droplet, the contact angle evolves in a highly non-linear fashion, while in the latter the contact angle relaxes approximately linearly in time. In both cases a friction factor μ_f of considerable size is found to be needed in order to obtain the proper wetting dynamics. For the water droplet a friction factor $(\mu_f)_{H_2O} = 0.15 Pas$ is found. For the very viscous glycerin-water droplet $(\mu_f)_{glycerin_{82.5\%}} = 1.02 Pas$.

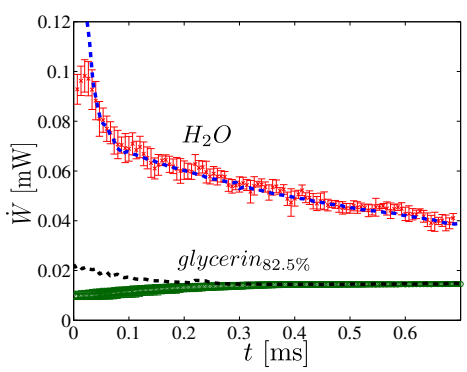
One of the driving forces in the spreading dynamics believed to be the uncompensated Young's force (F), by having a dynamic angle which is different from the angle at equilibrium state. In fig. 3c, we compare the rate of work done $(\dot{W}=u_{cl}F)$ by this force between experiments and simulations, as the contact line advances across the solid substrate. Since the contact line velocity and the contact angle relaxation (see fig. 3a, b) evolves much faster for water than for the glycerin mixture, \dot{W} is higher for water as observed in fig. 3c. \dot{W} slowly decreases in time during the spreading of the $glycerin_{82.5\%}$ droplet.



(a) Droplet radius as function of time.



(b) The apparent dynamic contact angle θ as function of time. θ has been extracted by using the same methodology in the experiments and in the simulations.



(c) The rate of change of work due to he uncompensated Young's stress, $\dot{W} = 2\pi r u_{cl} \sigma(\cos(\theta_e) - \cos(\theta))$.

Figure 3: a) Droplet radius, b) dynamic contact angle and c) the rate of change of work due to the uncompensated Young's stress as functions of time for a pure water and an 82.5% glycerin-water droplet. The dashed curves are simulations and the points with error bars are experimental. The contact line speed u_{cl} is determined by taking the derivative of the mean spreading radius in a).

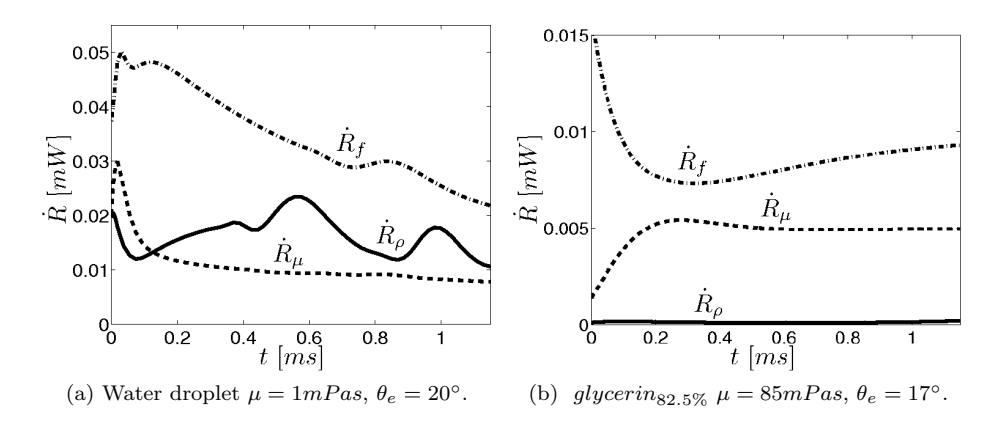


Figure 4: The different contributions to the dissipation from the simulations, viscous \dot{R}_{μ} (dashed lines), contact line \dot{R}_{f} dissipation (dashed-dotted lines) and rate of change of kinetic energy \dot{R}_{ρ} (full lines).

Having obtained a very good match between simulations and experiments, as shown in fig 3, we will now assume that also the dissipation mechanisms are the same in simulations and experiments. Thus, we will now evaluate the different contributions to the dissipation rate from the simulations, and claim that they reflect the dissipation rates in the corresponding experiments. Fig. 4 shows a comparison between the dissipation rates \dot{R}_f and \dot{R}_μ , extracted from the simulations as the water (fig. 4a) and $glycerin_{82.5\%}$ (fig. 4b) droplet spreads in time. Since it has been argued that inertia has a dominant role in such spreading, we also compare the magnitude of the rate of change of kinetic energy (\dot{R}_ρ) . The dashed line shows the viscous dissipation (\dot{R}_μ) , the dotted line the contact line dissipation (\dot{R}_f) and the full line the rate of change of kinetic energy (\dot{R}_ρ) .

Fig. 4a shows the dissipation as the water droplet spreads on an oxidized Si-wafer. At the incipience of wetting the contact line forms a small cusp region with a large curvature, and the contact line accelerates from a zero-velocity condition explaining the increase in dissipation at the very early stage of the spreading. It is also at the early stage of the spreading that the viscous dissipation is the largest but the spreading dynamics is dominated by contact line dissipation, which is here about five times larger than the viscous dissipation. Also the rate of change of kinetic energy is producing a similar contribution as the two dissipations, but it is found to give a smaller contribution than the contact line friction. Rapid spreading of water shows capillary waves traveling across the droplet (Biance et al. (2004), Bird et al. (2008)), which are causing the wavy form of the change in kinetic energy in time observed here. After a

peak in both the viscous and contact line dissipation around time $t = 50\mu s$, they slowly decreases as the contact line decelerates in time.

Also the dissipation in the spreading of the glycerin_{82.5%} droplet was found to be dominated by contact line dissipation, see fig. 4b. At the start of spreading the contact line dissipation is large, but rapidly decreases and levels off around $t=20\mu s$. In the same timeframe viscous dissipation slowly increases, before it becomes fairly constant. Contact line dissipation is found to be a significant and dominant contribution in the spreading of droplets for both low and high viscosity. At a much later time, when the capillary number is small ($\ll 0.1$) and the droplet has a spherical cap profile, viscous dissipation is expected to dominate the spreading thus recovering Tanner's law (Bonn et al. (2009)). For this viscous liquid, the rate of change of kinetic energy is much smaller than the viscous and contact line dissipation, also illustrating why no capillary wave is observed as it is immediately damped by the viscosity.

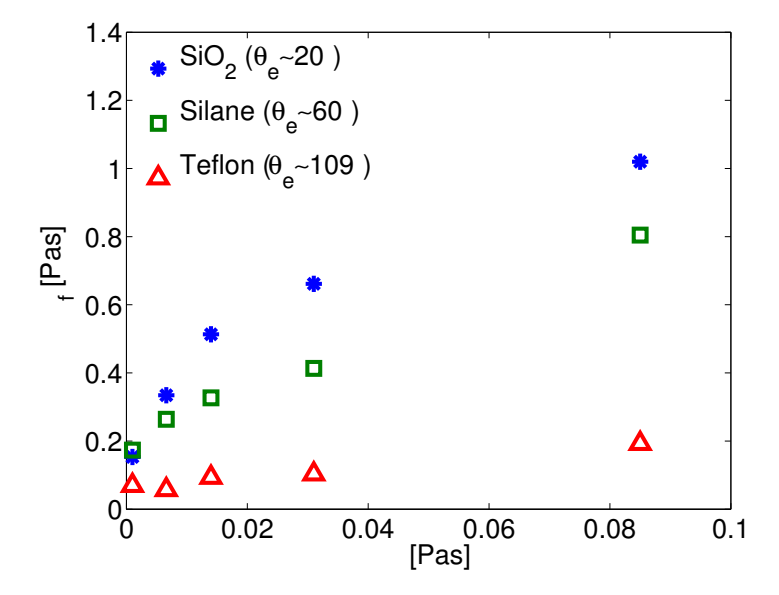


Figure 5: Measured contact line friction μ_f as a function of the dynamic viscosity μ on the Si-wafers coated with oxide (circles), silane (squares) and teflon (triangles). Water has an equilibrium contact angle of about $[20^\circ, 60^\circ, 109^\circ]$ for these coatings, respectively. Variation in the equilibrium contact angle for the different mixtures is small $\Delta\theta_e \sim \pm 2^\circ$.

The experiments of different water-glycerin mixtures have been performed on Si-wafers coated with oxide, silane and teflon. In fig. 5 we show the measured contact line friction parameter as a function of the dynamic viscosity of the mixtures, for the three surfaces. We notice that all of the reported values for the contact line friction factor are much larger than the dynamic viscosity. Based on the macroscopic simulations it is hard to make a conclusive argument about the microscopic origin of μ_f , it has previously been interpreted as an hysteresis effect (Prevost *et al.* (1999)) and molecular hopping (de Ruijter *et al.* (1999)) at the contact line.

The further the droplet is from its equilibrium condition as it starts to spread, the more important contact line friction is in the flow. In the spreading phenomena investigated here the contact angle is initially large, $\sim 180^{\circ}$, as the droplets start to wet. This explains why the friction factor becomes larger for surfaces that wet well. The friction factor increases with respect to the viscosity on all of the solid surfaces.

4. Conclusions

Our measurements identify contact line dissipation as an essential part in dynamic wetting. The excellent agreement between experiments and simulations indicates that the dissipation is the same in the two. This enables us to distinguish the different dissipation rates in simulations. They show that contact line dissipation is a significant and dominant contribution that can not be disregarded at the early stage of the spreading process. A friction factor appears (μ_f) at the contact line, which generates the dissipation as the contact line moves. This contact line friction factor is believed to parametrize the microscopic interactions at the contact line on the macro-scale. It has been directly measured from simulations by a direct comparison of experiments for a range of viscosities and equilibrium contact angles. These results help us to quantify an important underlying physical mechanism that governs rapid dynamic wetting, which has been largely unknown. This is in particular relevant for the strategic design of application at small scales, such as microfluidic devices, where moving contact lines are an inherent part.

We would like to thank F. Carlborg, M. Do-Quang, A. Oko and F. Lundell for technical support and stimulating discussions. Thank to H. A. Stone for pointing out an inconsistency in our analysis in an earlier version of this article. The authors acknowledge funding from the Swedish Research Council, through the Linné Flow Center.

References

- BIANCE, A. L., CLANET, C. & QUÉRÉ, D. 2004 First steps in the spreading of a liquid droplet. *Physical Review E*, **69** (1), 016301-1–4.
- BIRD, J. C., MANDRE, S. & STONE, H. A. 2008 Short-time dynamics of partial wetting. *Physical Review Letters*, **100** (23):234501.
- Blake, T. D. & Haynes, J. M. 1969 Kinetics of liquid/liquid displacement. *Journal of Colloid and Interface Sciences*, **30** (3):421–423.

- Bonn, D., Eggers, J., Indekeu, J., Meunier, J. & Rolley, E. 2009 Wetting and spreading. *Review Modern Phys.*, **81** (2):739–805.
- CAHN, J. W. & HILLIARD, J. E. 1958 Free energy of a nonuniform system. i. interfacial free energy. The Journal of Chemical Physics, 28 (2):258–267.
- Carlson, A., Do-Quang, M. & Amberg, G. 2009 Modeling of dynamic wetting far from equilibrium. *Physics of Fluids*, **21** (12):121701–4, 12.
- Carlson, A., Do-Quang, M. & Amberg, G. 2011 Dissipation in rapid wetting. Journal of Fluid Mechanics, 682: 213–240.
- Carlson, A., Bellani, G. & Amberg, G. 2012 Universality in dynamic wetting dominated by contact line friction. Submitted for publication, arXiv:1111.1214v1.
- CHEN, Q., RAME, E. & GAROFF, S. 1995 The breakdown of asymptotic hydrodynamic models of liquid spreading at increasing capillary number. *Physics of Fluids*, 7 (11):2631–2639.
- Dorsey, N. E.. 1940 Properties of ordinary water-substance. News Edition, American Chemical Society, 18 (5):215.
- Duvivier, D., Seveno, D., Blake, T.D., Rioboo, R. & De Coninck, J. 2011 Experimental evidence of the role of viscosity in the molecular kinetic theory of dynamic wetting. *Langmuir*, **27**:13015–13021.
- EGGERS, J. 2004 Toward a description of contact line motion at higher capillary numbers. *Physics of Fluids*, **16** (9):3491–3494, 2004.
- DE GENNES, P. G., BROCHARD-WYART, F. & Quéré, D. 2003 Wetting statics and dynamics. Capillarity and Wetting Phenomena., Springer.
- DE GENNES, P. G. 1985 Wetting statics and dynamics. Review of Modern Physics, 57 (3):827–863, 1985.
- Huh, C. & Scriven, L. E. 1971 Hydrodynamic model of steady movement of a solid/liquid/fluid contact line. *Journal of Colloid and Interface Sciences*, 35 (1):85–101.
- JACQMIN, D. 1999 Calculation of two-phase navier-stokes flows using phase-field modeling. Journal of Computational Physics, 155 (1):96–127.
- Prevost, A., Rolley, E. & Guthmann, C. 1999 Thermally activated motion of the contact line of a liquid he-4 meniscus on a cesium substrate. *Physical Review Letters*, **83** (2):348–351.
- Pomeau., Y. 2011 Contact line moving on a solid. European Physics Journal Special Topics, 197, 15–31.
- REN, W. & E, W. 2011 Derivation of continuum models for the moving contact line problem based on thermodynamic principles. *Physics of Fluids*, **22** (10):102103-1–19.
- Ren, W. & E, W. 2007 Boundary conditions for the moving contact line problem. *Physics of Fluids*, **19** (2).
- DE RUIJTER, M. J., BLAKE, T. D. & DE CONINCK, J. 1999 Dynamic Wetting Studied by Molecular Modeling Simulations of Droplet Spreading *Langmuir*, **15** (22), 7836–7847.
- Seppecher, P. 1996 Moving contact line in the Cahn-Hilliard theory. *International Journal of Engineering Science*, **34**, 977.
- Tanner, L. H. 1979 The spreading of silicone oil drops on horizontal surfaces. *Journal of Physics D*, **12**:1473–1484.

- Voinov, O. V. 1976 Hydrodynamics of wetting. Izvestiya Akademii Nauk SSSP, Makhanika Zhidkosti i Gaza, $\bf 5$ (76–84).
- Yue, P., Zhou, C. & Feng, J.J. 2010 Sharp-interface limit of the Cahn-Hilliard model for moving contact lines. *Journal of Fluid Mechanics* **645** (1), 279 294.

5

Paper 5

Universality in dynamic wetting dominated by contact line friction

By Andreas Carlson*, Gabriele Bellani* and Gustav Amberg*

*Linné FLOW Centre, Department of Mechanics, The Royal Institute of Technology, 100 44 Stockholm, Sweden.

submitted to Rapid Communications in Physical Review E, 2012.

We report experiments on the rapid contact line motion present in the early stages of capillary driven spreading of drops on dry solid substrates. The spreading data fails to follow a conventional viscous or inertial scaling. By integrating experiments and simulations, we quantify a contact line friction (μ_f) , which is seen to limit the speed of the rapid dynamic wetting. A scaling based on this contact line friction is shown to yield a universal curve for the evolution of the contact line radius as a function of time, for a range of fluid viscosities, drop sizes and surface wettabilities.

The interest in moving contact lines is increasing due to the need for design of fluid applications at small scales, since these often rely on manipulation or control of two-phase flow. Examples of such are microfluidic systems, sintering, printing, coating and immersion lithography techniques to name a few. Spontaneous spreading occurs in the deposition and formation of micron sized drops in biomedical applications and when rewetting the lubricating film covering the eye.

A generic example of dynamic wetting is the spreading of a spherical liquid drop as it comes in contact with a dry solid surface. Its spreading after contact is dominated by different physical mechanisms at various stages in the temporal evolution. If the drop radius is less than its capillary length, the flow is mainly driven by the interfacial energy of the drop and the substrate surface energy. The contact line is formed at the intersection of the drop liquid-air interface and the solid substrate, where the dynamic contact angle is defined as the angle between the liquid-air interface and the substrate. For a moving contact line, the interface is typically distorted near the solid surface, giving rise to a free surface capillary force, which may pull the contact line forward. These forces are balanced by different rate-limiting processes, such as viscous dissipation (Huh & Scriven (1971)) and inertia (Bird et al. (2008)), which all act to reduce the contact line speed.

It is well known that the classical hydrodynamic theory predicts a divergence of viscous stress at the contact line. Therefore it might be expected that

the spreading is dominated by the viscous dissipation in the bulk. By regularizing the viscous dissipation, a model for the spreading in viscously dominated wetting is established (Voinov (1976)). This is often referred to as Tanner's law where the spreading radius (r) evolves as $r \sim R(\frac{\sigma t}{\mu R})^{\frac{1}{10}}$, where σ is the surface tension coefficient, R the initial drop radius and μ the viscosity. This model, which holds promise if the drop evolves slowly and has a shape similar to a spherical cap, has explained many experiments. However there are many wetting phenomena that it does not describe, illustrating that there are other mechanisms influencing or dominating the spreading.

One example is the spontaneous spreading of a water drop as it comes in contact with a low energy substrate. Experiments indicate here that the acceleration of liquid in the bulk of the drop is resisting contact line motion. An inertial spreading is found to follow $r \sim R \left(\frac{R^3 \rho}{\sigma}\right)^{\frac{1}{4}} \cdot t^{\frac{1}{2}}$ (Biance et al. (2004)) (ρ is the density), but by making the substrate more hydrophobic a different exponent for the spreading radius was found by Bird et al. (2008). The hydrodynamic model cannot fully capture wetting at high capillary numbers (given by the ratio of the viscous and surface tension force) (Chen et al. (1995)), and dynamic wetting experiments of viscous (1Pa s) drops (Bliznyuk et al. (2010)). In the latter case the spreading radius was observed to increase as the square root of time ($r \sim t^{0.5}$).

de Gennes (1985) postulated that there might be another non-hydrodynamic dissipative contribution arising from the contact line itself. This macroscopic dissipation was defined by a friction factor local at the contact line, which has the same units as viscosity. Others (Carlson et al. (2011), Ren & E (2007), Prevost et al. (1999), Ren et al. (2010), Blake & Haynes (1969)) have also discussed the importance of local non-hydrodynamic effects at the contact line, with different interpretations of its microscopic origin. Recently (Duvivier et al. (2011)) a friction factor was estimated from the molecular kinetic theory by fitting the experimental spreading radius for drops with different viscosity. These experimental observations are collected at much later time scales than presented here, and the value for this friction factor is an order of magnitude larger than our numerical measurements.

By integrating experiments and axi-symmetric simulations based on the Cahn-Hilliard Navier Stokes equations (Carlson et al. (2009, 2012)) we estimate values for the friction factor (μ_f) that appears in the free energy formulation. Theoretically, the friction factor generates a local dissipation at the contact line through its boundary condition. Here, particular attention is devoted to the very first stage of a spontaneous spreading process that is far from equilibrium. The experimental data cannot be rationalized as viscous or inertial effects. The data set collapses for a scaling law based on the numerically measured contact line friction parameter μ_f , even for a wide range of viscosities (1-85mPa s), different drop sizes and surface energies. These results indicate that local

dissipation at the contact line, interpreted as a contact line friction, is limiting spreading.

Both experiments and numerical axi-symmetric simulations of drop spreading have been performed. The simulations are based on the Cahn-Hilliard Navier-Stokes equations (Carlson et al. (2009)). In terms of phenomenological thermodynamics one can postulate the free energy (F) for a binary fluid $F = \int \left(\frac{\sigma}{\epsilon}\Psi(C) + \frac{\sigma\epsilon}{2}|\nabla C|^2\right)d\Omega + \int \left((\sigma_{sl} - \sigma_{sg})g(C) + \sigma_{sg}\right)d\Gamma$. The volumetric (Ω) free energy consists of two terms representing the bulk $\left(\frac{\sigma}{\epsilon}\Psi(C)\right)$ and interfacial energy $\left(\frac{\sigma\epsilon}{2}|\nabla C|^2\right)$, respectively. $\Psi = \frac{1}{4}(C^2 - 1)^2$ is a double-well function with two minima, giving the equilibrium values of the order parameter C, as C = -1 for gas and C = 1 liquid. The diffuse interface width (ϵ) is chosen to be the same as the spatial resolution in the experiments $\epsilon = 7.5 \mu m$. Important to note, however, is that in (Carlson et al. (2011)) ϵ has been varied one order of magnitude, without any noticeable change in the results or any increase in viscous dissipation.

The surface energy of the wet substrate is σ_{sl} , and the dry (σ_{sg}) . $g(C) = \frac{1}{4}(2+3C-C^3)$ is chosen to give g(1) = 1 and g(-1) = 0, thus producing the corresponding wet or dry surface energy of the substrate.

By making a variation in F with respect to the concentration, one obtains an expression for the chemical potential $(\delta F/\delta C)$. If accounting for the effects of convection of the concentration, that would equal the flux due to gradients of the chemical potential, the Cahn-Hilliard equation is recovered, which along with the Navier Stokes equations forms a theoretical basis for modeling of wetting (Carlson et al. (2009)) with a no-slip on the wall.

By retaining any perturbation in the concentration at the wall, a general wetting boundary condition for the concentration at the solid surface appears (Jacqmin (2000)),

$$\epsilon \mu_f \frac{\partial C}{\partial t} = -\epsilon \sigma \nabla C \cdot \mathbf{n} + \sigma \cos(\theta_e) g'(C). \tag{1}$$

We interpret here μ_f as a friction factor at the contact line. θ_e is the equilibrium contact angle.

Experiments of spontaneously spreading drops have been carried out through high-speed imaging (150kfps) for different viscosities and coatings (oxide, silane, teflon) on Si-wafers. The viscosity was changed by using different glycerin-water mixtures, of glycerin mass-fraction 0%, 50%, 65%, 72.5%, 82.5%, corresponding to viscosities [1, 6.6, 14, 31, 85] mPa s, respectively. The different viscosities do not give any significant change in equilibrium contact angle ($\pm 2^{\circ}$), which were measured as $\theta_e = [20^{\circ}, 60^{\circ}, 109^{\circ}]$ for oxide, silane and teflon coatings.

The axi-symmetric Cahn-Hilliard Navier Stokes simulations mimic the experiments using the same material properties (density, viscosity, surface tension and equilibrium angle) as measured from experiments. To obtain the experimentally observed spreading behavior, an additional dissipation at the contact

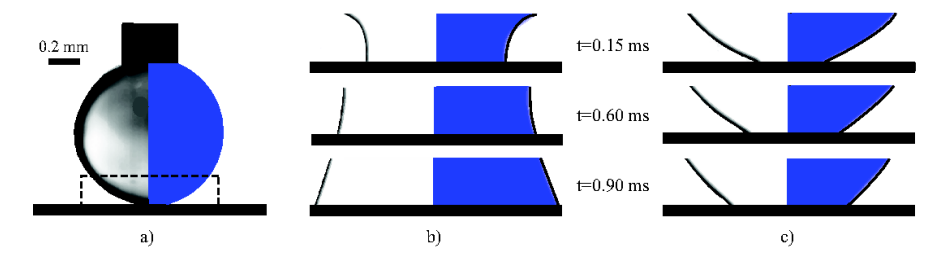


Figure 1: Panel a) Illustrates the initial condition for the experiments and the numerical simulations, where a drop held at the tip of a needle is brought into contact with a dry solid substrate. The dashed box in the figure shows the field-of-view in the experiments. In panels b) and c) are shown the drop shape near the substrate, at times t=0.15ms, t=0.60ms and t=0.90ms, after initial contact. Each panel shows a composite of experiment (left) and simulation (right). The black solid line in the right half that is plotted on top of the simulation result, illustrates experimental interface shape. b) A water drop spreading on an oxidized Si-wafer ($\theta_e=20^\circ$, viscosity $\mu_{H_2O}=1$ mPa s). c) Glycerin 82.5% drop spreading on an oxidized Si-wafer ($\theta_e\sim20^\circ$, viscosity $\mu_{glycerin_{82.5\%}}=85$ mPa s).

Mass fraction glycerin	0%	50%	65%	72.5%	82.5%
SiO_2 [Pa s]	0.15	0.33	0.51	0.66	1.02
Silane [Pa s]	0.17	0.26	0.33	0.41	0.80
Teflon [Pa s]	0.07	0.06	0.09	0.10	0.19

Table 1: Values for the contact line friction parameter μ_f [Pa s] for different viscosities and substrates (SiO_2 , Silane, Teflon) measured from the numerics.

line was necessary through a non-zero μ_f (Carlson et al. (2009)). μ_f was determined by obtaining a direct agreement between simulations and experiments, enabling a direct measurement of μ_f even in the presence of other contributions such as viscosity and inertia (Carlson et al. (2012)). The values for μ_f are reported in table I for all the surfaces and viscosities. A non-monotonicity in μ_f is observed for pure water for the SiO_2 and silane coating, the same dependency was reported by Carlson et al. (2009) when comparing with similar experiments by Bird et al. (2008). We can at the present time not explain this non-monotonicity for pure water. Fig. 1 shows the excellent agreement between simulations and experiments for a water-glycerin 82.5% drop with an initial radius $R \approx 0.5mm$. Fig. 1a shows the initial condition in the experiments and simulations, and the field of view in the experiments (dashed box). The same window was extracted from the numerics, however the whole drop was simulated.

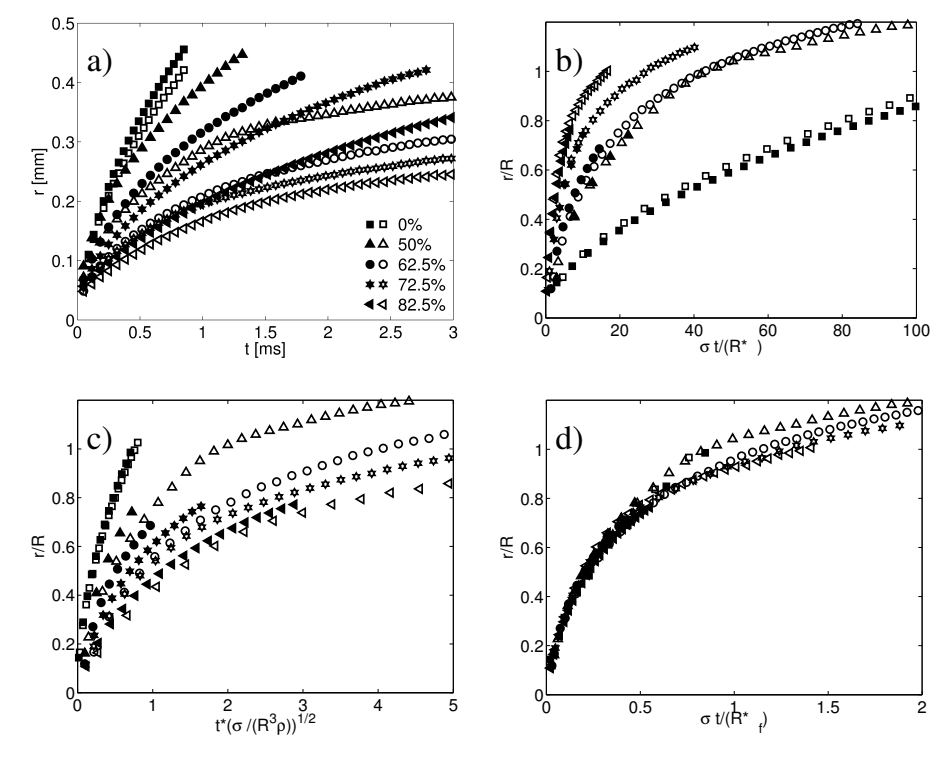


Figure 2: The spreading radius in time on an oxidized Si-wafer for two drop sizes $R \approx (0.3 \pm 0.02) \mathrm{mm}$ (hollow markers) and $R \approx (0.5 \pm 0.02) \mathrm{mm}$ (filled markers) for different mass fractions glycerin as indicated in the legend. (a) Dimensional units. (b) Viscous scaling. (c) Inertial scaling. (d) Contact line friction scaling.

Fig. 2a shows how the radial position of the contact line evolves in time for drops with different initial radii and for different viscosities on the oxidized Si-wafer. The markers represent the mean value after several realizations of the experiments (minimum of four) and the data set has been reduced for clarity. One observation to be made in fig. 2a is that the viscosity as well as the drop size influences the spreading.

Fig. 2b shows the same data, with the contact line radius scaled with initial drop radius R and the time scale with a viscous capillary speed σ/μ . The capillary speed σ/μ is 73m/s for water and 0.75 m/s for 85% glycerinwater. However, as is evident from fig 2b, this scaling fails to collapse the data, so the viscous contribution does not seem to be the limiting factor in this situation. An alternative would be an inertial scaling of time based on an inertial capillary velocity scale $\sqrt{\sigma/(\rho R)}$, as shown in fig 2c. As is evident here, this scaling does not capture the essential dynamics either, and we conclude

that neither inertia or bulk viscosity is the limiting factor for spreading in our experiments.

The remaining possibility is a capillary velocity based on the contact line friction discussed above and quantified in table 1. A representative velocity in this case can be found either from equation 2 or from dimensional analysis to be $u^* = \sigma/\mu_f$. Introducing the values for σ and μ_f from table 1 gives a speed of $u^*_{0\%} \sim 4.8 m/s$ for water and $u^*_{85\%} \sim 0.6 m/s$ for 85% glycerin. By scaling time with R/u^* , we do obtain a collapse of data, for the entire range of viscosities and drop sizes, see fig. 2d. The scattered dimensional plot represented in fig. 2a is reduced to a single spreading curve. Fig. 2 shows only results for the SiO_2 surface, but similar results are also obtained for the other solid surface coatings.

 μ_f is determined by adjusting it in simulations so that the mean spreading radius agrees with that of several experiments performed using the drop radius 0.5mm. It should be noted that the adjustment of this single parameter achieves excellent agreement for the entire drop shape, over the whole spreading event. We have also varied the drop size in additional experiments, which has a significant influence on the spreading radius (see fig. 2a). As shown in fig 2d, the data for both drop sizes collapse excellently when using a scaling of time according to $\sigma t/(R*\mu_f)$. The value of μ_f is thus independent of drop size, and this indicates that it is an intrinsic material property of the surface in combination with the wetting liquid.

Fig. 3a shows the non-dimensional collapse of data for the three surface coatings for different drop sizes and viscosities. By representing the dimensionless curves in fig. 3a in logarithmic axis, we observe that the radii follow the same slope independent of the solid surface at the early stage of the partial wetting, see fig. 3b. This is indicating that the governing physical mechanism is indeed the same for the different solid surfaces. From fig. 3b it is clear that the spreading radius evolves as $\frac{r}{R} \sim (\frac{\sigma t}{R\mu_f})^{\frac{1}{2}}$. A similar relationship is expected in a diffusion process, where in this context $\sigma R/\mu_f$ would represent a diffusion coefficient. This could indicate that a diffusive process is taking place at the contact line, which was suggested by Ren & E (2007) from rapid wetting simulations using molecular dynamics. However, a detailed study at the nanoscale would be needed to verify this. In the first stage of the spreading, for non-dimensional time < 1, the experiments cannot be fully captured by the hydrodynamic theory through Tanner's law $r = R(\frac{\sigma t}{\mu R})^{\frac{1}{10}}$ or by the molecular kinetic theory that predicts $r \sim t^{\frac{1}{7}}$ (de Ruijter et al. (1999), De Coninck et al. (2001)). We have for clarity inserted the slope predicted from Tanner's law in fig. 3b.

In fig. 3b a distinct transition between the 1/2 slope and a much more gradual slope ($\sim 1/10$) is observed around non-dimensional time 1. This might be an indication of the transition between contact line friction dominated spreading and another slower spreading regime. We assume here that the second regime is viscously dominated spreading given by Tanner's law and makes this

equal to the contact line friction dominated spreading $r = R\sqrt{\frac{\sigma t}{\mu_f R}}$ a distinct transition time (t_t) between the two regimes is obtained. In dimensional scales

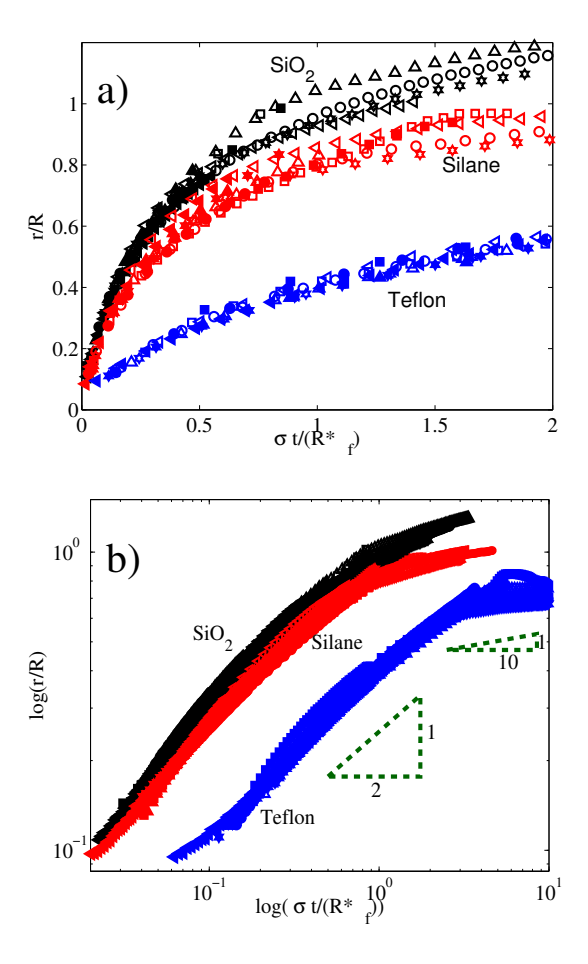


Figure 3: Non-dimensional spreading radius based on a contact line friction scaling on the different substrates (oxide (back), silane (red), teflon (blue)). Hollow markers denote (R=0.3mm) and filled markers (R=0.5mm). (a) Linear axis. (b) Logarithmic axis.

this becomes $t_t = \frac{R\mu_f}{\sigma} (\frac{\mu_f}{\mu})^{\frac{1}{4}}$ or in non-dimensional time (τ) , $\tau = \frac{t_t\sigma}{R\mu_f} = (\frac{\mu_f}{\mu})^{\frac{1}{4}}$. Introducing the material properties in the expression for τ we notice that a physically reasonable transition time is obtained and in very good agreement with the experimental results presented in fig. 3. For example, the dimensionless transition time for water and 85% glycerin is on the oxide surface found to be $\tau_{0\%} = 3.5$ and $\tau_{85\%} = 1.05$, respectively.

An analytical function can be derived for the contact line velocity (\hat{u}_{cl}) , based on the boundary condition given in eq. 1, if the equilibrium profile for the concentration across the interface is introduced and some algebra is performed (Yue & Feng (2011)),

$$\hat{u}_{cl} = \frac{\sigma}{\mu_f} \frac{\cos(\theta_e) - \cos(\theta)}{\sin(\theta)} \tag{2}$$

where θ is the dynamic or apparent contact angle. Eq. 2 is different from other expressions for the contact line velocity previously reported in the literature (de Gennes (1985)) by that it is divided by $\sin(\theta)$ which makes the expression diverge at angles 0° and 180°. This function is assumed to only be valid when the local dissipation at the contact line dominates. At these extrema, other mechanisms such as inertia or bulk viscous friction are expected to regularize the solution. $\sin(\theta)$ gives a non-negligible contribution to the function and introduces an additional non-linearity.

In fig. 3b it is clear that the spreading radius evolves as a function $r \sim R(\frac{\sigma t}{R\mu_f})^{\frac{1}{2}}$. By taking the time derivative of this expression we find that the contact line speed should be proportional to $\sim t^{-\frac{1}{2}}$. To evaluate the analytical expression for the contact line velocity given in eq. 2, we use the experimental data for the dynamic contact angle for the data presented in fig. 2a for the different viscosities and drop sizes, as they evolve on the oxidized wafer. We define the dynamic contact angle between the tangent along the contoured interface (interpolated at a fixed height of 7 pixels from the wall) and the solid substrate, on the liquid side. The dynamic contact angle measurements are found to be fairly insensitive to changes in interpolation height, as long as this height is chosen to be less than the local radius of curvature at the contact line.

Fig. 4 shows that the expression given in eq. 2 indeed gives a slope for the contact line speed as $\hat{u}_{cl} \sim R \sqrt{\frac{\sigma}{R\mu_f}} t^{-\frac{1}{2}}$. This indicates that $\frac{\cos(\theta_e)-\cos(\theta)}{\sin(\theta)} \sim R/r$, which from eq. 2 recovers the experimentally observed behavior presented in fig. 2d and fig. 3. The inset in fig. 4 shows the predicted contact line speed using the linearized function from molecular kinetic theory $\hat{u}_{MKT} = (\sigma/\mu_f) \cdot (\cos(\theta_e) - \cos(\theta))$ (de Ruijter et al. (1999)). Since we are interested in the slope for the contact line speed in time, we assume μ_f to be the same in \hat{u}_{MKT} as reported in table I. One clear observation to make from the inset in fig. 4 is that at non–dimensional time < 2.4 the slope for the contact line speed predicted from molecular kinetic theory $u_{MKT} = (\mu_f/\sigma)\hat{u}_{MKT}$ does not agree with the experimental observation in fig. 3.

In summary we have shown that spreading experiments and simulations for a wide range of viscosities, on substrates with very different wetting properties, all exhibit a universal spreading behavior if contact line friction dominates the spreading. An expression for the contact line radius is proposed for this spreading regime as $r \sim R(\frac{\sigma t}{\mu_f R})^{\frac{1}{2}}$. The analytical contact line velocity from phase field theory, where the dynamic contact angle is primary input, predicts

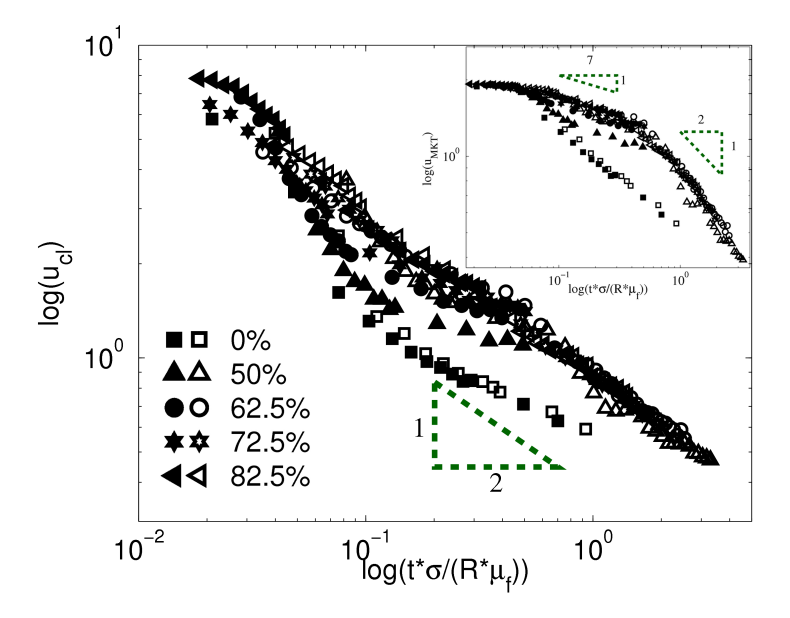


Figure 4: The main figure shows the dimensionless contact line velocity function from phase field theory $u_{cl} = \frac{\mu_f}{\sigma} \hat{u}_{cl} = (\cos(\theta_e) - \cos(\theta))/\sin(\theta)$. Inset shows the velocity predicted from the linearized molecular kinetic theory $u_{MKT} = \frac{\mu_f}{\sigma} \hat{u}_{MKT} = \cos(\theta_e) - \cos(\theta)$. The input in these two functions are the experimentally measured dynamic contact angle θ for two different drop sizes on the oxidized Si-wafer. The mass fraction glycerin is indicated in the legend. Hollow markers denote small (R=0.3mm) and filled markers large drops (R=0.5mm).

the same slope for the spreading as found directly in experiments. A criterion is proposed to determine the dominance of contact line friction or viscosity in spreading, which is found in good agreement with the experiments. We hope that these results can help rationalize spreading phenomena that falls beyond classical hydrodynamic theory, and gives a phenomenological explanation for such physics.

References

- BIANCE, A. L., CLANET, C. & Quéré, D. 2004 First steps in the spreading of a liquid droplet. *Physical Review E* **69** (1), 016301-1-4.
- BIRD, J. C., MANDRE, S. & STONE, H. A. 2008 Short-time dynamics of partial wetting. *Physical Review Letters* **100** (23), 234501.
- Blake, T. D. & Haynes. J. M. 1969. Kinetics of liquid/liquid displacement *Journal* of Colloid and Interface Science **30** (3), 421–423.
- BLIZNYUK, O., JANSEN, H. P., KOOIJ, E. S. & POELSEMA, B. 2010. Initial spreading kinetics of high-viscosity droplets on anisotropic surfaces. *Langmuir* **26** (9), 6328–6334.
- Carlson, A., Do-Quang, M. & Amberg, G. 2009 Modeling of dynamic wetting far from equilibrium. *Physics of Fluids* **21** (12), 121701–4.
- CARLSON, A., Do-QUANG, M. & AMBERG, G. 2011 Dissipation in rapid dynamic wetting. Journal of Fluid Mechanics 682, 213–240.
- Carlson, A., Bellani, G. & Amberg, G. 2012 Dissipation in short–time dynamic wetting. EPL 97, 44004-1–6.
- Chen, Q., Rame E. & Garoff, S. 1995 The breakdown of asymptotic hydrodynamic models of liquid spreading at increasing capillary number. *Physics of Fluids* 7 (11), 2631–2639.
- DE CONINCK, J., DE RUIJTER, M. J. & VOUE, M. 2001 Dynamics of wetting. Current opinion in Colloid and Interface Science 6 (1), 49–53.
- Duvivier, D., Seveno, D., Blake, T.D. Rioboo, R. & De Coninck, J. 2011 Experimental evidence of the role of viscosity in the molecular kinetic theory of dynamic wetting. *Langmuir*, 27, 13015–13021.
- DE GENNES, P. G. 1985 Wetting statics and dynamics. Review of Modern Physics 57 (3), 827–863.
- Huh, C. & Scriven, L. E. 1971 Hydrodynamic model of steady movement of a solid/liquid/fluid contact line. *Journal of Colloid and Interface Science* 35 (1), 85–101.
- JACQMIN, D. 2000 Contact-line dynamics of a diffuse fluid interface. Journal of Fluid Mechanics 402, 57–88.
- PREVOST, A., ROLLEY, E. & GUTHMANN, C. 1999 Thermally activated motion of the contact line of a liquid he-4 meniscus on a cesium substrate. *Physical Review Letters* 83 (2), 348–351.
- REN, W. & E, W. 2007 Boundary conditions for the moving contact line problem. *Physics of Fluids* **19** (2), 022101-1–15.
- REN, W. Hu, D. & E, W. 2010 Continuum models for the contact line problem . $Physics\ of\ Fluids,\ 22(10):102103-1-19.$
- DE RUIJTER, M. J., DE CONINCK, J. & OSHANIN, G. 1999 Droplet spreading: Partial wetting regime revisited. *Langmuir* **15** (6), 2209–2216.
- Voinov, O. V. 1976 Hydrodynamics of wetting. *Izvestiya Akademii Nauk SSSP*, *Makhanika Zhidkosti i Gaza* **5** (76–84).
- YUE, P. & FENG, J. J. 2011. Wall energy relaxation in the Cahn-Hilliard model for moving contact lines *Physics of Fluids* 23, 012106-1-8.